



Defense Threat Reduction Agency
8725 John J. Kingman Road, MS 6201
Fort Belvoir, VA 22060-6201



DTRA-TR-12-40

TECHNICAL REPORT

High Intensity Superconducting Cyclotron

Approved for public release; distribution is unlimited.

December 2012

DTRA 10-274M, 11-2492M

Authored by:

Joseph V. Minervini

Prepared by:

Massachusetts Institute of Technology
Plasma Science and Fusion Enter
Fusion Technology and Engineering Division
185 Albany Street
Cambridge, MA 02139

DESTRUCTION NOTICE:

Destroy this report when it is no longer needed.
Do not return to sender.

PLEASE NOTIFY THE DEFENSE THREAT REDUCTION
AGENCY, ATTN: DTRIAC/J-3 ONIU, 8725 JOHN J. KINGMAN ROAD,
MS-6201, FORT BELVOIR, VA 22060-6201, IF YOUR ADDRESS
IS INCORRECT, IF YOU WISH THAT IT BE DELETED FROM THE
DISTRIBUTION LIST, OR IF THE ADDRESSEE IS NO
LONGER EMPLOYED BY YOUR ORGANIZATION.

REPORT DOCUMENTATION PAGE					Form Approved OMB No. 0704-0188	
<p>The public reporting burden for this collection of information is estimated to average 1 hour per response, including the time for reviewing instructions, searching existing data sources, gathering and maintaining the data needed, and completing and reviewing the collection of information. Send comments regarding this burden estimate or any other aspect of this collection of information, including suggestions for reducing the burden, to Department of Defense, Washington Headquarters Services, Directorate for Information Operations and Reports (0704-0188), 1215 Jefferson Davis Highway, Suite 1204, Arlington, VA 22202-4302. Respondents should be aware that notwithstanding any other provision of law, no person shall be subject to any penalty for failing to comply with a collection of information if it does not display a currently valid OMB control number.</p> <p>PLEASE DO NOT RETURN YOUR FORM TO THE ABOVE ADDRESS.</p>						
1. REPORT DATE (DD-MM-YYYY) 00-12-2012		2. REPORT TYPE Technical		3. DATES COVERED (From - To) Aug. 2010 - Aug. 2012		
4. TITLE AND SUBTITLE High Intensity Superconducting Cyclotron				5a. CONTRACT NUMBER DTRA 10-2747M, 11-2492M PSU ARL S11-07		
				5b. GRANT NUMBER		
				5c. PROGRAM ELEMENT NUMBER		
6. AUTHOR(S) Joseph V. Minervini				5d. PROJECT NUMBER		
				5e. TASK NUMBER		
				5f. WORK UNIT NUMBER		
7. PERFORMING ORGANIZATION NAME(S) AND ADDRESS(ES) Massachusetts Institute of Technology Plasma Science and Fusion Center Fusion Technology and Engineering Division 185 Albany Street				8. PERFORMING ORGANIZATION REPORT NUMBER HISCC (Megatron) Final Report		
9. SPONSORING/MONITORING AGENCY NAME(S) AND ADDRESS(ES) Defense Threat Reduction Agency John J. Kingman Road, STOP 6201, Fort Belvoir, VA 22060 Pennsylvania State University/ Applied Research Laboratory, P.O. Box 30, State College, PA 16804-0030				10. SPONSOR/MONITOR'S ACRONYM(S) DTRA/J9NTD; PSU/ARL		
				11. SPONSOR/MONITOR'S REPORT NUMBER(S) DTRA-TR-12-40		
12. DISTRIBUTION/AVAILABILITY STATEMENT Approved for public release; distribution is unlimited.						
13. SUPPLEMENTARY NOTES Prepared by MIT under contract with Pennsylvania State University/ Applied Research Laboratory with funding from the Defense Threat Reduction Agency						
14. ABSTRACT The Massachusetts Institute of Technology undertook to design, fabricate and test a prototype compact superconducting proton cyclotron which addressed all fundamental design and performance issues for a cyclotron at a final energy of 250 MeV and final beam intensity of 1 mA with less than 0.1% extraction loss. In March 2012, DTRA suspended work on the project indefinitely. This report documents the accomplishments and status of work on the five major subsystems of the project: 1) proton injection using external electron cyclotron resonance source with axial injection using spiral inflector; 2) magnetic field design; 3) radio frequency accelerating cavities; 4) cryogenic system; 5) beam extraction.						
15. SUBJECT TERMS compact surperconducting cyclotron; superconducting magnet; cryogenic system; electron cyclotron resonance ion source; spiral inflector; radio frequency acceleration, thermal management; quench analysis; beam extraction; high power beam dump						
16. SECURITY CLASSIFICATION OF:			17. LIMITATION OF ABSTRACT	18. NUMBER OF PAGES	19a. NAME OF RESPONSIBLE PERSON	
a. REPORT	b. ABSTRACT	c. THIS PAGE			James Lemley	
U	U	U	UU	154	19b. TELEPHONE NUMBER (Include area code) 703-767-4208	

Reset

Table of Contents

Table of Contents	2
List of Figures.....	5
List of Tables	9
Executive Summary	10
1.0 Tasks and Work Breakdown Structure	11
1.1 Project Work Breakdown Structure (WBS).....	11
1.2 Phase 2a Detailed Tasks.....	12
2.0 General System Requirements	13
2.1 Reference Configuration	13
2.2 Magnet.....	14
2.3 Ion Source	14
2.4 Acceleration	14
2.5 Beam Structure	15
2.6 Vacuum System	15
2.7 Cryogenics.....	15
2.8 Mechanical Support.....	15
2.9 Dose and Field	16
2.10 Beam Dump.....	16
3.0 System Design Description	16
3.1 Reference Configuration	16
3.2 Reference Magnetic Geometry	16
3.3 Isochronous Cyclotron Requirements.....	19
3.3.1 Isochronous Condition.....	19
3.3.2 Flutter.....	22
3.4 Magnet.....	24
3.5 Electron Cyclotron Resonance Ion Source	25
3.5.1 Source Design and Assembly	25
3.5.2 Power Supplies	28
3.5.3 Characterization of the Ion Beam	29
3.6 Axial Injection.....	31
3.7 Acceleration	31
3.8 Beam Structure	32
3.9 External Beam Matching.....	32
3.10 Vacuum System.....	32
3.11 Cryogenics System Design.....	32
4.0 Magnetic Field Design.....	37
4.1 Magnetic Design with Rare Earth Pole Tips	37
5.0 Cyclotron Layout	41
6.0 Magnet Design	43
7.0 Quench Analysis	46
7.1 Summary	46

7.2	Details.....	47
8.0	Magnet Nuclear Heating.....	52
8.1	The radiation challenges of Megatron.....	52
8.2	The MegatronG4 Simulation.....	54
8.3	Verification and validation of MegatronG4	56
8.4	Results from the MegatronG4 Simulation	61
8.5	Feasibility assessment of an ex-situ beam diagnostic	66
9.0	Temperature Distribution in Winding Pack Due to Radiation Heating ..	67
9.1	Thermal model.....	67
9.2	Heating source.....	70
9.3	Results without steel yoke	73
9.4	Results with steel yoke	74
9.5	Analytical model	75
10.0	Central Region Design.....	75
10.1	Introduction.....	75
10.2	Magnetic field design.....	76
10.3	Material: Holmium	77
10.4	Magnet design	78
10.4.1	Model 406.....	78
10.4.2	Model 018H.....	81
10.4.3	Idealized Magnetic Field.....	86
10.4.4	Summary.....	91
10.5	Central Region.....	91
10.5.1	Part I: Source to Puller Gap	91
10.5.2	Part II: Inner Large E-Map	92
10.6	Future Work	95
10.7	References.....	96
11.0	RF System Design.....	96
11.1	System Introduction	96
11.2	System Outline and Parameters	97
11.3	RF Resonator Electromagnetic Design	97
11.3.1	HFSS Single Stem Case.....	98
11.3.2	HFSS "Flat-Top" Case.....	98
11.3.3	Resonator Voltage Distribution	99
11.3.4	Resonator Voltage Distribution	100
11.3.5	Resonator Plans.....	100
11.4	RF System Stability Modeling and Analysis.....	101
11.4.1	System Modeling Introduction	101
11.4.2	System Modeling – Dee Cavity 1	101
11.4.3	System Modeling – Dee Cavity 2	101
11.4.4	System Modeling – Dee Cavity 3	102
11.4.5	System Modeling – Dee Cavity 4	103
11.4.6	System Modeling – Dee Cavity 5	104
11.4.7	System Modeling – Dee Cavity 6	104
11.4.8	System Modeling – Transfer Function 1	105
11.4.9	System Modeling – Transfer Function 2	106
11.4.10	System Modeling – PID.....	106
11.4.11	System Modeling – Simulink PID	107

11.4.12	System Modeling – PID Response	107
11.4.13	ADRC – Active Disturbance Rejection Control	108
11.4.14	ADRC Block Diagram.....	108
11.4.15	ARDC 3 rd Order ESO	109
11.4.16	ADRC Mechanics - 2	109
11.4.17	ADRC Mechanics - 3	110
11.4.18	System Modeling – Simulink ADRC.....	111
11.4.19	Third Order ADRC Simulation	111
11.4.20	System Modeling & Control Summary	112
11.5	Necessary Technology.....	112
11.6	Estimated Cost	113
11.7	RF Summary Summary.....	113
12.0	Evolution of Proton Bunches in HI Cyclotrons: a Preliminary Study...	114
12.1	Introduction.....	114
12.2	Geometrical effects.....	114
12.3	Physical models for the evolution of the proton bunch.....	114
12.3.1	A. Kinetic description	114
12.3.2	Fluid description.....	116
12.3.3	Electromagnetic fields	117
12.4	Summary	118
12.5	Starting fluid equations: Non-dimensional equations in moving frame.....	118
12.6	Ideal focusing model.....	119
12.7	Asymptotic analysis: Asymptotic expansion	120
12.8	Asymptotic analysis	120
12.9	Solving the equations	122
12.9.1	The betatron oscillations	122
12.9.2	The slow time scale evolution	124
12.10	Numerical results	125
12.10.1	Numerical method.....	126
12.10.2	Numerical results: Cylindrical bunch	126
12.10.3	Numerical results: Elliptic bunch	127
12.11	Future plans	133
13.0	High Power Beam Dump System Final Design.....	133
13.1	Overview.....	133
13.2	Beam dump design	133
13.3	Radiation Transport Modeling.....	135
13.3.1	Energy deposition and heating.....	135
13.4	Activation.....	138
13.5	Mechanical Design and Analysis.....	139
13.5.1	Thermal Analysis	139
13.5.2	Cooling System and Analysis.....	140
13.5.3	Vacuum system	143
13.6	Manufacturing plan	146
13.7	Long-lead items	150
13.8	Beam Monitoring and Diagnostics	150
14.0	Acknowledgements.....	151

List of Figures

Fig. 3.1	A median plane cross-sectional view showing the pole profile of the compact, high field, $K_{\text{bending}}=250$, isochronous cyclotron is shown. [Reference Opera 3D Model is 3D31f]. Iron of model 3D31f has a circumferentially continuous cylindrical skirt within $0.419 \text{ m} < r < 0.500 \text{ m}$. The pole spiral limited by the skirt at $r=0.419 \text{ m}$ is $\theta=r/(1.01*0.419/2)$.	17
Fig. 3.2	Iron Point Definitions	17
Fig. 3.3	Pole spiral shape (Model 3D31F coordinate system.)	18
Fig. 3.4	The scheme of the magnetic field B vs. radius r of an isochronous cyclotron.	19
Fig. 3.5	The kinetic energy and the total energy variation with radius in an isochronous cyclotron	20
Fig. 3.6	The azimuthal average of the Reference Model 3D31f axial field along a 45° width hill of the K250-42 isochronous cyclotron (B_{av3D}) is compared with the ideal average field (B_z_{goal}).	21
Fig. 3.7	The azimuthal average of the Reference Model 3D31f axial field along a 45° width valley of the K250-42 isochronous cyclotron (B_{av3D}) is compared with the ideal average field (B_z_{goal}).	22
Fig. 3.8	Spiral geometry of the K250 isochronous cyclotron.	22
Fig. 3.9	Isometric CAD model view of the ion source.	26
Fig. 3.10	Cross-sectional view of CAD model of the ion source.	26
Fig. 3.11	Axial component of B along axis ($r = 0$). Exit of ionizer is at 100 mm.	27
Fig. 3.12	Main components of the ECRS ion source. At top left, the sapphire window in the microwave waveguide. At the top right the magnetic shield with the small coils. Bottom left shows the extractor. Bottom right shows the apparatus for testing the HV microwave source and the dummy load.	28
Fig. 3.13	Two versions of magnetically permeable “plasma” exit grids.	28
Fig. 3.14	Equipment assemblies. At left, ion source with RF assembly mounted on diagnostics flange atop the superconducting test magnet. At right, the rack-mounted ion source power supplies.	29
Fig. 3.15	Magnetic field surrounding the ion source, with magnetic shielding.	30
Fig. 3.16	Magnetic field contours of the superconducting magnet in the region below the ion source. The magnetic shield of the ion source can be seen in the top left of the figure.	30
Fig. 3.17	Schematic of the three liquid helium cryostats used to cool the Megatron cryogenics systems.	34
Fig. 3.18	Semi-transparent solid model for the current lead cryostat.	34
Fig. 3.19	a) Semi-transparent solid model for the helium recondensing cryostat, and b) digital image for one of the Daikin three-stage cryocoolers.	36
Fig. 3.20	Acceptance test performance data for one of the Megatron’s Daikin CG310SC cryocoolers. Both cryocoolers gave similar performance meeting the specification.	37
Fig. 5.1	Cross-sectional view of the Megatron cyclotron.	41
Fig. 5.2	Top view of the Megatron showing the spiral pole tips and the cold-to-warm supports of the cold mass in the cryostat.	42

Fig. 5.3 Cross-sectional view of the Megatron cyclotron showing the nominal dimensions of the iron yoke, the superconducting coil, and steel structural support yoke for the coil.	42
Fig. 6.1 Photograph of the NbTi Cable-in-Channel for the Megatron coils.	45
Fig. 6.2 Drawing of 2000 A CryoSaver current leads made by HTS-110 showing the dimensions.	46
Fig. 7.1 Coil current.....	48
Fig. 7.2 Fraction of winding normal.....	48
Fig. 7.3 Coil hot spot temperature.....	49
Fig. 7.4 Voltage along the windings.....	49
Fig. 7.5 Coil normal resistance.....	49
Fig. 7.6 Fig. 7.6 Quench from Bmax, Rd=0.04 Ω , 1 s. Three dimensional temperature distribution at 1 s. Each small window represents a view of the r (vertical) – z (horizontal) plane at one of 16 evenly distributed azimuthal (θ direction) slices around the coil.....	50
Fig. 7.7 Quench from Bmax, Rd=0.04 Ω , 3 s. Three dimensional temperature distribution. Each small window represents a view of the r (vertical) – z (horizontal) plane at one of 16 evenly distributed azimuthal (θ direction) slices around the coil.	50
Fig. 7.8 Quench from Bmax, Rd=0.04 Ω , 25 s. Three dimensional temperature distribution. Each small window represents a view of the r (vertical) – z (horizontal) plane at one of 16 evenly distributed azimuthal (θ direction) slices around the coil.	51
Fig. 7.9 Quench from Bmin, Rd=0.04 Ω , 2.5 s. Three dimensional temperature distribution. Each small window represents a view of the r (vertical) – z (horizontal) plane at one of 16 evenly distributed azimuthal (θ direction) slices around the coil.	51
Fig. 7.10 Quench from Bmin, Rd=0.04 Ω , 28 s. Three dimensional temperature distribution. Each small window represents a view of the r (vertical) – z (horizontal) plane at one of 16 evenly distributed azimuthal (θ direction) slices around the coil.	52
Fig. 8.1 Main processes in the production of neutrons in the Megatron.	53
Fig. 8.2 Schematic of the nuclear radiation process that results in heating of the structures.	53
Fig. 8.3 Drawing of the Geant4 model of the Megatron.....	55
Fig. 8.4 3D voxelization of the MegatronG4 geometry. A low-resolution 3D voxelization of the SC coils (magenta) is imaged over the geometry. High resolution 3D voxelization are used for simulation with r=40, phi=180, z=5 divisions for a total of 36000 voxels.	55
Fig. 8.5 Top down view of 250 MeV proton beam (yellow) incident into upon a copper target (obscured). Spallation neutrons (cyan) and induced gammas (magenta) scatter through the geometry and deposited energy into the SC coils (red) and SC coil bobbin (green).	56
Fig. 8.6 Peak heating of a single superconducting coil from a $0.25 \times 10^{-6} \text{ W/cm}^3/\text{nA}$ beam. Top-down view of heating tally mesh in a C400 PHITS simulation.	57

HISCC (Megatron) Final Report

Fig. 8.7 MCNPX simulation of heating in the cold mass of the S2C2. Heating of single SC coil: 1.5 W/ μ A beam, peak heating of SC coil: 0.35×10^{-3} W/cm ³ / μ A, total heating of cold masses: 3.86 W/ μ A.	58
Fig. 8.8 A cross-section of the benchmarking geometry and two simulation setups in MCNPX.	59
Fig. 8.9 Spallation benchmarking for 250 MeV protons on a nickel target.....	59
Fig. 8.10 a) (Top) shows heating in the coil copper in watts as a function of neutron energy in the range 0 to 150 MeV, b) (Bottom), expanded scale heating in the coil versus neutron energy in the range 0 to 20 MeV.	60
Fig. 8.11 Nuclear heating for full stopping of a 1 μ A proton beam in the beam target for 7 different target materials.	63
Fig. 8.12 Activated beam dump cooling times for 1.6 mA, 150 MeV proton beam.	64
Fig. 8.13 a) Peak heating in the azimuthal direction from protons deposited in the superconducting magnet, b) peak heating in the radial direction, at different axial heights, from protons deposited in the superconducting magnet. Results are based on using a 5x5x70 mm nickel beam target.	65
Fig. 8.14 Top-down view of Megatron with an external Helium-3 detector.....	66
Fig. 8.15 ³ He count rates as a function of Megatron beam currents at different energies.....	67
Fig. 9.1 Cyclotron geometry used for analysis.	68
Fig. 9.2 Cable configuration used in the analysis.....	68
Fig. 9.3 Thermal properties of Cu at low temperatures.	69
Fig. 9.4 Thermal properties of SS used in this analysis.....	69
Fig. 9.5 Thermal properties of G10 at low temperatures.....	70
Fig. 9.6 Heating source determined by Hartwig using MCNP.....	71
Fig. 9.7 Radial fit to the heating profile, for the cells at the bottom of the winding pack at the poloidal location near the peak of the heating.	72
Fig. 9.8 Axial fit to the heating profile, for the cells at the innermost set of cells at the poloidal location near the peak of the heating.	72
Fig. 9.9 Poloidal fit to the heating profile, for the cells at the innermost set of cells at the bottom of the winding pack.	72
Fig. 9.10 Analytic heating source in the model.	73
Fig. 9.11 Temperature along horizontal planes and along vertical planes on winding pack.	73
Fig. 9.12 Model with steel.	74
Fig. 9.13 Temperature profiles in the case with the steel.	74
Fig. 10.1 Comparison of the magnetism of Holmium and Steel.....	77
Fig. 10.2 OPERA design of the Model 406.....	78
Fig. 10.3 The magnetic field and the proton energy of Model 406.....	79
Fig. 10.4 Phase properties of Model 406.....	80
Fig. 10.5 Betatron tunes of Model 406.....	81
Fig. 10.6 OPERA design of Model 018H.....	82
Fig. 10.7 The magnetic field and the proton energy of Model 018H.....	83
Fig. 10.8 Phase properties of Model 018H.....	84
Fig. 10.9 Betatron tunes of Model 018H.....	85
Fig. 10.10 Flutter comparison of the two models.....	86
Fig. 10.11 Ideal Isochronous Magnetic Field contours for Model 018H.....	88

HISCC (Megatron) Final Report

Fig. 10.12 Ideal Isochronous Magnetic Field B vs R	89
Fig. 10.13 The general beam dynamics of the ideal magnetic field	90
Fig. 10.14 The source-to-puller electric field map	91
Fig. 10.15 Ion trajectories with different injecting situations of a) starting time, b) injecting angle, c) injecting position ξ_0 , d) injecting position η_0	92
Fig. 10.16 Design of the cyclotron central region part II.....	93
Fig. 10.17 The electric field of part II.....	94
Fig. 10.18 The ion trajectory from Z3CYCLONE part I.....	95
Fig. 11.1 Schematic of Megatron RF system components.	96
Fig. 12.1 Initial bunch density profile - cylindrically symmetric case	127
Fig. 12.2 Bunch density profile after 100 revolutions - cylindrically symmetric case...	128
Fig. 12.3 Bunch density profile after 500 revolutions - cylindrically symmetric case...	128
Fig. 12.4 Bunch density profile after 1000 revolutions - cylindrically symmetric case.	129
Fig. 12.5 Initial bunch density profile - Elliptic initial density profile	130
Fig. 12.6 Bunch density profile after 100 revolutions - Elliptic initial density profile...	130
Fig. 12.7 Bunch density profile after 500 revolutions - Elliptic initial density profile...	131
Fig. 12.8 Bunch density profile after 1000 revolutions - Elliptic initial density profile.	131
Fig. 12.9 Bunch density profile after 1500 revolutions - Elliptic initial density profile.	132
Fig. 12.10 Bunch density profile after 2000 revolutions - Elliptic initial density profile	132
Fig. 13.1 Beam Dump Target Design Schematic	134
Fig. 13.2 Beam dump target sizing	134
Fig. 13.3 MCNPX Geometry Implementation.....	136
Fig. 13.4 Energy deposition values in $\text{W}/\text{cm}^3/\text{mA}$ and throughout the original beam dump	137
Fig. 13.5 Volumetric heating rates as a function of distance along the beam dump for several layers. The boundaries for each layer are given at the bottom of the figure.	137
Fig. 13.6 Effects of shielding on dose fields surrounding beam dump with cyclotron at full power (1 mA of 250 MeV protons).....	139
Fig. 13.7 Temperature profiles in beam dump for varying water coolant flow rates.	140
Fig. 13.8 Cooling schematic layout	141
Fig. 13.9 Channel measurements	142
Fig. 13.10 Collection manifold	143
Fig. 13.11 Vacuum schematic layout.....	144
Fig. 13.12 VacIon pump	145
Fig. 13.13 Pressure gauge	145
Fig. 13.14 Brazed assembly of cooling chamber.....	146
Fig. 13.15 Inlet flare.....	147
Fig. 13.16 Lanced and offset fins.....	147

List of Tables

Table 3.1 Iron Point Coordinates, Model 3D31f	17
Table 3.2 Spiral hill edge coordinates, Model 3D31f	18
Table 3.3 Parameters of the azimuthal degree vs r of gap 1	23
Table 3.4 Parameters of the final revolution $r = 40$ cm	24
Table 3.5 Parameters of the K250-42 Superconducting Magnet (Reference Model 3D31f)	25
Table 3.6 Anticipated heat load at 65 K on the Cryomech cryocooler in the current lead cryostat	35
Table 3.7 Anticipated heat load at 4.3 K on helium circuit due to the current lead and magnet cryostats	36
Table 3.8 Heat load at 4.3 K on helium circuit due to helium recondensing cryostat	36
Table 4.1 Megatron Model Ho-406	38
Table 4.2 Megatron Model FePM-506	39
Table 6.1 Winding pack parameters for the Megatron magnet	43
Table 6.2 Strand and Cable-in-Channel conductor design parameters	44
Table 6.3 Conductor piece lengths as delivered	45
Table 6.4 Measured conductor performance parameters	45
Table 7.1 Winding Parameters	47
Table 8.1 Target materials considered for an intermediate proton beam dump	63
Table 8.2 Comparison of beam loss in the cold mass for three different cyclotrons	65
Table 9.1 Winding pack parameters used in the thermal calculations	67
Table 9.2 Effective thermal conductivities in the smeared model	70
Table 10.1 Principal parameters of the cyclotron	75
Table 11.1 System geometry and operating parameters	97
Table 11.2 Resulting Resonator Parameters	99
Table 11.3 Estimated costs of RF system components	113
Table 13.1 Steady-state activity for the full power 250 MeV 1 mA proton beam	138
Table 13.2 Coolant flow rates throughout system	140
Table 13.3 Pumping rates	144
Table 13.4 Vacuum system bill of materials	148
Table 13.5 Cooling system bill of materials	149
Table 13.6 Beam diagnostic measurement concepts	150

Executive Summary

Under this program the Massachusetts Institute of Technology proposed to design, fabricate, and test a prototype Compact Superconducting Proton Cyclotron, which addresses all of the fundamental design and performance issues for a cyclotron at a final energy of 250 MeV. The immediate objective was to design, build and demonstrate a compact transportable 250 MeV High Intensity Superconducting Cyclotron (HISCC) with a final beam intensity of 1 mA and an extraction loss rate of less than 0.1%. In doing so, the fundamental feasibility and engineering issues of the GeV class machines would be addressed, but at this lower power level, the technology can be adequately demonstrated and be accomplished more rapidly and at significantly lower overall cost

An initial first phase 1, 6 month feasibility design study was completed in 2010 under DTRA funding through the Los Alamos National Laboratory (LANL). That conceptual design was completed in November 2010. In December, 2010 the second phase to perform the final design, fabrication, assembly, and low level power commissioning began under DTRA source funding through the Pennsylvania State University, Applied Research Laboratory (PSU-ARL) as the prime contractor, with MIT research performed under sub-contract from them.

In March 2012, DTRA took a decision to stop all work on this research subject and the program was halted before the Megatron project could be completed. This report provides a summary of the overall system requirements, a summary of the status of the component design and analysis, early equipment and materials procurements, and a summary of the remaining work required to complete the project. This report reflects the technical status as of February 29, 2012. Many tasks were incomplete at that time, so the details given here report the work-in-progress, and do not constitute a final design ready for fabrication.

1.0 Tasks and Work Breakdown Structure

The Phase 2 effort was initially funded to begin with a 6-month, Phase 2a effort to address engineering design and planning for the complete design/fabricate/test effort, and to result in a project baseline for cost and schedule. This was to be followed by a separate 2-year effort to finish the detailed design, fabrication, assembly, and low power commissioning test of the 250 MeV prototype system. This project progressed only through the Phase 2a effort and all Phase 2b and 2c (second and third year) tasks remain incomplete.

Phase 2a- Detailed Design and Long-Lead Items Procurement.

Work Breakdown Structure: A Project Work Breakdown Structure (WBS) for the entire Phase 2-Manufacturing Design, Fabrication, Assembly, and Testing is given below. All work scope follows from the phased program structure and work progress, scheduled tasks, and costs were monitored according to the WBS. Each major element had a senior person responsible for its execution.

1.1 Project Work Breakdown Structure (WBS)

- 2.0 Project Office
 - 2.1 Final Cyclotron Design and Analysis
 - 2.1.1 Field Design
 - 2.1.2 Beam Dynamics
 - 2.1.3 Cyclotron Fast Energy and Intensity Control
 - 2.2 Final Magnet and Charging Circuit
 - 2.2.1 Magnet Design and Analysis
 - 2.2.2 Magnet Fabrication, Assembly, and Test
 - 2.2.2.1 Tooling, Coil, Cryostat, Leads, Supports
 - 2.2.2.2 Charging Circuit Fabrication, Assembly, and Test
 - 2.2.2.3 Support Cyclotron Integrated Systems Test
 - 2.3 Final RF System
 - 2.3.1 Cyclotron RF Resonator
 - 2.3.1.1 Final Design and Analysis
 - 2.3.1.2 Baseline Cyclotron RF Design Report
 - 2.3.1.3 RF Amplifiers
 - 2.3.2 RF Controls and Instrumentation
 - 2.3.2.1 Systems Models and Analysis
 - 2.3.2.2 Electronics System Design
 - 2.3.2.3 Proposed Modules
 - 2.3.3 Support Cyclotron Integrated Systems Test
 - 2.4 Final Cyclotron Systems
 - 2.4.1 Ion Source and Axial Injection
 - 2.4.2 Central Region Design
 - 2.4.3 Beam Chamber Resonators and Dees
 - 2.4.4 Vacuum System
 - 2.4.5 Probes and Diagnostics
 - 2.4.6 Beam Extraction System

HISCC (Megatron) Final Report

- 2.4.7 Cyclotron Assembly and Testing
 - 2.4.7.1 Cyclotron Test facility Preparation
 - 2.4.7.2 System Integration
 - 2.4.7.2.1 Verify Magnet
 - 2.4.7.2.2 Assemble Beam Chamber
 - 2.4.7.2.3 RF Testing
 - 2.4.7.2.4 Internal Beam Tests
 - 2.4.7.2.5 External Beam Tests
 - 2.4.7.3 Test Plan
 - 2.4.7.4 Cyclotron Integrated System test
- 2.5 Final Instrumentation and Controls
 - 2.5.1 Control System Software and Programming
 - 2.5.2 Controls Fabrication and Procurement
 - 2.5.3 Controls Assembly and Test Plan
 - 2.5.4 Support Cyclotron Integrated Systems Test
- 2.6 Final Neutronics Simulation and Beam Dump
 - 2.6.1 Neutronics Simulation for Beam Losses in the Cyclotron
 - 2.6.2 High Power Beam Dump Fabrication and Test
 - 2.6.3 Support Cyclotron Integrated Systems Test
- 2.7 Final Radiation Effects and Safety
 - 2.7.1 Radiation Effects Assessment
 - 2.7.2 Assembly and Testing Safety Requirements
 - 2.7.3 Support Cyclotron Integrated Systems Test
- 2.8 Reviews and Reporting
 - 2.8.1 Reports
 - 2.8.2 Project Reviews

1.2 Phase 2a Detailed Tasks

Task 1: Detailed design field, beam dynamics, and cyclotron control

Perform detailed field design to final specification and further beam dynamics simulations in support of sub-systems design and high current operation of the cyclotron.

Task Responsibility: MIT - T. Antaya

Task 2: Detailed design of superconducting magnet system and tooling

Magnet tooling final design and procurement and fabrication, set-up conductor soldering line, procure dummy conductor for reaction, winding, and soldering trials. Start detailed design of winding bobbin cryostat, and quench detection and protection circuit. Finalize specification for magnet iron.

Task Responsibility: MIT – J. Minervini

Task 3: Detailed design of RF system

Begin detailed design and development of the cyclotron RF resonators, input couplers, tuners, sensors, transmission lines, amplifiers, and control electronics. Begin design of 2 RF amplifiers, 84 MHz, 200kW each.

Task Responsibility: MSU – J. Vincent

Task 4: Detailed design of cyclotrons systems

Detailed design of ion source and axial injection, central region design, beam chamber resonators and dees, beam extraction system, and beam chamber vacuum system.

Task Responsibility: MIT - T. Antaya

Task 5: Detailed design of system instrumentation and controls

Design and specify detailed system instrumentation, control hardware and software.

Task Responsibility: MIT – P. Michael

Task 6: Detailed neutronics simulation and beam dump design

Perform neutronics simulation of cyclotron structure as design evolves. Determine internal beam loss effects at full energy and calculate heat load and radiation fluences to cryostat and superconducting coils, peak heat loads to conductors and radiation fluences and radiation effects in the extraction channel.

Begin detailed design of external beam dump.

Task Responsibility: MIT R. Lanza

Task 7: Radiation effects and safety

Radiation effects and safety feasibility analysis coupled to the neutronics analysis. Select materials to mitigate radiation. Assist in definition of high power diagnostics.

Task Responsibility: MIT: R. Lanza

2.0 General System Requirements

This section summarizes the general system requirements.

2.1 Reference Configuration

Machine Type: Single stage compact superconducting isochronous cyclotron

Final Energy: 250 MeV \pm .25 MeV

Energy Spread: $\Delta E/E \leq 0.5\%$ FWHM

Ion Species: proton

External Beam Intensity:

Minimum: 0.9 emA

Maximum: 1 emA

Extraction Efficiency: = 99.9 %

4 spiral poles, 2 RF cavities,

Large Acceptance Extraction:

electrostatic deflector in a valley (2 dees)

Single turn extraction not a goal

RF/acceleration parameters:

Acceleration on 1st harmonic

look at 2nd harm.

Fundamental RF freq: ~84 MHz

Cavities peak field: aiming for 800-1000 turns

Spiralled cavities

Cyclotron is transportable

4K cooling via cryocoolers: Liquid helium cooled via thermosiphon loop

2.2 Magnet

Magnet type: cryostable, superconducting split coil, warm iron ferromagnet
Peak Field at Full Energy: $B(r=0) \equiv B_0 \leq 9.50$ T
Peak Field at Second Energy: $B(r=0) \equiv B_2 \leq 7.95$ T
Orientation: symmetry axis horizontal
Rotation: None
Total Ampere Turns: TBD
Engineering Current Density: ≤ 15000 A/cm²
Peak Field at Conductor: TBD
Maximum Operating Temperature at the conductor: TBD
Fringe Field: $B(r=3\text{m}, z=0) \leq 0.5$ mT
Magnet Mass: \leq TBD tons
Iron Return Yoke Ring Material: \leq 1028 Steel
Iron Pole Material: \leq 1008 Steel
Pole Radius: 0.40 m
Pole Gap: TBD
Conductor: Nb₃Sn or NbTi Cable-in-Channel
Winding Pack: epoxy impregnated S2 glass composite
Winding Pack Cooling: Liquid helium at coil surfaces, thermosiphon vapor to recondensing cryocooler
Current Leads: Low loss, burnout proof, high temperature superconductor (HTS)
Helium Vessel Maximum Design Pressure: TBD
Cryostat Maximum Design Pressure: TBD

2.3 Ion Source

Ion species: protons
ECR source + axial injection
10 mA DC current
Injection emittance 0.01 mm-mr
Initial phase width $< 5^\circ$

2.4 Acceleration

Proton Gamma at 250 MeV: $\gamma=1.267$
Acceleration: 180° dee and 180° dummy dee
Starting Frequency (f_0): TBD MHz
Starting Radius (r_0): 2.81 cm
Final Frequency (f_{ext}): TBD MHz
Extraction Radius (r_{ext}): 25 cm
Dee Voltage (V_0): 50 kV
Resonator Type: $\frac{3}{4}$ wavelength dee and structure at 145 MHz with rotary condenser
Oscillator Type: Self-excited grounded grid power tube with filament (dee) and collector (stub) feedback
Acceleration Gaps per Revolution: 2
Bunch Phase Error: -30°
Energy gain per revolution: ≥ 87 keV

Number of Revolutions (n): ≤ 2890
Dee – Dummy Dee Gap: TBD
Dee – Liner Vertical Gap: TBD
Dee – Liner Radial Gap: TBD

2.5 Beam Structure

Micro Structure

Maximum Initial Bunch Phase Width ($\Delta\phi_b$): $\leq 20^\circ$
Maximum Initial Bunch Time Width (Δt_b): ≤ 0.43 ns
Maximum Initial Bunch Proton Number (N_b): $\leq 6.25 \cdot 10^8$ protons
Instantaneous Current (N_b/f_0):
Single Bunch Full Acceleration Time (n/\bar{f}): $22.2 \mu\text{s}$

Macro Structure

Repetition rate: 1000 Hz
Average current: $\leq 6.25 \cdot 10^{11}$ protons/s

2.6 Vacuum System

Configuration: beam chamber and cryostat shall maintain separate vacuums against atmospheric pressure

Operating Beam Chamber Pressure: $\leq 1.0 \cdot 10^{-6}$ T

Beam Chamber Pumping Speed: $\leq 500 \ell\text{s}^{-1}$

Beam Chamber Pumping System: turbomolecular pump with external roughing pump

Cryostat: no direct pumping; roughing via inter-stage of beam chamber turbo pump

Cryostat Helium Leak Requirement: no detectable signal, 1 hr accum. @ $1.0 \cdot 10^{-9} \text{T}\ell\text{s}^{-1}$

2.7 Cryogenics

Cryogenic states: warm, cool down, stand by, cold, warm up

Operating Temperature: 4.5 K

Standby Temperature: TBD

Steady State Heat Load:

Helium: TBD

Nitrogen: TBD

Current leads: TBD

Cryogen Supply: Closed system, batch fill as necessary

Cool Down Rate:

Warm to stand by: TBD

Standby to cold: TBD

LN2 reservoir: TBD ℓ

LHe reservoir: TBD ℓ

2.8 Mechanical Support

Skid Mounted

Transportable by truck

Maximum skid weight : TBD

Maximum dimensions: TBD

2.9 Dose and Field

Minimum Field: TBD

Maximum Field: 20 cm × 20 cm

Maximum Dose: 8 Gray/min

2.10 Beam Dump

TBD

3.0 System Design Description

3.1 Reference Configuration

Machine Type: Isochronous cyclotron

Final Energy: 250 MeV ± 0.25 MeV

Energy Spread: $|\Delta E/E| \leq 0.1\%$

Ion Species: H⁺

Extraction Efficiency: $\geq 99.9\%$

External Proton Beam Intensity:

Minimum: 0.9 emA

Maximum: 1.1 emA

Cyclotron Resonance Conditions

The isochronous central field shall be $B_0 = 5.5T$.

The proton cyclotron resonance frequency shall be $\omega_0 = 84.5$ MHz.

The RF acceleration is on harmonic 1: $\omega_{rf} = \omega_0$

3.2 Reference Magnetic Geometry

A median plane cross-sectional view showing the pole profile of the compact, high field, $K_{\text{bending}}=250$, isochronous cyclotron is shown in Fig. 3.1 and a table of the iron yoke coordinates is given in Table 3.1. The iron pole shape coordinates are shown in Fig. 3.2.

HISCC (Megatron) Final Report

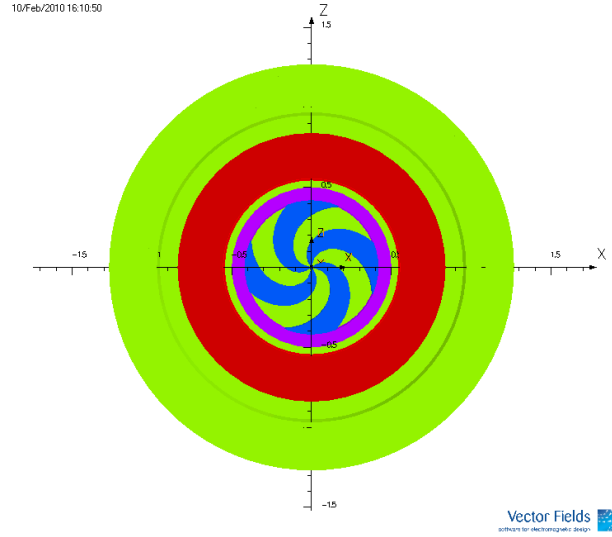


Fig. 3.1 A median plane cross-sectional view showing the pole profile of the compact, high field, $K_{\text{bending}}=250$, isochronous cyclotron is shown. [Reference Opera 3D Model is 3D31f]. Iron of model 3D31f has a circumferentially continuous cylindrical skirt within $0.419 \text{ m} < r < 0.500 \text{ m}$. The pole spiral limited by the skirt at $r=0.419 \text{ m}$ is $\theta=r/(1.01*0.419/2)$.

Table 3.1 Iron Point Coordinates, Model 3D31f.

Model	3D31f	
Point	R (m)	Z (m)
1	0.013	0.015
2	0.013	0.512
3	0.952	0.512
4	1.269	0.322
5	1.269	0.000
6	0.969	0.000
7	0.969	0.262
8	0.500	0.262
9	0.500	0.015
10	0.419	0.015
11	0.419	0.262
12	0.419	0.015
13	0.013	0.015

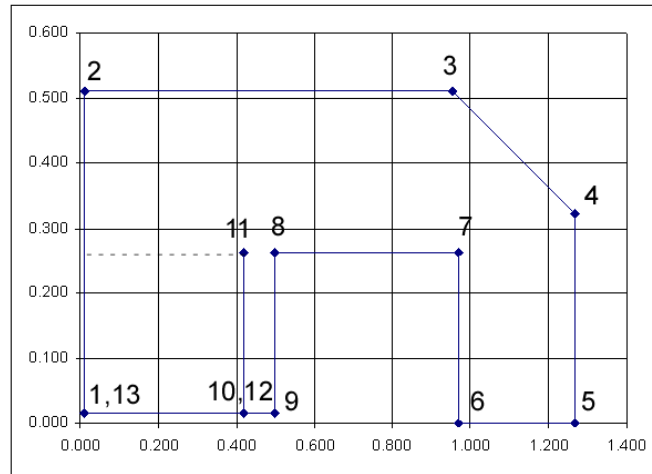
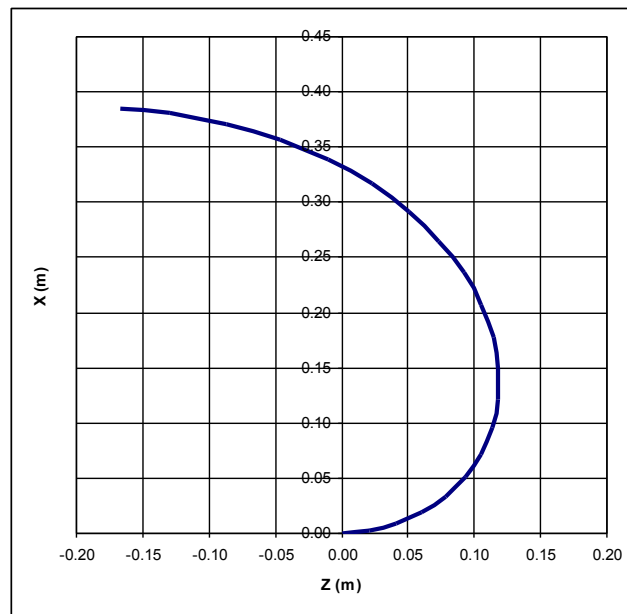


Fig. 3.2 Iron Point Definitions

The spiral pole shape coordinates are given in Table 3.2 and these are shown plotted in Fig. 3.3.

Table 3.2 Spiral hill edge coordinates, Model 3D31f.

Model 3D31f			
R (m)	theta	Z (m)	X (m)
0.000	0.00	0.000	0.000
0.021	0.10	0.021	0.002
0.042	0.20	0.041	0.008
0.063	0.30	0.061	0.019
0.085	0.40	0.078	0.033
0.106	0.50	0.093	0.051
0.127	0.60	0.105	0.072
0.148	0.70	0.113	0.095
0.169	0.80	0.118	0.121
0.190	0.90	0.118	0.149
0.212	1.00	0.114	0.178
0.233	1.10	0.106	0.207
0.254	1.20	0.092	0.237
0.275	1.30	0.074	0.265
0.296	1.40	0.050	0.292
0.317	1.50	0.022	0.317
0.339	1.60	-0.010	0.338
0.360	1.70	-0.046	0.357
0.381	1.80	-0.087	0.371
0.402	1.90	-0.130	0.380
0.419	1.98	-0.167	0.384


Fig. 3.3 Pole spiral shape (Model 3D31F coordinate system.)

3.3 Isochronous Cyclotron Requirements

3.3.1 Isochronous Condition

This superconducting magnet shall provide the magnetic guide field for a 250 MeV proton isochronous cyclotron. An isochronous cyclotron has a fixed RF driving frequency in which the relativistic mass increase of the protons is compensated by an increase in the magnetic field with radius. Strong focusing accelerators are governed by the requirement that the field index k , as defined by

$$k \equiv -n = r dB / B dr > 0$$

shall exceed zero (as indicated) over the whole acceleration interval in the radial coordinate r . Corresponding, the magnetic field must increase with radius, as shown in Fig. 3.4.

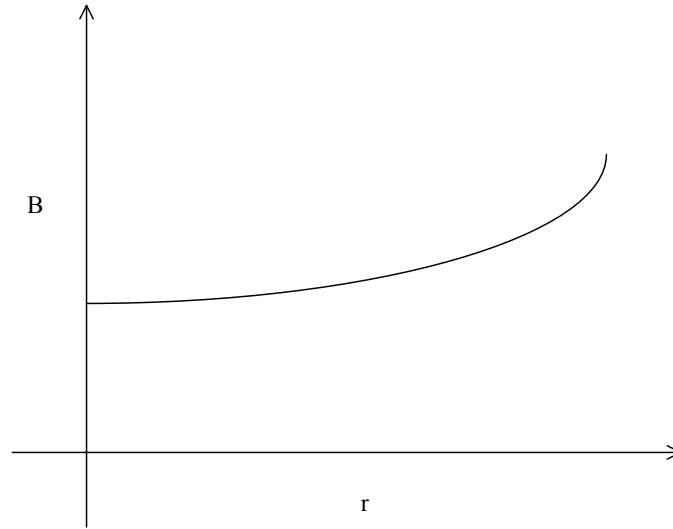


Fig. 3.4 The scheme of the magnetic field B vs. radius r of an isochronous cyclotron.

The field index k is determined by a combination of fields from superconducting coils and magnetized iron. This guide field has two important symmetries. There exists a plane, which shall be known as the median plane, on which $B_r=0$ for all r . There exists an axis, which shall be known as the symmetry axis, for which $B_r=0$ for all z . The symmetry axis is normal to the median plane.

Isochronous cyclotrons require azimuthal variation in the field strength (Flutter) to provide a strong focusing effect and confine the ions in the median plane.

The relationship between total energy E , momentum p , and rest energy E_0 is

$$E^2 = p^2 c^2 + E_0^2$$

For protons $E_0 = m_p c^2 = 938.272 \text{ MeV}$. The relationship between total energy, kinetic energy and rest energy is

$$E = E_0 + T$$

Where the final proton kinetic energy here is $T_f = 250 \pm 0.25 \text{ MeV}$ by Specification 2.1. These relationships are shown in Fig. 3.5

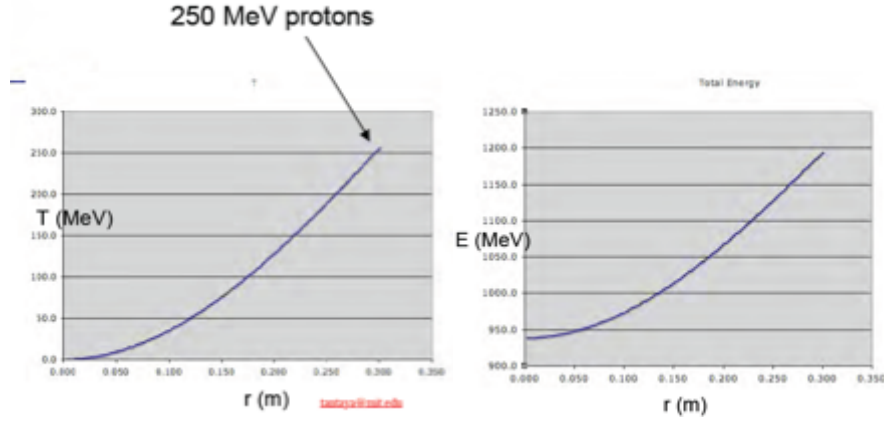


Fig. 3.5 The kinetic energy and the total energy variation with radius in an isochronous cyclotron

The Isochronism condition illustrated in Fig. 3.4 can be stated as

$$B = \gamma B_0$$

where γ is

$$\gamma = (1 + T/E_0)$$

Combining these last two relations we can show that

$$B = B_0 [1 - (r/\alpha)^2]^{-1/2}$$

where

$$\alpha \equiv \frac{E_0}{ecB_0}$$

For protons, taking $B_0 = 5.5T$ from Specification for Cyclotron Resonance Conditions, 3.1.7, we have $\alpha = 0.569$. Further, in the K250-42 isochronous cyclotron, the relativistic γ at final energy is

HISCC (Megatron) Final Report

$$\gamma_f = \frac{M}{M_0} = \frac{E}{E_0} = \frac{E_0 + T}{E_0} = 1 + \frac{250}{938} = 1.267$$

Since the magnetic field varies proportionally to γ we have that

$$B_f = \gamma_f B_0 = 6.97T$$

The Isochronous condition for the K250-42 cyclotron shall be:

$$B = 5.5T[1 - (r/0.569)^2]^{-1/2}$$

The nominal final energy of 250 MeV \pm 0.25 MeV is achieved at a radius of 42 cm.

Isochronous cyclotrons have no phase stability and a precise way of generating and maintaining the field isochronism is required. Figures 3.6 and 3.7 shows a comparison of the ideal isochronous field with the azimuthal average isochronous field over a 45° sector of a hill (3.8) and valley (3.9).

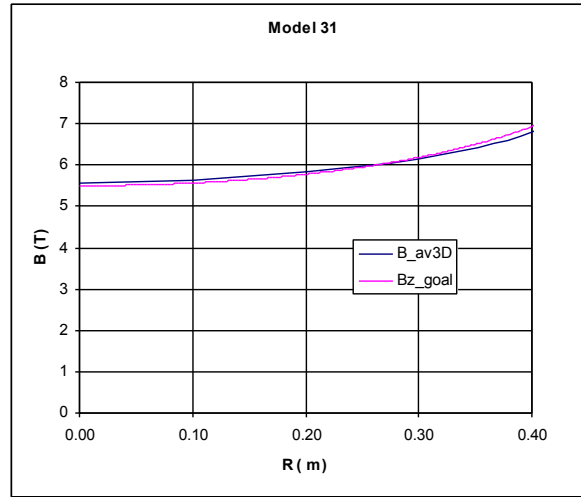


Fig. 3.6 The azimuthal average of the Reference Model 3D31f axial field along a 45° width hill of the K250-42 isochronous cyclotron (B_av3D) is compared with the ideal average field (Bz_goal).

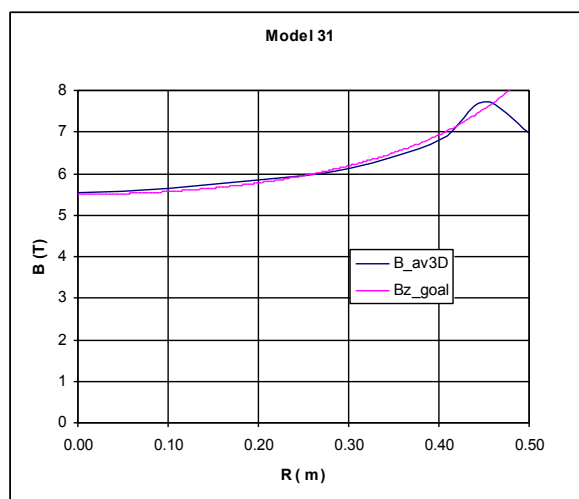


Fig. 3.7 The azimuthal average of the Reference Model 3D31f axial field along a 45° width valley of the K250-42 isochronous cyclotron (B_{av3D}) is compared with the ideal average field (Bz_{goal}).

3.3.2 Flutter

The radial increasing isochronous magnetic field results in an axial (away from the median plane) defocusing of ions during acceleration in an isochronous cyclotron. In order to restore axial focusing, an azimuthally varying magnetic field is introduced through a periodic azimuthal variation in the pole height. The precise spiral geometry is shown in Fig. 3.8.

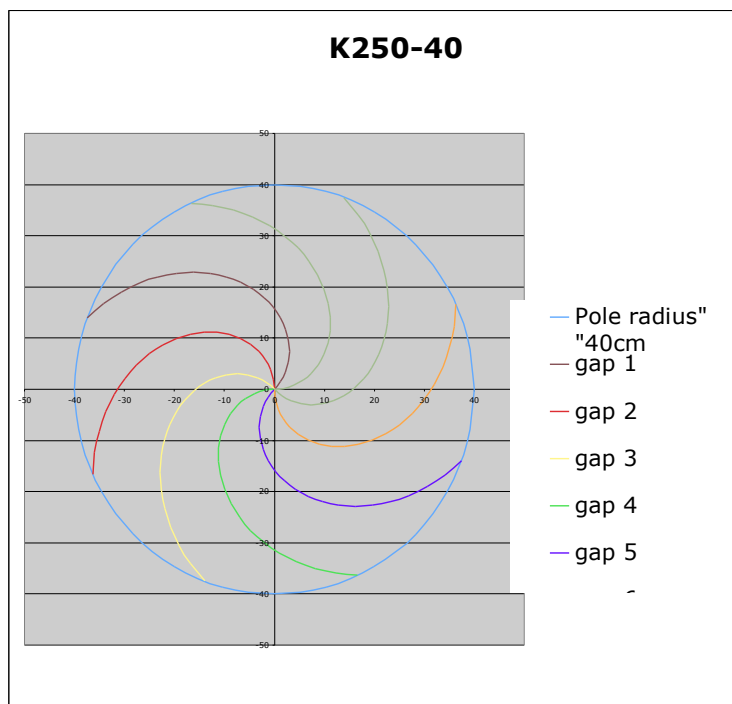


Fig. 3.8 Spiral geometry of the K250 isochronous cyclotron.

HISCC (Megatron) Final Report

The azimuthal formula for the pole edges is $\tau = r/20 + n\pi/4$, $n=1,2,3,\dots,8$. [Note: this must be reconciled with the pole spiral in Specification 3.2].

The parameters of the azimuthal degree τ vs r of gap 1 are shown in Table 3.3 and the parameters of the final revolution are shown in Table 3.4.

Table 3.3 Parameters of the azimuthal degree vs r of gap 1

r	tau	x	y
0	0.7854	0	0
2	0.8854	1.26595977	1.54833648
4	0.9854	2.21011905	3.33397268
6	1.0854	2.79935366	5.30694065
8	1.1854	3.00741138	7.41319613
10	1.2854	2.81537769	9.59550147
12	1.3854	2.212033	11.7943592
14	1.4854	1.19409601	13.9489833
16	1.5854	-0.2336505	15.9982939
18	1.6854	-2.0583535	17.8819233
20	1.7854	-4.2592042	19.5412175
22	1.8854	-6.8076717	20.92022
24	1.9854	-9.6678531	21.966625
26	2.0854	-12.796937	22.6326843
28	2.1854	-16.145773	22.8760573
30	2.2854	-19.659543	22.6605906
32	2.3854	-23.278519	21.9570162
34	2.4854	-26.938909	20.7435578
36	2.5854	-30.57377	19.0064362
38	2.6854	-34.113978	16.740266
40	2.7854	-37.489251	13.9483362

Table 3.4 Parameters of the final revolution $r = 40$ cm

		r=40	
th deg	th rads	x	y
0	0	40	0
15	0.26175	38.6375443	10.3508536
30	0.5235	34.6429915	19.9965782
45	0.78525	28.2884616	28.2800802
60	1.047	20.006843	34.6370645
75	1.30875	10.3623025	38.6344754
90	1.5705	0.01185307	39.9999982
105	1.83225	-10.339404	38.6406098
120	2.094	-19.986312	34.6489155
135	2.35575	-28.271696	28.2968405
150	2.6175	-34.631134	20.017106
165	2.87925	-38.631403	10.3737505
180	3.141	-39.999993	0.02370614
195	3.40275	-38.643672	-10.327953
210	3.6645	-34.654836	-19.976043
225	3.92625	-28.305217	-28.26331
240	4.188	-20.027367	-34.625201
255	4.44975	-10.385198	-38.628327
270	4.7115	-0.0355592	-39.999984
285	4.97325	10.3165015	-38.646731
300	5.235	19.9657734	-34.660754
315	5.49675	28.2549212	-28.313591
330	5.7585	34.6192651	-20.037627
345	6.02025	38.6252482	-10.396644
360	6.282	39.9999719	-0.0474123

Particles experience betatron oscillation in the isochronous cyclotron. The requirements of radial frequency ν_r and axial frequency ν_z are

$$\nu_r = 1.267$$

$$\nu_z > 0.3$$

3.4 Magnet

Magnet type: superconducting split coil, warm iron yoke

Orientation: isochronous cyclotron symmetry axis parallel to gravity.

Return Yoke and Pole: AISI 1008 Magnetic Steel with magnetic properties consistent with modeling

Conductor: NbTi Cable in Channel

The main properties of the magnet are given in Table 3.5

Table 3.5 Parameters of the K250-42 Superconducting Magnet (Reference Model 3D31f)

Parameter	Units	
Coil		
dR	m	0.279
dZ	m	0.097
R1	m	0.550
Z1	m	0.065
Volume (per coil)	m ³	0.117
Jwp	A/mm ²	80
NI (per coil)	MA-t	2.16
Bmax	T	7.71
E (total)	MJ	13.9
Iron Yoke		
Volume (total)	m ³	3.44
Weight (total)	t	27.05
Rmax	m	1.269
Zmax (half)	m	0.512

3.5 Electron Cyclotron Resonance Ion Source

For applications to compact cyclotrons, efficient ion sources are needed. Requirements are stability, sufficient life-time, low gas requirements, high ionization, and for some applications, high ratio of H^+ to H^{2+} . Microwave heating of electrons bypasses the complications of providing for a hot cathode and supplying anode power. It also minimizes impurity generation from exposure of metal wall electrodes to energetic ions in the hot plasma.

3.5.1 Source Design and Assembly

A high brightness ECR proton source, with a nominal current output of 40 mA at 20 kV, has been designed for axial injection into a 7 T superconducting cyclotron. The mechanical design is based upon a 2.54 GHz electron resonant heated plasma in the presence of an axial magnetic field. Microwave heating of electrons bypasses the complications of providing for a hot cathode and supplying anode power. It also minimizes impurity generation from exposure of metal wall electrodes to energetic ions in the hot plasma. Figures 3.9 and 3.10 illustrate the design details.

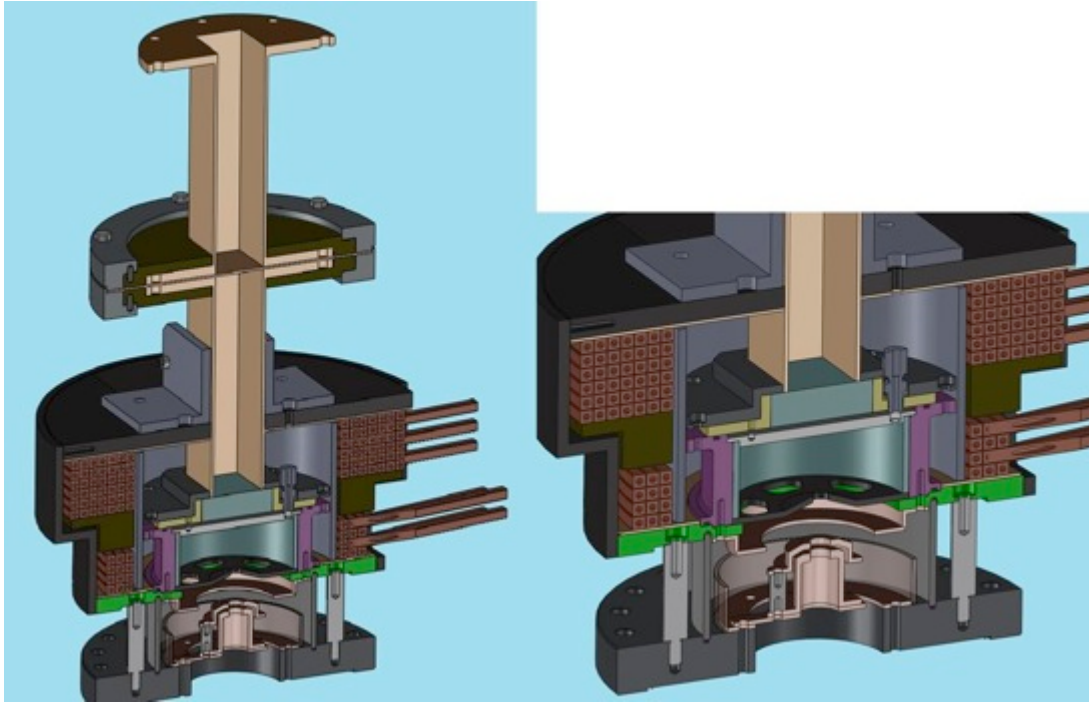


Fig. 3.9 Isometric CAD model view of the ion source.

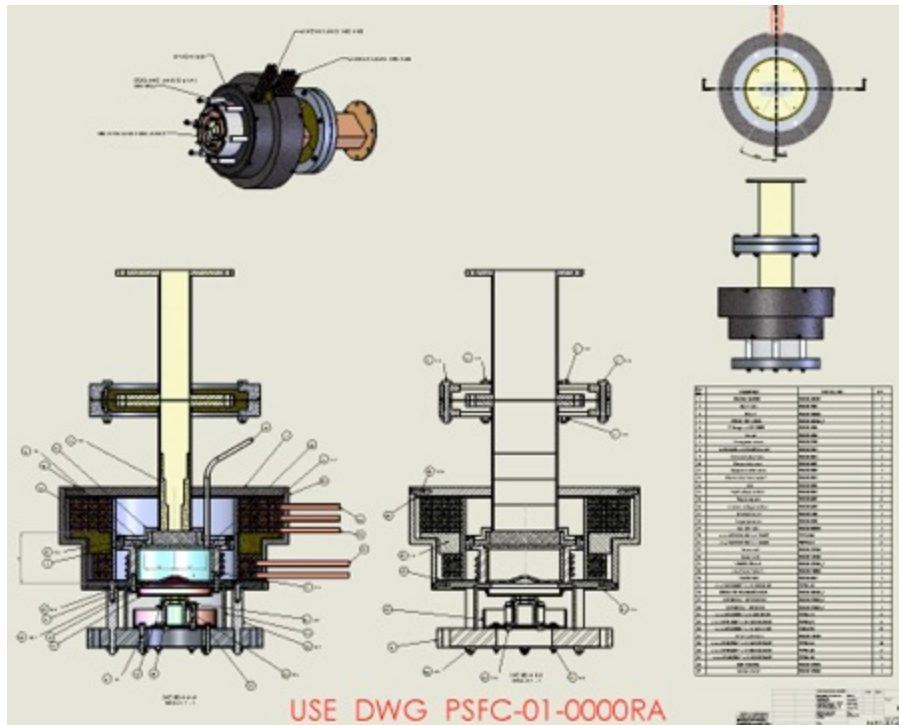


Fig. 3.10 Cross-sectional view of CAD model of the ion source.

Vacuum testing has been completed after addressing issues involving vacuum integrity and high voltage. In particular, seals are now made with elastomers instead of Indium wire while the design of the high voltage break in the waveguide has been modified.

The ionizer utilizes water-cooled coils to generate the 0.08T resonant field. The variable field will allow “tuning” of the electron resonance location. This will allow some control over plasma density and beam divergence. The water-cooled coils have been wound and tested. It should be noted that the purpose of using water -cooled coils is to provide flexibility to the measurements. Once the source parameters have been optimized, a magnetic design using permanent magnets will be used.

A magnetically permeable iron shroud shapes the magnetic field for electron cyclotron resonance near the center of the quartz walled ionization chamber (0.08T) falling to near zero at the exit of the “plasma” grid. See Fig. 3.11

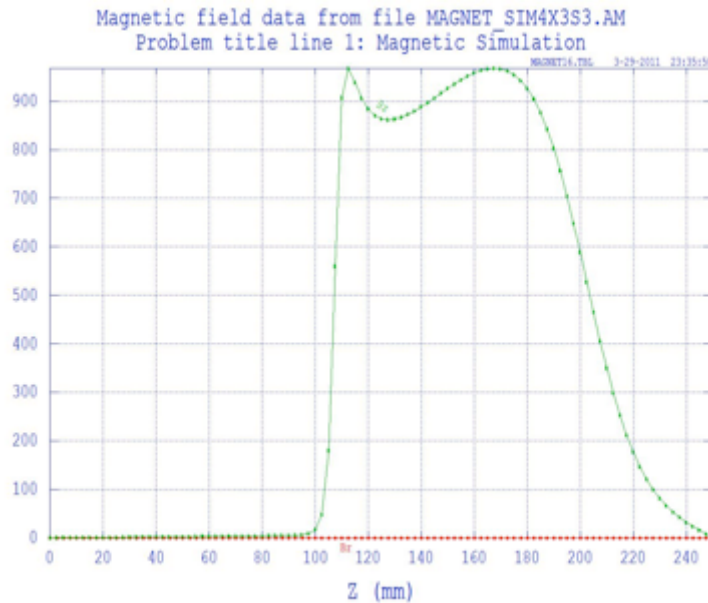


Fig. 3.11 Axial component of B along axis ($r = 0$). Exit of ionizer is at 100 mm.

All mechanical components of the source have been fabricated and are shown in Fig. 3.12. The extraction electric field is formed between a “plasma” grid (Fig. 3.13), which is an intermediate copper grid biased negatively to inhibit downstream electrons, and a grounded exit grid. The grid arrangement can be identified at the base of Fig. 3.9. The water-cooled coils have been wound and operated at full current. The high voltage break in the waveguide has been tested at 28 kV.

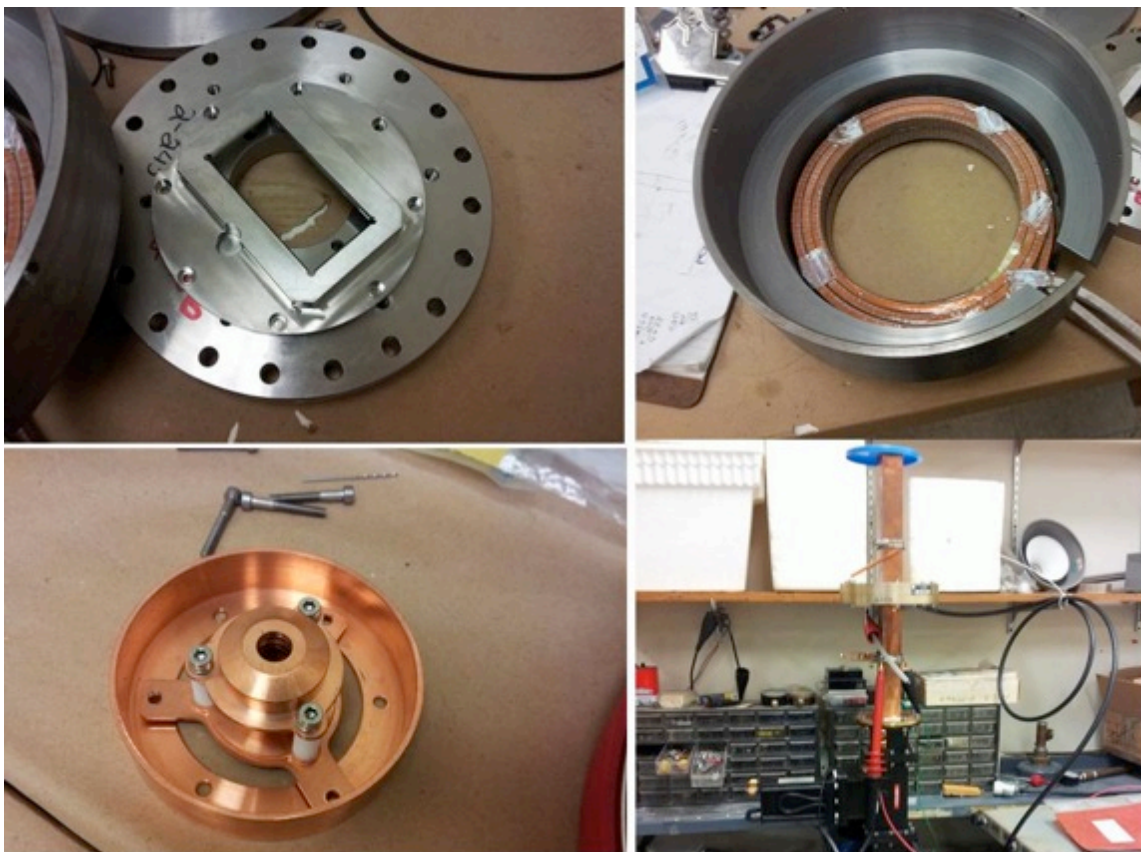


Fig. 3.12 Main components of the ECRS ion source. At top left, the sapphire window in the microwave waveguide. At the top right the magnetic shield with the small coils. Bottom left shows the extractor. Bottom right shows the apparatus for testing the HV microwave source and the dummy load.



Fig. 3.13 Two versions of magnetically permeable “plasma” exit grids.

3.5.2 Power Supplies

The RF generator is in-house. The equipment consists of 1.2 kW, 2.5 GHz generator with dummy load and circulator. It has been operated at low power into a dummy load.

RF leakage at waveguide joints has been quantified with a field meter. We may need a 3-stub tuner for Z matching of the ionizer chamber to the RF source. However, our experience is that once the plasma has been created, the plasma load removes the need for matching network. We may need it only for the initial breakdown.

The extraction power supply (30 kV, 50 mA), electron suppressor supply, and the magnet power supplies are also in house.

The assembled ion source mounted on the superconducting test magnet with the RF generator on top is seen in Fig. 3.14 along with the control rack with power supplies.



Fig. 3.14 Equipment assemblies. At left, ion source with RF assembly mounted on diagnostics flange atop the superconducting test magnet. At right, the rack-mounted ion source power supplies.

3.5.3 Characterization of the Ion Beam

The ion source will be placed on top of a 7 Tesla superconducting magnet test facility available for this program (Fig. 3.14). Figure 3.15 and 3.16 show the magnetic field lines and the magnetic field contours, respectively, for a source with a magnetic shield.

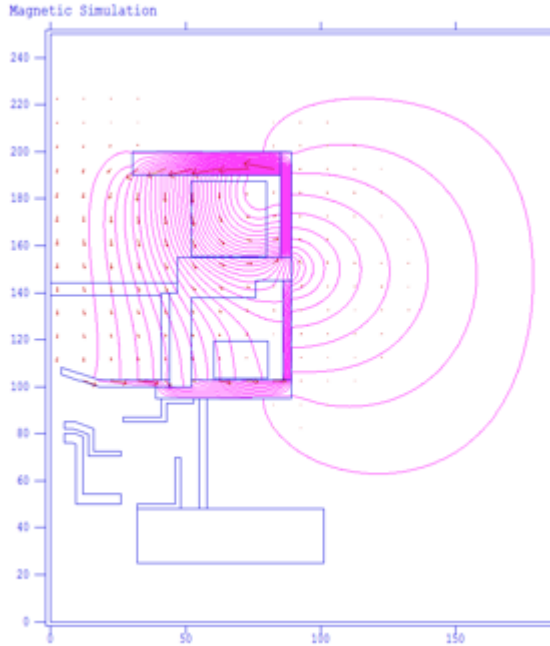


Fig. 3.15 Magnetic field surrounding the ion source, with magnetic shielding.
Surface: Magnetic flux density norm (T) Contour: Magnetic flux density norm (T)

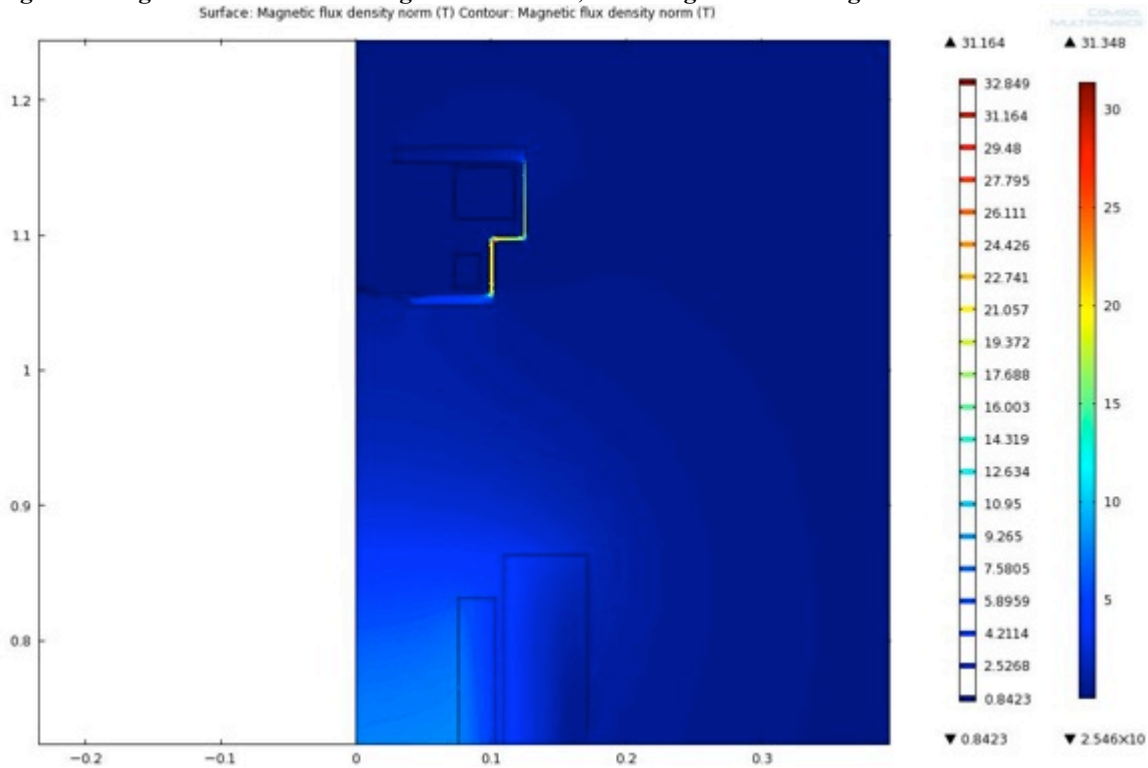


Fig. 3.16 Magnetic field contours of the superconducting magnet in the region below the ion source.
The magnetic shield of the ion source can be seen in the top left of the figure.

We are in the process of modeling the source. The most important information that we expect to obtain is the composition of the extracted ions (protons versus molecular hydrogen ions), as well as ion temperature. Initially, the extracted beam intensity and shape will be monitored with a retractable, segmented Faraday cup diagnostic which has

just been fabricated. These measurements will allow us to “tune” the ion source.

Once ion source-extractor operation is documented, the beam will be injected into the 4-inch bore of the large magnet. Diagnostics placed inside the magnet bore will be used to characterize beam emittance. The characteristics of the ion beam to be measured include beam intensity, proton fraction, and emittance, and these will be compared with simulations. Modeling of the plasma generator is described below.

3.6 Axial Injection

The axial injection will be done with a spiral inflector. At the time of the project termination work on this component had not begun yet. The elements to be designed, modeled, and fabricated include:

1. Geometry
2. Buncher
3. Intensity Modulation
4. Focusing Elements

3.7 Acceleration

RF System:

2 Dees in Valleys

Design Peak Electric Field: TBD

Dee – Dummy Dee Minimum Gap: TBD

Dee – Liner Vertical Minimum Gap: TBD

Dee – Liner Radial Minimum Gap: TBD

Frequency (f_0): 84.5 MHz

Resonator Type: 1/4 wavelength structure

Harmonic: $h=1$ (first harmonic)

RF drive: Programmable waveform generator, broadband amplifier, phase locked to rotating condenser drive

Central Region:

Spiral Inflector Maximum chimney diameter: TBD

Chimney Offset: x TBD y TBD

Gap 1 Spacing: TBD mm

Gap 1 Magnetic Field: TBD

Spiral Inflector Voltage: TBD

Acceleration:

Number of Revolutions (n): 2000

Bunch Design Phase Error: 0°

Dee Width 45°

Nominal Dee Voltage (V_0): 82 kV

Average Energy gain per turn ($4eV_0\sin 22.5^\circ$): 125.6 keV

Proton Gamma at 250 MeV: $\gamma=1.267$

3.8 Beam Structure

Initial Structure

Initial RF period (84.5 MHz): 11.8 ns
Maximum Initial Bunch Capture Phase Width($\Delta\phi_b$): $\leq 5^\circ$
Maximum Initial Bunch Time Width (Δt_b): 0.69 ns
Number of Capture Bunches per acceleration cycle: 1
Req. Captured Protons per Bunch (N_b): 7.4×10^6 protons

Final Structure

Repetition rate: CW
Macro Duty Factor: TBD
Nominal Design Current: 6.25×10^{15} protons/s

Intensity Control:

TBD

Beam Stop

Central region bias stop in TBD RF periods

3.9 External Beam Matching

Extraction Efficiency:

$\geq 99.9\%$, as measured from the internal H⁺ beam current at full energy radius to external H⁺ beam current on first scattering element.

Match Point: TBD

Horizontal Emittance at match point: TBD

Vertical Emittance at Match point: TBD

Radiation Requirements due to Non-extracted Beam

Reference Analysis for Neutron Production rates by lost beam: TBD

Estimated Cryostat Neutron heat load: TBD

Primary beam peak power: 0.25 MW ($P = E \times I = 250 \text{ MeV} \times 1 \text{ emA}$)

Primary beam cryostat neutron heat load: TBD

Primary beam Quasi-Steady-State Cryostat Neutron heat Load: TBD

Primary beam Quasi-Steady-State Cryostat Neutron Power: TBD

3.10 Vacuum System

Configuration: beam chamber and cryostat shall maintain separate vacuums against atmospheric pressure

Operating Beam Chamber Pressure: $\leq 1.0 \times 10^{-6}$ Torr

Beam Chamber Pumping Speed: 2000 ℓs^{-1}

Beam Chamber Pumping System: turbomolecular pumps with external roughing pumps

Cryostat: no direct pumping; roughing via inter-stage of beam chamber turbo pump

Cryostat Helium Leak Requirement: no detectable signal, 1 hour accumulation test at sensitivity level of 1.0×10^{-9} Torr- ℓs^{-1}

3.11 Cryogenics System Design

Cryogenic states: warm, cool down, stand by, cold, and warm up

Operating Temperature: 4.5 K

Standby Temperature: TBD

Steady State Heat Load: TBD

HISCC (Megatron) Final Report

Helium: TBD
Nitrogen: TBD
Current leads: TBD
Cryogen Supply: closed loop thermal-siphon
Cool Down Rate:
 Warm to stand by: TBD
 Standby to cold: TBD
LN2 reservoir: TBD
LHe reservoir: TBD
Provision for rapid initial Cooldown with force flow LN2
Provision for rapid final Cooldown with force flow LHe

The schematic layout of the Megatron cryogenic systems is shown in Fig. 3.17. The cryogenic system includes three independent, but interconnected liquid helium cryostats. The first of these cryostats, shown towards the lower left-hand side of the figure is enclosed within the Megatron's iron yoke and contains the superconducting cyclotron magnet in a liquid helium bath. The second cryostat, shown towards the upper right-hand side of the figure, is equipped with a pair of 3-stage Daikin CG310SC cryocoolers; this cryostat is used to recondense boil-off helium gas from the magnet cryostat and provides for closed-loop operation of the cooling circuit. The third cryostat, shown towards the lower center of the figure, contains the magnet current leads, which can provide up to 4000 A operating current to the magnet.

Each cryostat contains three, nested, cylindrical shells. The outer most shell is a vacuum boundary that permits the internal cryogenic components to operate within a thermally-insulating, vacuum environment. The intermediate shell, both in terms of placement and temperature, limits the radiant heat load on the lowest temperature components and is used to intercept most of the heat conducted from room temperature along structural supports within the cryostat. The inner-most shell houses the liquid helium coolant needed for stable operation of the Megatron superconducting coils.

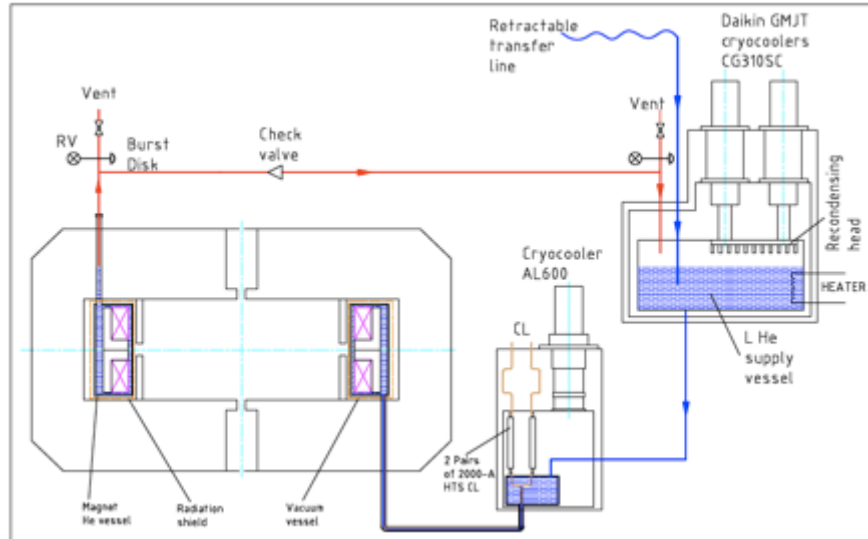


Fig. 3.17 Schematic of the three liquid helium cryostats used to cool the Megatron cryogenics systems.

Figure 3.18 illustrates the design for the current lead cryostat. In this figure, rather than section the solid model, various portions of the outer shells are either suppressed or made semi-transparent to reveal the full system configuration. The magnet current leads are cooled in two stages. The higher temperature portion of the leads consists of copper buswork. The dominant heat load on the cryogenic system is caused by resistive dissipation within and heat conduction from room temperature along this portion of the lead. The combined heat load from the copper portion of the current leads, approximately 330 W, accounts for the bulk of the 425 W heat removal capacity available at 65 K from the single-stage, Cryomech AL600 cryocoolers installed in the current lead cryostat for this purpose. Table 3.6 summarizes all of the anticipated heat loads on this cryocooler.

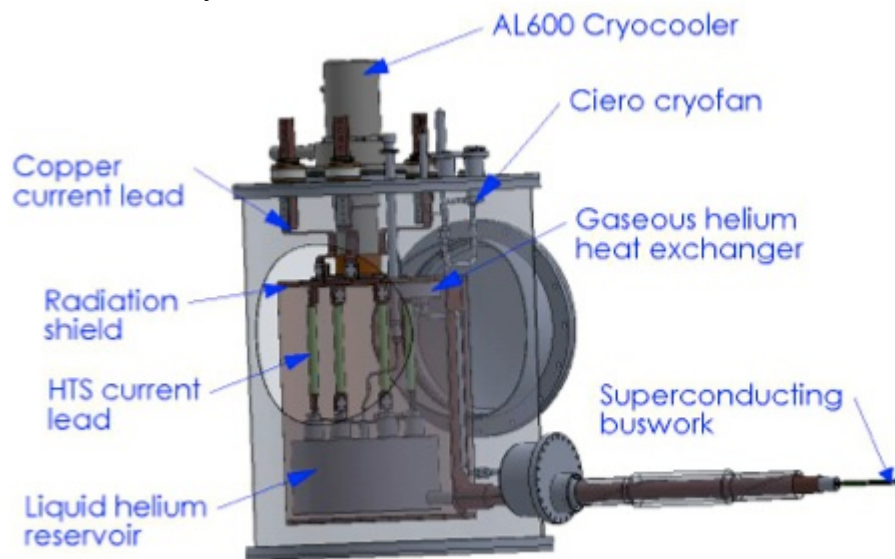


Fig. 3.18 Semi-transparent solid model for the current lead cryostat.

The lower temperature portion of the magnet current leads consists of a pair of 2000 A high temperature superconductor (HTS) current leads manufactured by HTS-110. Recondensed helium from the Daikin cryocoolers is directed to the current lead cryostat where it cools the lower ends of the HTS leads before continuing to the magnet cryostat, along the same cooling channel that contains the superconducting bus work, which connects the HTS leads to the magnet. The use of HTS leads limits the heat load on the liquid helium circuit due to the current leads to slightly less than 1 W.

Table 3.6 Anticipated heat load at 65 K on the Cryomech cryocooler in the current lead cryostat.

Heat source	Watt
MLI (300-70) K for one cryostat	2.1
Supports of the cold mass of one cryostat	0.5
Shield supports for one cryostat	0.5
Shield and support subtotal for one cryostat	3.1
Shield and support subtotal for two cryostats	6.2
Instrumentation wiring	1.0
Current lead supports	4.0
Thermal conduction along, and Ohmic generation in copper current leads	332
Total	343

The radiation shield in the current lead cryostat is equipped with a helium gas heat exchanger that provides 65 K helium gas, which is used to cool the radiation shield for the magnet cryostat. Flow through this loop is created using a Cierzo cryofan mounted near the heat exchanger outlet, as shown in Fig. 3.18. This gaseous cooling loop is designed with sufficient capacity to accommodate heat loads due to thermal radiation from the room temperature walls of the magnet cryostat and from thermal conduction along the magnet vessel structural supports and its instrument wiring. The gaseous cooling circuit and its return lines are similarly connected to the thermal radiation shield that surrounds the liquid helium filled current bus that connects the current lead and magnet cryostats.

The general arrangement of the helium recondensing cryostat is illustrated in Fig. 3.19a, while Fig. 3.19b shows a digital image of one of the Daikin cryocoolers following removal from its shipping container. The use of cryocoolers in the Megatron's cryogenic design greatly simplifies the operation and control of the system. Cooling at the first stage of the cryocoolers is more than sufficient to remove the anticipated 14 W heat load on the radiation shield at a temperature below roughly 50 K. Table 3.7 and Table 3.8 summarize the anticipated heat loads at 4.3 K on the liquid helium cooling loop. Table 3.7 lists the anticipated heat loads from the current lead and magnet cryostats, while Table 3.8 lists the anticipated heat loads from the helium recondensing cryostat. The total anticipated heat load on the liquid helium circuit in the absence of cyclotron beam is roughly 2.5 W, while the full recondensing power provided by the Daikin cryocoolers is about 10 W. The remaining, approximately 7.5 W of third-stage cooling power is available to accommodate nuclear heating of the magnet due to imperfect beam

extraction during operation of the Megatron, as well as to provide design margin against unanticipated heat loads. The use of a closed-loop, recondensing liquid helium circuit provides the magnet with sufficient heat transfer to thermally stabilize the magnet and keep its internal temperature low.



Fig. 3.19 a) Semi-transparent solid model for the helium recondensing cryostat, and b) digital image for one of the Daikin three-stage cryocoolers.

Table 3.7 Anticipated heat load at 4.3 K on helium circuit due to the current lead and magnet cryostats.

Heat source	Heat load, W
Radiation (70-4) K	0.098
He gas convection (70-4) K	0.39
Axial supports (four)	0.02
Radial supports (three)	0.041
Joints at 3692 A (2x2)	0.29
Instrumentation wiring (70-4) K	0.10
Subtotal	0.94
Subtotal with 20% margin	1.13
Current leads 3692 A (two pairs)	0.96
Grand total	2.09

Table 3.8 Heat load at 4.3 K on helium circuit due to helium recondensing cryostat.

Heat source	Heat load, W
Thermal radiation (70-4) K	0.012
He gas convection (70-4) K	0.048
Mechanical supports	0.020
Two cryocooler supports (70-4) K	0.220
Retractable helium supply and vent lines	0.060
Instrumentation (including a heater)	0.005
Total	0.365

Thermal analysis of the Megatron's cryogenics heat loads is complete and nearly all cryogenic components have been designed and specified. Most of the required components, with the exception of current lead cryostat and magnet cryostat, have been received at MIT. Performance testing for the incoming equipment is essentially complete. Figure 3.20 shows representative performance data for one of the Daikin CG310SC cryocoolers, which exceeded its contracted 5 W performance specification at less than 4.3 K temperature by roughly 10%.

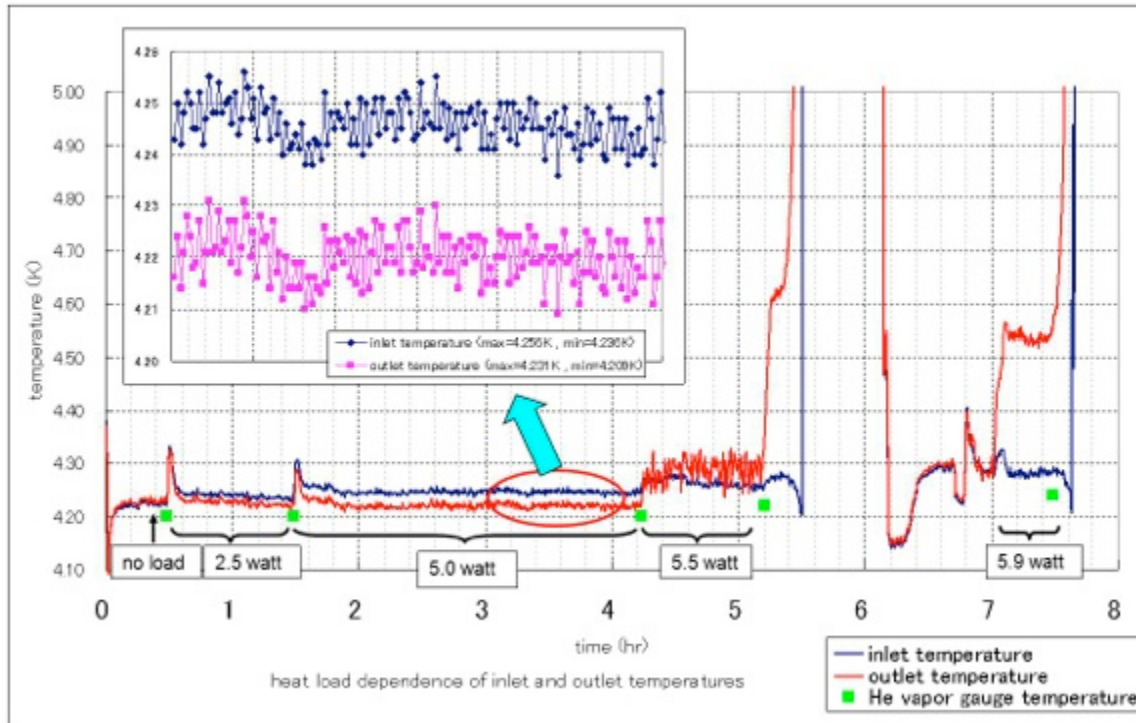


Fig. 3.20 Acceptance test performance data for one of the Megatron's Daikin CG310SC cryocoolers. Both cryocoolers gave similar performance meeting the specification.

4.0 Magnetic Field Design

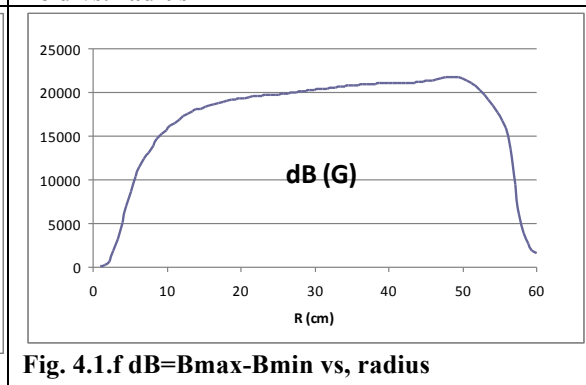
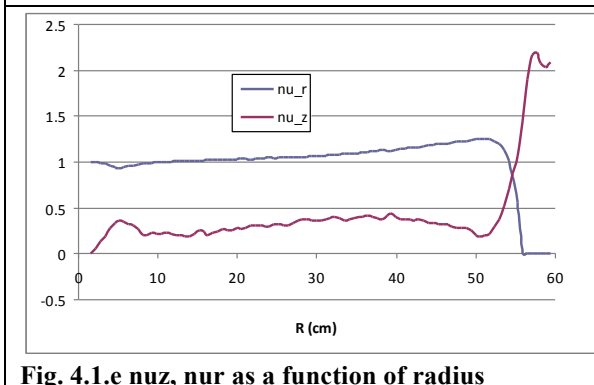
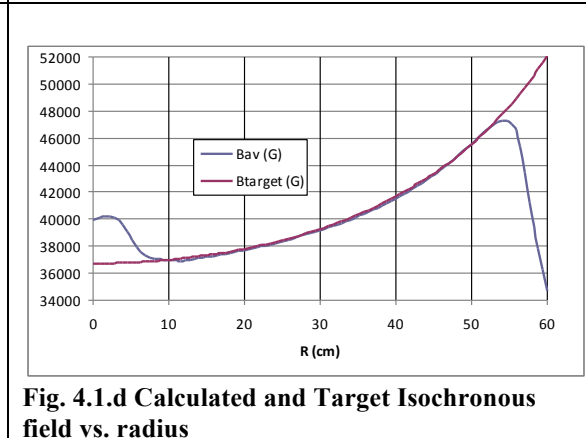
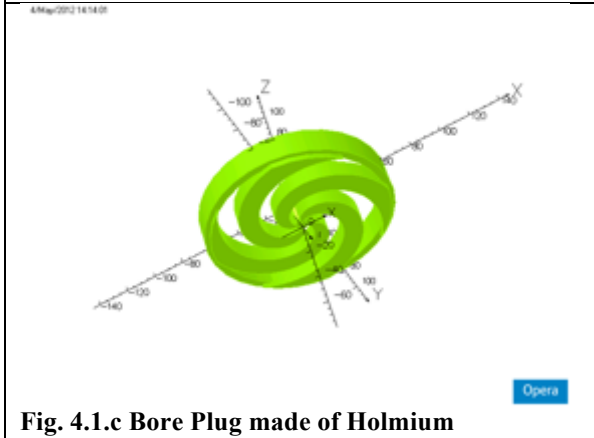
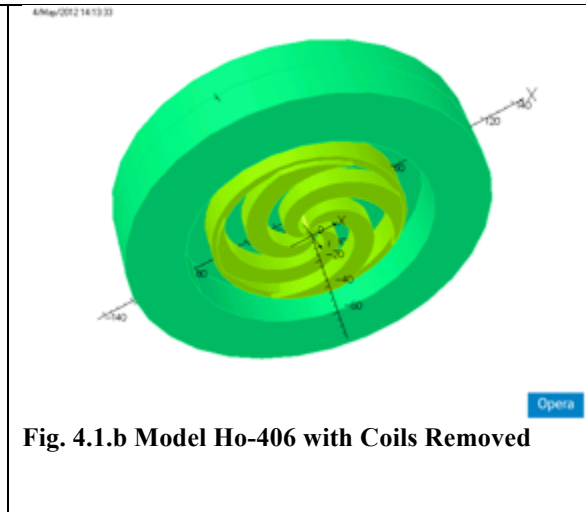
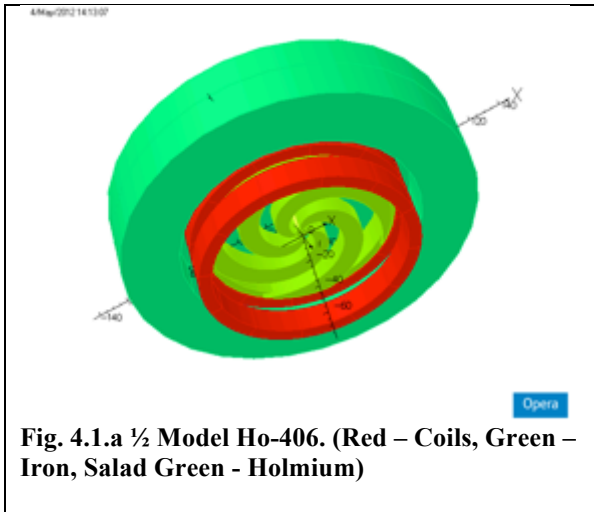
4.1 Magnetic Design with Rare Earth Pole Tips

At the time the project was halted the magnetic design was not completed. A major issue that was still being analyzed was how to provide the required flutter and also achieve a final energy of 250 MeV. An early plan was to consider the use of rare earth magnetic materials, e.g. holmium or gadolinium, as the spiral pole tip material. Basic characteristics and views of Model Ho-416 with hills of the central bore made of Holmium are shown in Table 4.1 and Figures 4.1.a-4.1.f.

HISCC (Megatron) Final Report

Table 4.1 Megatron Model Ho-406.

B0	T	3.67
Rextr	cm	52.0
gamma		1.268
Bex	T	4.66
T	MeV	251
Hill material, temperature		Holmium, <10K
Hill gap	cm	3.0

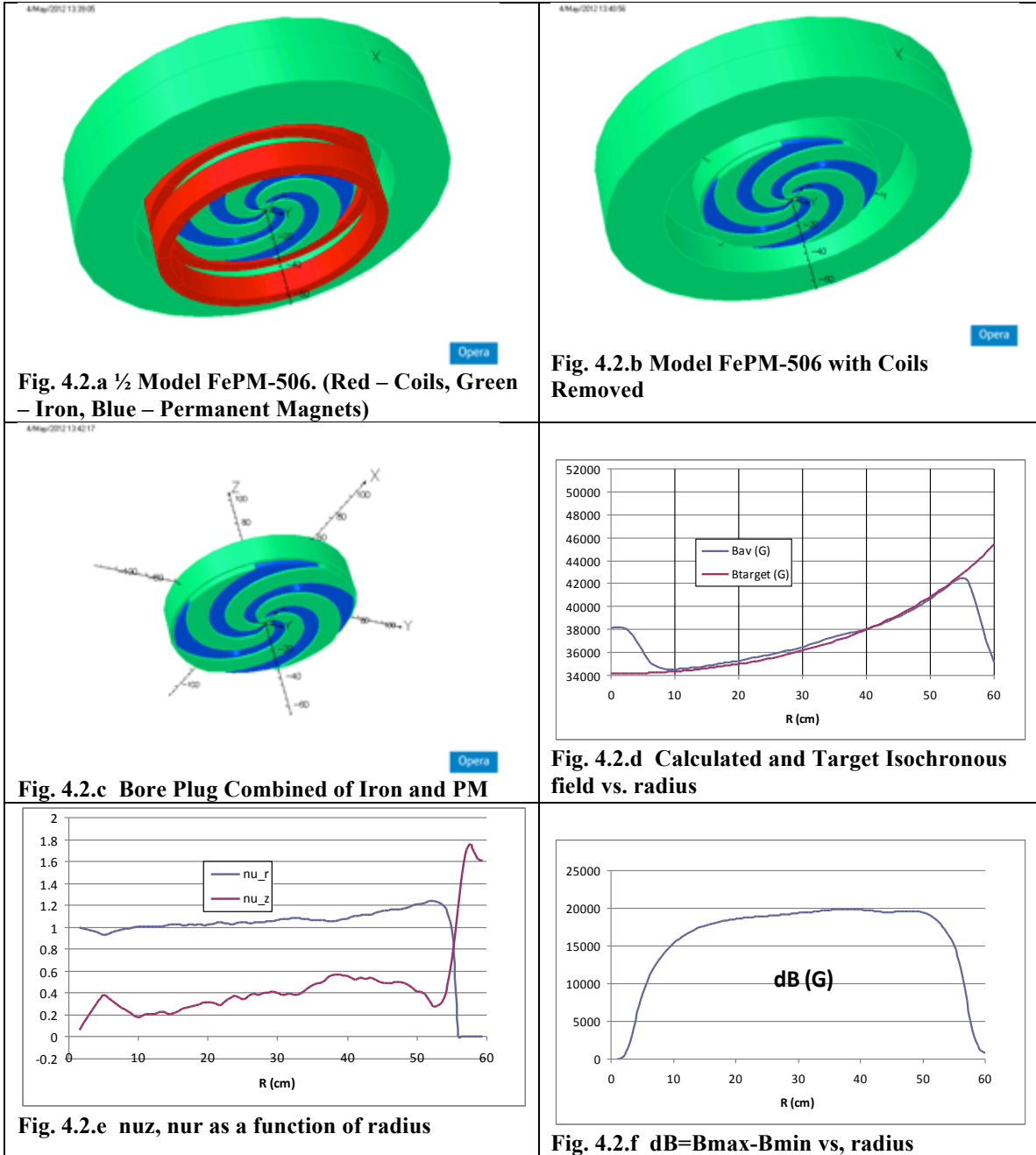


Although these materials exhibit a magnetic saturation much greater than low carbon steel, they must be maintained at a cryogenic temperature to achieve these high values. We also considered using superconducting coils wound around the spiral steel pole pieces to achieve a satisfactory degree of flutter. In both cases this would require designing and building a central pole assembly contained within a cryostat. Note that a cyclotron with cryogenic pole tip construction has never been attempted before. In Model Ho-406 the gap between the hills made of Holmium and maintained at the cryogenic temperature is only 3 cm. This presents a technical challenge that would be very difficult to resolve within the desired timeframe of this project. The use of a pole cryostat requires extra axial space to maintain the vacuum, conduction, and thermal radiation separation needed to maintain a low cryogenic temperature. The extra space required increases the pole gap, thus also reducing the flutter field.

Taking all these issues into consideration we decided, for simplicity and reliability, to retain the use of low carbon steel pole tips. To achieve the required flutter, the final energy had to be reduced, if we were also to maintain the nominal pole diameter and extraction radius. However, even after these concessions the flutter created by the RT iron hills turned out to be insufficient. To increase the flutter we decided to fill the valleys with Permanent Magnets (PM) polarised axially in opposite direction to the field of the background coils. Parameters of Model FePM-506 based on this design are shown in Table 4.2 and Figs. 4.2.a-4.2.f.

Table 4.2 Megatron Model FePM-506

B0	T	3.41
Rextr	cm	52.0
gamma		1.219
Bex	T	4.16
T	MeV	205
Hill material, temperature		Iron+PM, RT
Hill gap	cm	2.5



At this point our work on the magnetic field design was terminated. Would it not have happened we planned to adjust this design to the specified proton beam energy of 250 MeV by increasing the extraction radius by about 5 cm. Preliminary estimates showed that this solution could both provide workable beam dynamics and be realistic from the engineering standpoint.

5.0 Cyclotron Layout

A cross-sectional view of the cyclotron layout is shown in Fig. 5.1. This view shows the location of the split coil pair and their steel yoke support, the cryostat, and several of the tension straps reacting the forces between the magnet and the cold mass against the warm iron. The large vertical cylinder along the centerline, top is the ERIS and spiral inflector, while the vertical centerline cylinder at the bottom is the vacuum port for the beam chamber including a diagnostic probe. The vertical cylinder on the right side of the iron yoke is the vacuum port for the cryostat and integrates with the cold helium gas from the cryostat to return to the recondensing cryostat. The L-shaped tube on the lower right is the liquid helium transfer line which also contains the superconducting bus transferring both liquid and current from the current lead satellite cryostat (refer to Figs. 3.17-3.19 in the Cryogenics System Design (Section 3.10)).

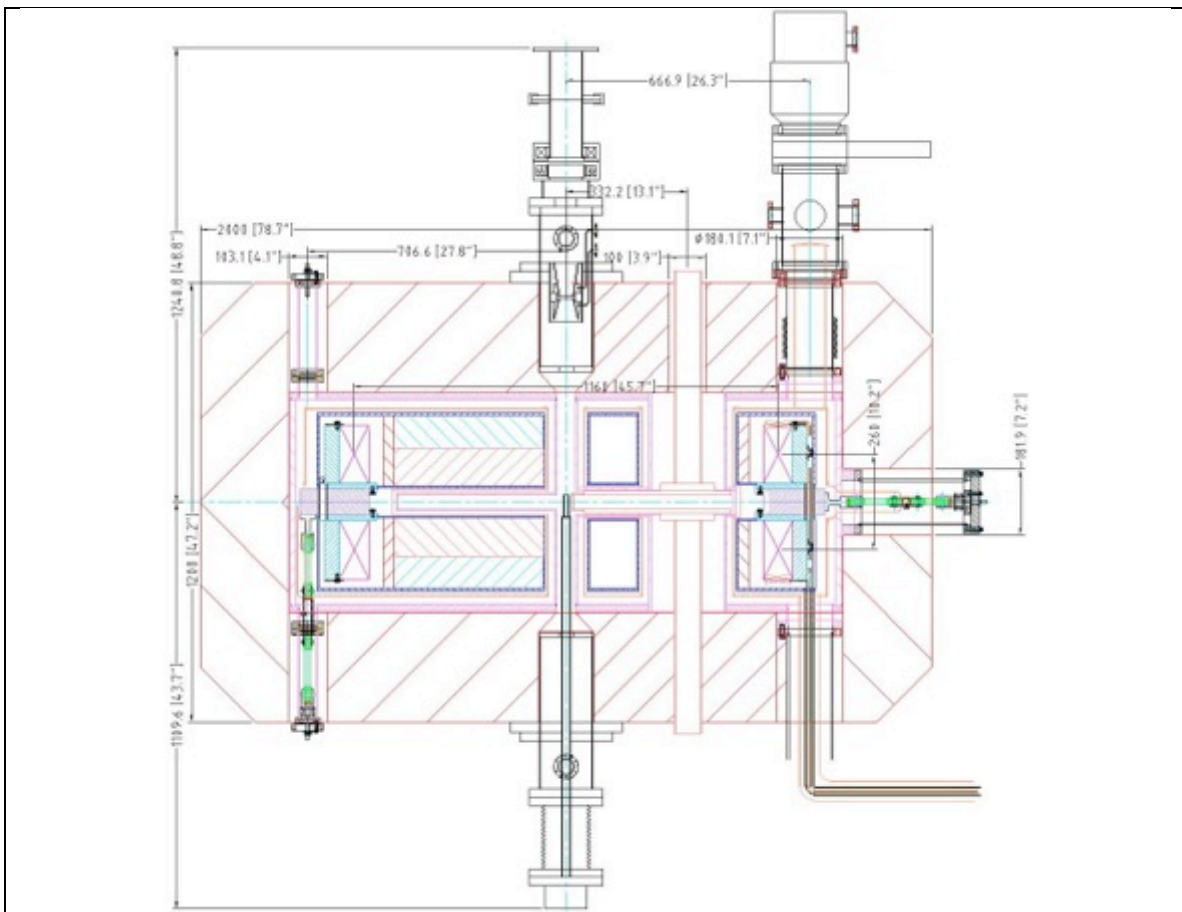


Fig. 5.1 Cross-sectional view of the Megatron cyclotron.

The shape of the spiral pole tips can be seen in Fig. 5.2. Further information about the pole shapes is given in Section 4.1.

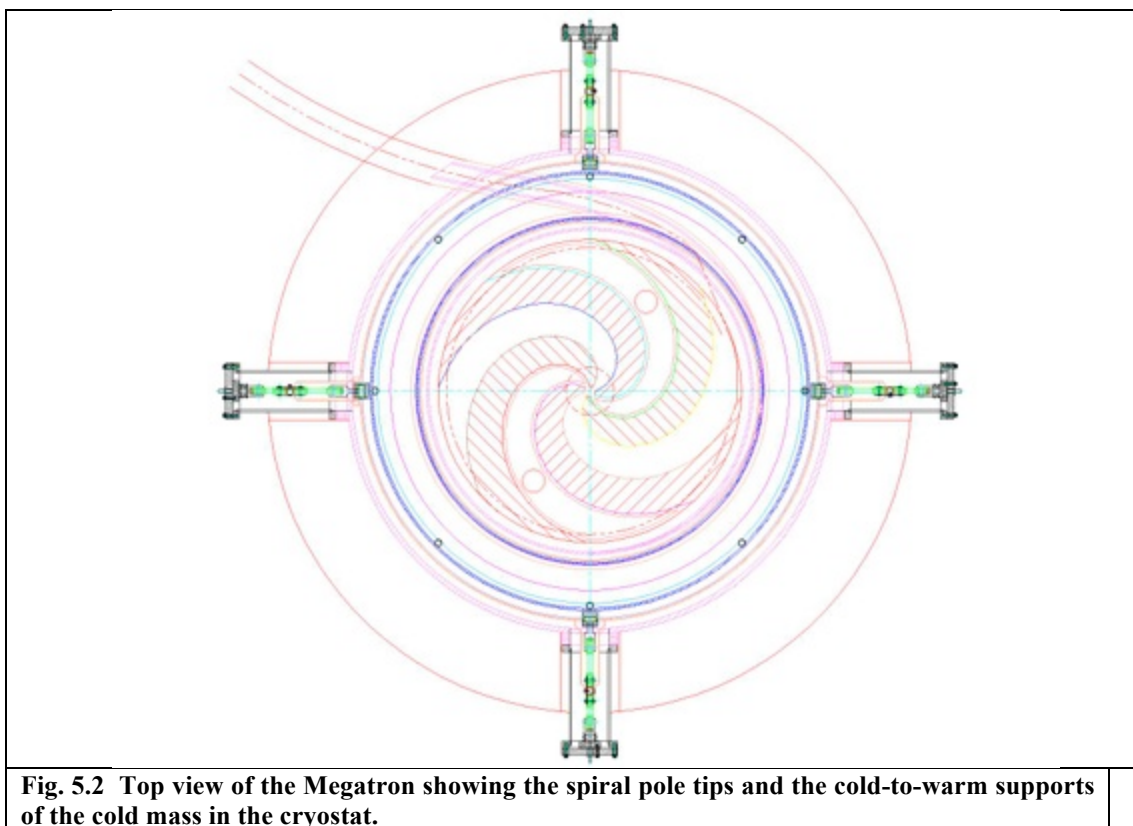


Fig. 5.2 Top view of the Megatron showing the spiral pole tips and the cold-to-warm supports of the cold mass in the cryostat.

Nominal dimensions for the iron yoke, coil location, and steel support yoke are given in Fig. 5.3. Note that these are not necessarily the final dimensions which might have minor deviations from those shown here before being finalized.

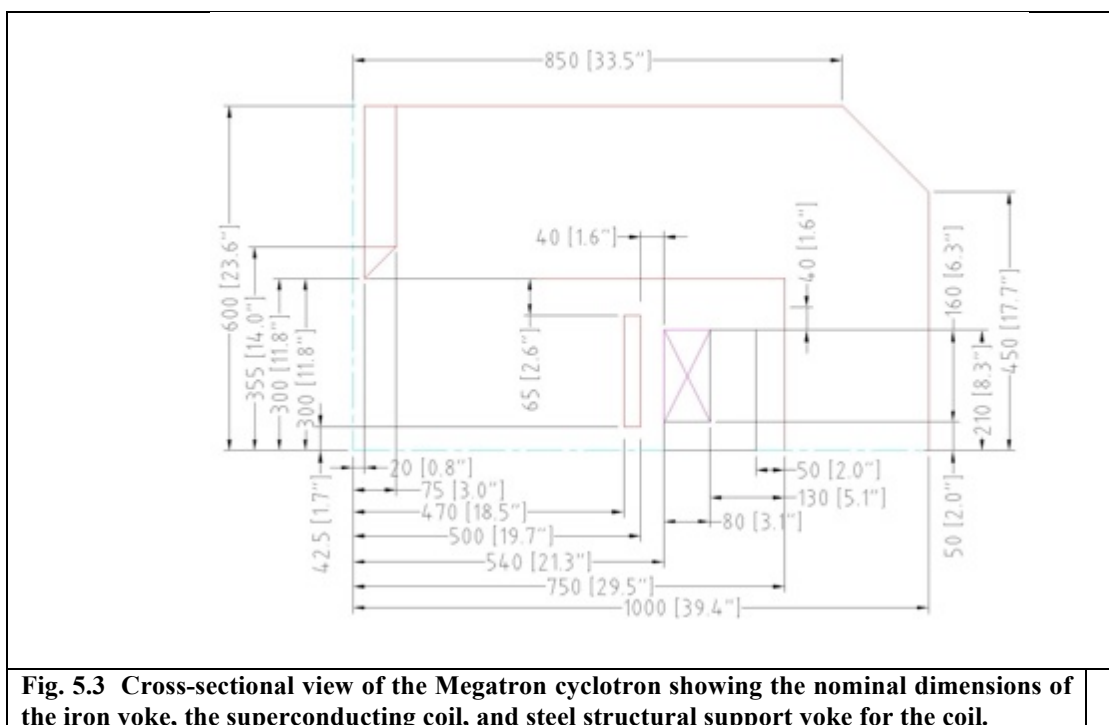


Fig. 5.3 Cross-sectional view of the Megatron cyclotron showing the nominal dimensions of the iron yoke, the superconducting coil, and steel structural support yoke for the coil.

6.0 Magnet Design

Magnet geometry and electrical parameters are given in Table 6.1.

Table 6.1 Winding pack parameters for the Megatron magnet.

Coil Dimensions							
R_{inner} (m)	R_{outer} (m)	Radial Build (m)	Height (m)	Area 1 coil (m^2)	Average Turn Length (m)	Volume 1 Coil (m^3)	Volume 2 Coil (m^3)
0.55	0.65	0.1	0.16	0.016	3.769911184	0.060318579	0.120637158
NI (A-t)	B_{max} (T)			Winding Pack Current Density (A/mm^2)	Length per Coil (m)	Total Conductor Length (m)	
1,232,000	6.1			77.00	1261	2522	

Winding Insulation	mm	0.2	All around
Conductor Area	mm^2	45.08	
Conductor + Insulation Area	mm^2	50.88	
No. Radial Turns		20.4	
No. Axial Turns		16.4	
Total Turns/Coil		335	
Operating Current	A	3,683	

The conductor is a NbTi Cable-in-Channel designed and fabricated by Luvata, Inc., Waterbury CT. This conductor was in production for a different project but it's geometric, magnetic, and electrical characteristics were ideal for use in the Megatron application. This conductor was purchased for the Megatron and resulted in considerable cost savings because the fabrication development was already paid by the other project.

The conductor parameters are given in Table 6.2, and a photograph of the cross-section is given in Fig. 6.1. The conductor was shipped in 5 piece lengths as given in Table 6.3. The measured values of geometry and performance data is given in Table 6.4.

HISCC (Megatron) Final Report

Table 6.2 Strand and Cable-in-Channel conductor design parameters

**ISEULT CIC
Conductor (Luvata)**

Strand		
strand diameter	mm	1.48
Cu/SC Ratio		1.29
Filament Number		468
Avg. Expected Ic at 4.22K and 9.5 T	A	300
Rutherford Type Cable		
No. sc strands		10
Width	mm	7.4
Height	mm	2.7
Cable lay (pitch)	mm	100

Area Sc in 1 strand	mm ²	0.751
Area Cu in 1 strand	mm ²	0.969
Area Sc in 10 strands	mm ²	7.512
Area Cu in 10 strands	mm ²	9.691
Area Cu in Channel	mm ²	24.866
Total Cu area	mm ²	34.557
Total Conductor Area	mm ²	44.248

Conductor-in-Channel		
Final Width	mm	9.2
Final Height	mm	4.9
Corner Radius (4X)	mm	0.75
RRR		>110
Avg. Expected Ic at 4.22K and 9.5T	A	2930
0.2% yield strength	MPa	>250
Overall Cu/SC ratio		4.6
Unit Length Range	m	708-768

HISCC (Megatron) Final Report

Fig. 6.1 Photograph of the NbTi Cable-in-Channel for the Megatron coils.

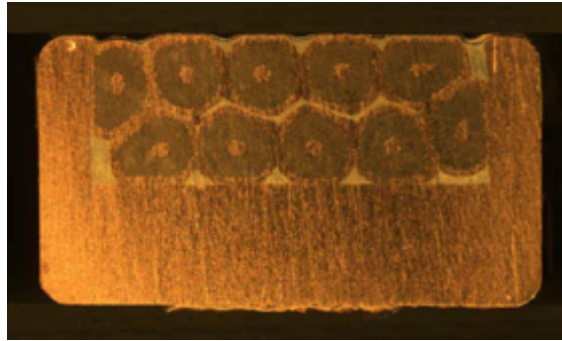


Table 6.3 Conductor piece lengths as delivered

	Meters
Piece 1	706
Piece 2	680
Piece 3	571
Piece 4	479
Piece 5	300
Total	2736
Order Quantity	2500
Invoiced for	2500

Table 6.4 Measured conductor performance parameters

Calculated Ic at 4.2 K											
Spec			9.180 mm	4.866 mm	>0.2 mm	<1% Fil breakage	~17,000 A	~14,000 A	>30	>150	> 200 MPa
Spec Min			9.130	4.816	0.2				30	150	200
Spec Max			9.230	4.916		<1%					
PieceID	Luvata Cable ID	Length	Thickness	Width	Coner Rad.	40mm Bend	Ic (5T)	I (6T)	n (6T)	RRR of Stabilizer	Yield Strength @ 300K
57920-1-1	TYL120	706	9.186	4.875	0.5	Pass	17305	14398	38	167	233
59302-2	TYL149	680	9.189	4.868	0.5	Pass	17381	14461	38	164	239
60095-1-2-1	TYL188	573	9.184	4.874	Pass	Pass	17306	14365	38	165	236
60358-2	TYL191	482	9.188	4.865	Pass	Pass	16384	13472	38	168	225
60358-3	TYL191	357	9.188	4.865	Pass	Pass	16384	13472	38	168	225

* Measurements are the Mean value of Laser Mic

The magnet will use commercial High Temperature Superconductor (HTS) current leads purchased from HTS-110. Use of HTS current leads reduces the 4.5 K cryogenic heat load by about a factor of 5 over the usual vapor cooled current leads. The dimensions of the 2000 A HTS current leads are shown in Fig. 6.2. Since the coil requires 4000A, 2 sets of these leads will be used.

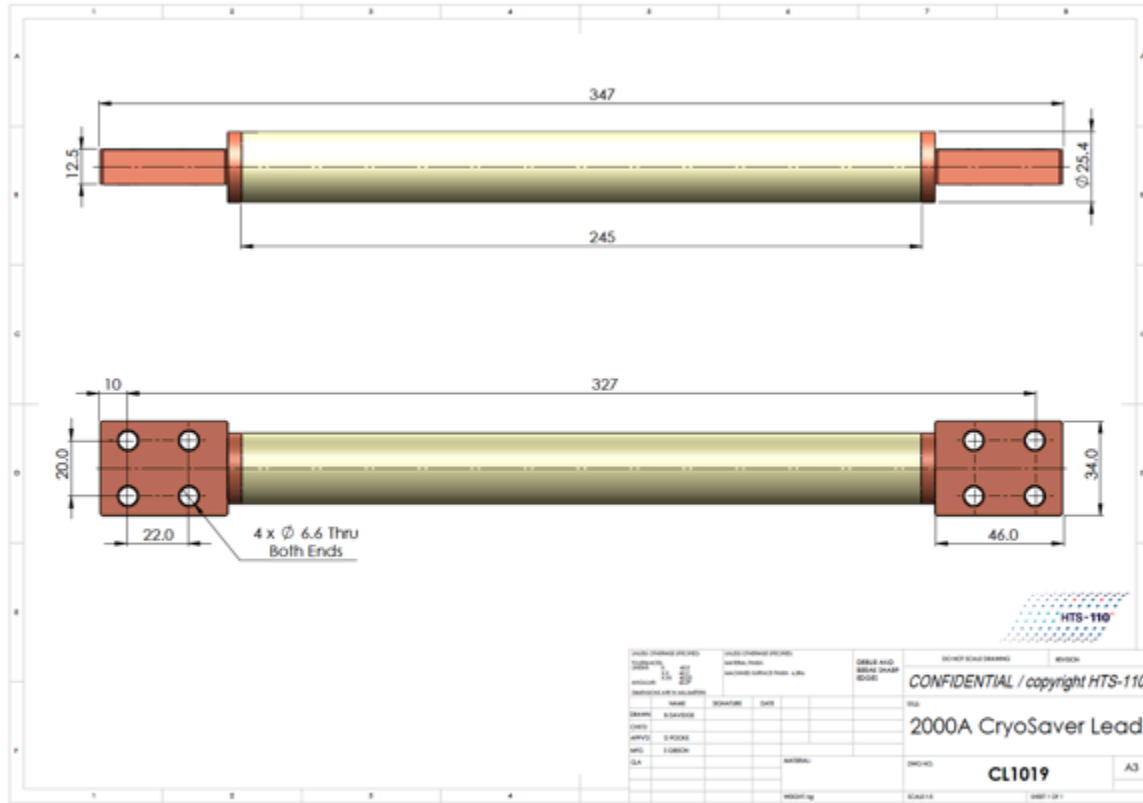


Fig. 6.2 Drawing of 2000 A CryoSaver current leads made by HTS-110 showing the dimensions.

7.0 Quench Analysis

7.1 Summary

A quench analysis has been completed on the Megatron Rev0 configuration. The general arrangement of the windings and iron was provided by Antaya¹, but it was modified per agreement in a meeting on 11/3/11 to add two more layers of conductor in the radial direction to keep the operating current below 4000 A. This avoids the need to bump the HTS current leads to another 2000 A increment. This layer count increase brought the winding arrangement to 20 layers radially by 16 turns per layer, or 320 turns per winding. The conductor is Luvata cable in channel², insulated with 0.2 mm of epoxy impregnated fiberglass all around. The Poisson model was modified to expand the winding area for the added layers, but the ampere turns were kept at 1.1982 MAT per coil. Energy reported from the revised Poisson model is 2.28 MJ (x2) = 4.56 MJ. With a current of 3744 A, the system inductance is 0.651 H.

A simple dump circuit has been modeled, comprised of a series connection of the two coil windings inside the cold mass, together with an external dump resistor ($R_d = 0.04 \Omega$) and a dump switch to disconnect the power supply following quench detection. A quench

¹ Timothy Antaya email, "Re: Poisson Model for Megatron", 11/02/11

² Hem Kanithi, Superconductor strand for HISCC (Megatron), Q 4826-Rev 1, 07/20/11

detection voltage threshold of 0.5 V together with a 0.5 s time delay was assumed. Once the normal zone voltage reaches 0.5 V and remains above that value for 0.5 s, the power supply is disconnected and the current decays through the dump resistor.

Four quench scenarios were evaluated: two with quench initiated from the point in the winding where $B=B_{\max}$, with $R_d = 0.04 \, \Omega$ and $R_d = 0 \, \Omega$, two with quench initiated from the point in the winding where $B=B_{\min}$ with $R_d = 0.04 \, \Omega$ and $R_d = 0 \, \Omega$. The analysis confirms a simple $\int J_{Cu}^2 dt$ estimate that the winding is well protected with the dump resistor. The analysis shows that the winding may be reasonably well self-protected. For the cases with a dump resistor, a normal zone initiating from the B_{\max} location produced the higher hot spot temperature of 76 K, whereas only 62.3 K was reached for the B_{\min} case. Maximum voltage across the coil terminals is 150 V at the start of the dump. The results show a very conservative quench performance. For the self-protection cases the corresponding maximum hot spot temperatures were 139 K (B_{\max}) and 111 K (B_{\min}).

7.2 Details

Parameters relative to the quench analysis are summarized in Table 1. Note that there are two coils which are fully symmetric about the z axis and only parameters for the coil in +z are given, although stored energy and inductance are for the system. Parameters are based on the nominal dimensions of the Luvata conductor, which is surrounded by 0.2 mm of turn insulation.

Table 7.1 Winding Parameters

Parameter	Units	Value
r_{inner}	m	0.57
r_{outer}	m	0.67532
z_{lower}	m	0.05
z_{upper}	m	0.20328
nlayers		20
n turns/layer		16
Nturns		320
NI	MAT	1.1982
Icoil	A	3744
Stored energy (Poisson)	MJ	4.56
System inductance	H	0.65

$J_c(B, T)$ fits to the Luvata provided data are per Bottura³, as calculated by Radovinsky⁴ with the aid of Mathematica.

The quench model used bulk thermal conductivity properties in the transverse direction derived from an ANSYS model done by Miller⁵. These were shown to be reasonably close to values obtained from simple electrical circuit analogy based models. Thermal

³ L. Bottura, "A Practical Fit for the Critical Surface of NbTi", IEEE Transactions on Applied Superconductivity, Vol. 10, No. 1, March 2000

⁴ Alexi Radovinsky, LUVATA Bottura Fit.nb, 11/2/11

⁵ Craig Miller, email "Compatible MS Versions", 11/14/11

conduction in the θ direction is calculated directly in the quench solver to account for variation with magnetic induction, B , in every element, which varies with time. The magnetic induction is assumed to be proportional to the current in each element, which is to imply that the non-linearities caused by the iron are not accounted for in the calculation of B on an element by element basis. The specific heat of each element is also calculated dynamically within the solver to account for the variation of the specific heat of NbTi with temperatures that are above or below the current sharing temperature.

A relatively new addition to the quench program combines the local resistive and inductive voltages on an element by element basis to give the net voltage along the element. Inductive voltages are calculated using a mutual inductance module extracted from Solderesign. By sorting the coil elements in winding order and summing the element voltages, the voltage along the entire winding can be calculated at any point in time. The end-to-end voltage across the windings should match the voltage across the dump resistor to satisfy Kirkhoff's voltage law, and this serves as a good check of the code calculations.

Plots of the results are provided in the figures below. The first four plots are the transient response curves for the coil current (Fig. 7.1), hot spot temperature (Fig. 7.2), normal zone resistance (Fig. 7.3) and the evolution of the normal region of the winding (Fig. 7.4). Note that only half of all windings are normal since the symmetric coil does not quench. Figure 7.5 shows the coil voltage along the winding at 1.5 seconds into the transient for quench from B_{max} with $R_d=0.04 \Omega$. For the megatron this voltage is rather linear with turn number, although this is not always the case for other magnet systems. The fact that the summed inductive and resistive voltages within the almost 20,000 elements matches the $I_{coil} \cdot R_d$ voltage drop is a good check of the results. The voltages, of course, are entirely benign.

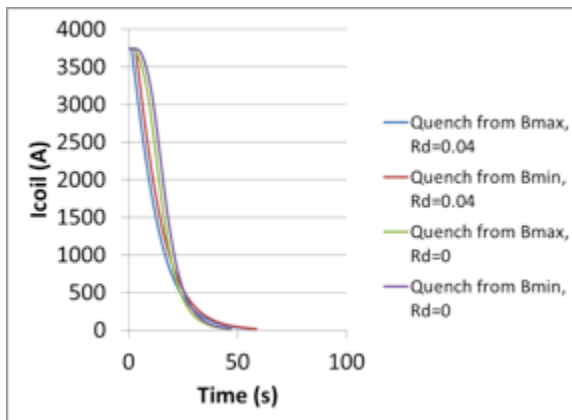


Fig. 7.1 Coil current

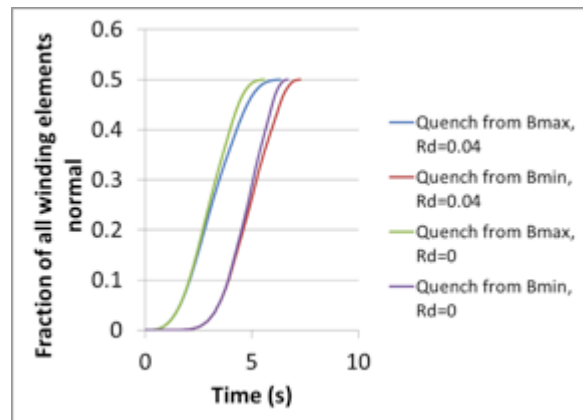


Fig. 7.2 Fraction of winding normal

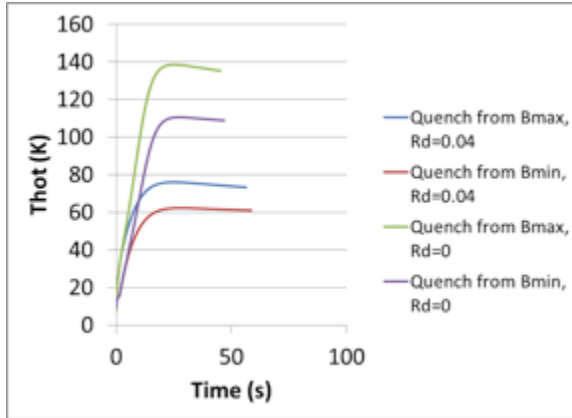


Fig. 7.3 Coil hot spot temperature

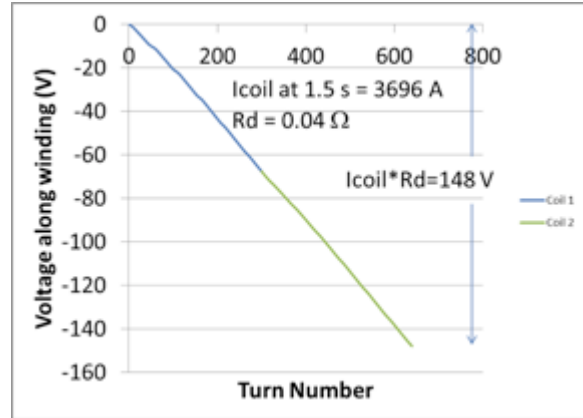


Fig. 7.4 Voltage along the windings

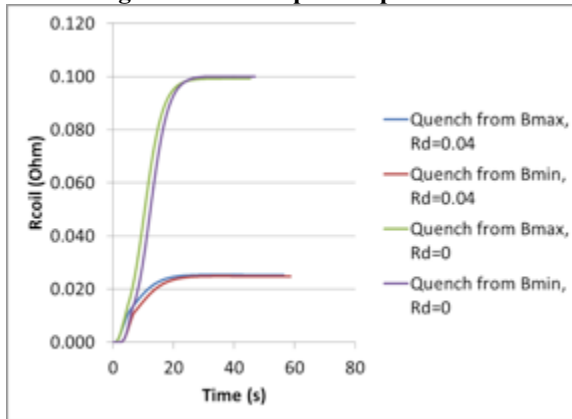


Fig. 7.5 Coil normal resistance

Figures 7.6-7.8 are the 3d temperature distribution plots at various time points for the case of quenching from Bmax with $R_d=0.04$ Ω, and Figs. 7.9 and 7.10 are for quenching from Bmin with $R_d=0.04$ Ω. Figs. 7.6, 7.7 and 7.9 are relatively early in their respective transients and Figs. 7.8 and 7.10 are at the time of the hot spot temperature maximum for each case. A full set of 3d plots, which are only partially presented here, help with the visualization of how the normal zone spreads in time.

HISCC (Megatron) Final Report

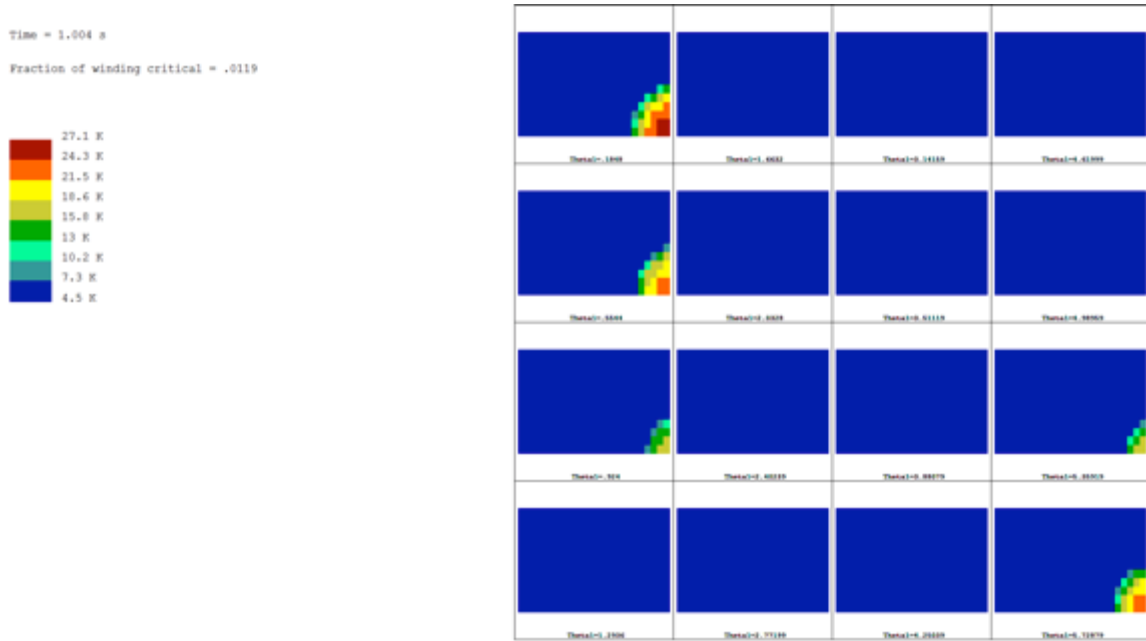


Fig. 7.6 Fig. 7.6 Quench from Bmax, Rd=0.04 Ω , 1 s. Three dimensional temperature distribution at 1 s. Each small window represents a view of the r (vertical) – z (horizontal) plane at one of 16 evenly distributed azimuthal (θ direction) slices around the coil.

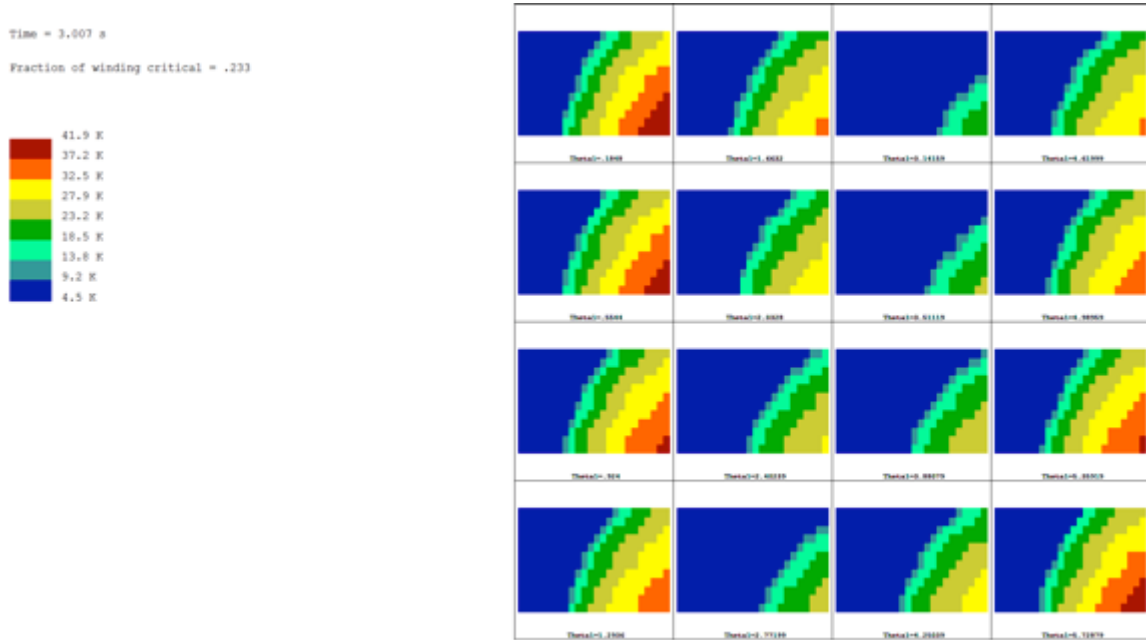


Fig. 7.7 Quench from Bmax, Rd=0.04 Ω , 3 s. Three dimensional temperature distribution. Each small window represents a view of the r (vertical) – z (horizontal) plane at one of 16 evenly distributed azimuthal (θ direction) slices around the coil.

HISCC (Megatron) Final Report

Time = 25.007 s
Fraction of winding critical = .5

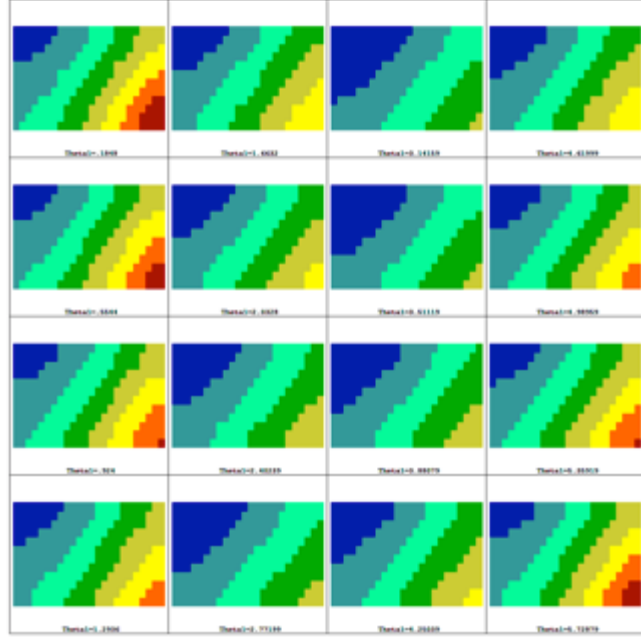


Fig. 7.8 Quench from Bmax, $R_d=0.04 \Omega$, 25 s. Three dimensional temperature distribution. Each small window represents a view of the r (vertical) – z (horizontal) plane at one of 16 evenly distributed azimuthal (θ direction) slices around the coil.

Time = 2.502 s
Fraction of winding critical = .0042

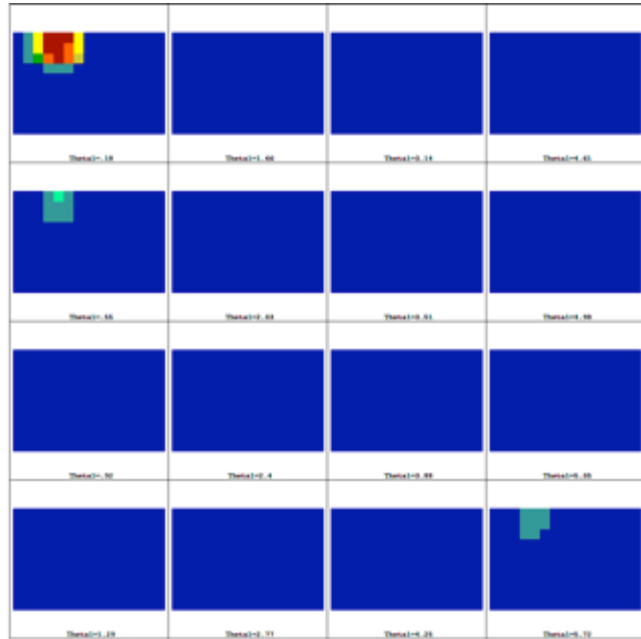


Fig. 7.9 Quench from Bmin, $R_d=0.04 \Omega$, 2.5 s. Three dimensional temperature distribution. Each small window represents a view of the r (vertical) – z (horizontal) plane at one of 16 evenly distributed azimuthal (θ direction) slices around the coil.

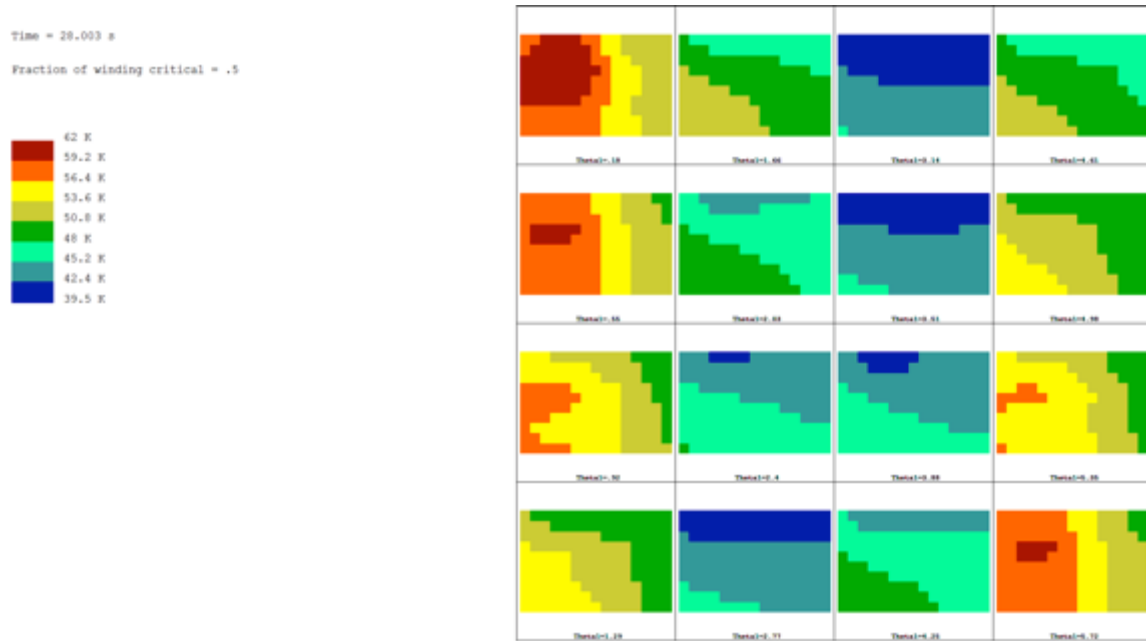


Fig. 7.10 Quench from Bmin, Rd=0.04 Ω , 28 s. Three dimensional temperature distribution. Each small window represents a view of the r (vertical) – z (horizontal) plane at one of 16 evenly distributed azimuthal (θ direction) slices around the coil.

8.0 Magnet Nuclear Heating

8.1 The radiation challenges of Megatron

Megatron is an ultracompact, superconducting, isochronous cyclotron designed to produce a 250 MeV, 1mA proton beam with an extremely low extraction loss rate. Several novel features of the Megatron design have significant implications for the analysis and mitigation of deleterious effects induced by radiation.

- Ultra-compact geometry results in
 - High particle fluxes/fluences through structural components
 - Constraints on the design and effectiveness of a radiation shield
- High beam energy of 250 MeV opens many nuclear reaction channels
- High beam current 1 μ A - 1 mA ensures high nuclear reaction rates.

The accelerated beam of protons represents two significant sources of radiation that must be taken into account for the engineering of Megatron:

The proton beam itself (“primaries”)

- A 250 MeV, 1 mA proton beam carries 250 kW of power

Proton-induced nuclear reaction products (“secondaries”)

- High energy protons incident upon dense materials induce high-energy particle cascades or “spallation”
 - High energy protons are produced via (p,p’), (n,p) reactions
 - High energy neutrons are produced via (n,n’), (p,n) reactions

- High energy gamma are produced by inelastic scattering and particle capture reactions

A graphic description of these reactions are shown in Fig. 8.1

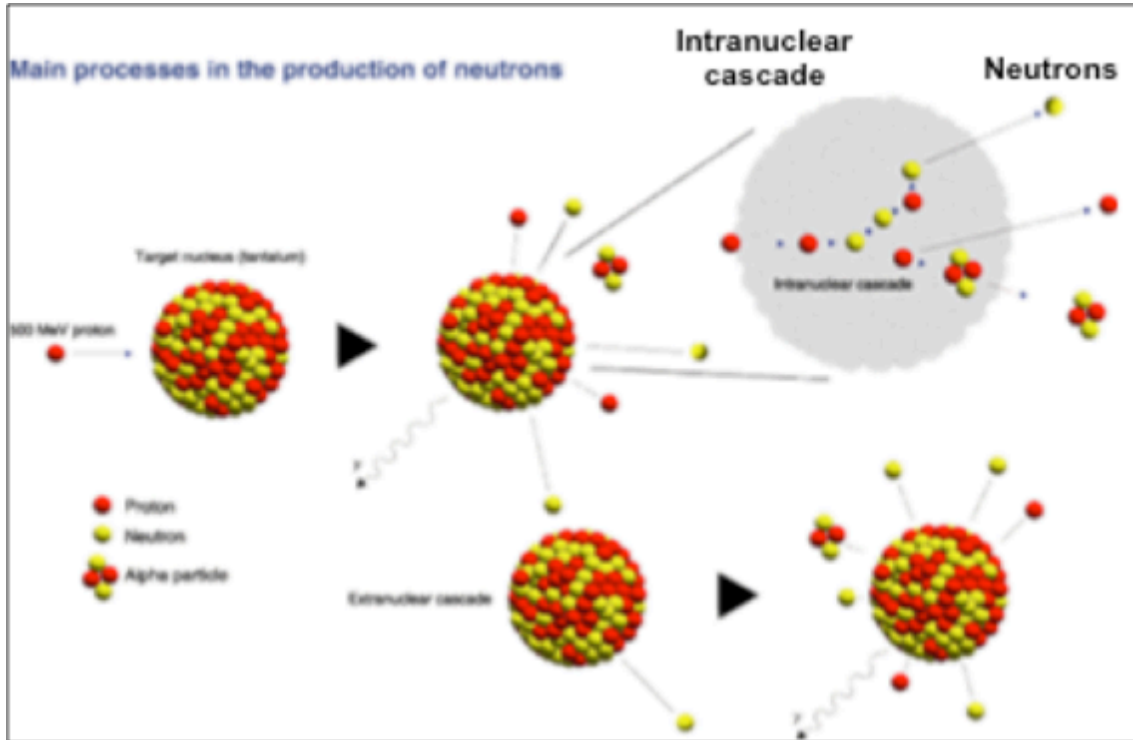


Fig. 8.1 Main processes in the production of neutrons in the Megatron.

When the control of the primary proton beam is lost or misguided, primary protons will impact bulk material in Megatron. Primary protons deposit energy and induce secondary particle production. Secondaries deposit energy and induce further particle production cycles. All particles that do not leak out of the system eventually deposit their kinetic energy into the bulk material as heat. This process is shown schematically in Fig. 8.2.

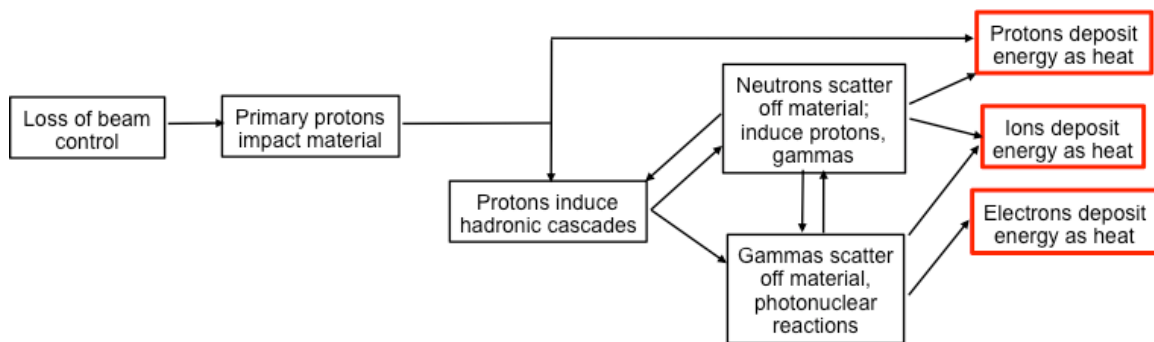


Fig. 8.2 Schematic of the nuclear radiation process that results in heating of the structures.

Nuclear heating of bulk structures in Megatron is most critical for the 4 K superconducting magnet coils and cold magnet supports for two reasons :

1. Preventing a quench of the superconducting magnets: sufficient heating of the coil will exceed the critical temperature and return the coil to normal conducting.
 - a. Joule heating of the magnet can lead to permanent and/or terminal damage.
2. Minimizing the required cryogenic system power: The removal of heat at 4 K by a cryogenic system is power intensive, which affects the cost and size of the required cryogenic system.

A comprehensive understanding of how the primary and secondary radiation contributes to nuclear heating of the cold masses, as well as mitigation strategies if nuclear heating is determined to be mission critical, are necessary for the engineering design and ultimate success of Megatron. Note: All results discussed heat refer to beam loss inside Megatron and subsequent radiation effects on Megatron components.

8.2 The MegatronG4 Simulation

Geant4[†] is a C++ toolkit for the Monte Carlo transport of particle through matter originally developed at CERN for high energy physics (HEP). Geant4 is:

1. A leading simulation package for particle, nuclear, space, and medical physics:
 - a. LHC's ATLAS and CMS detectors; proton beam radiotherapy; Fermi Gamma-Ray Space Telescope, Alcator C-Mod fusion tokamak
2. Increasingly used by the security community
 - a. SNM detection, X-ray scanners, accelerator and cyclotron development, advanced neutron detectors
3. Complete range of physics, complex geometry handling, robust data extraction.

Geant4 has several unique advantages for the Megatron simulation work. It is *extendable* by providing a platform for inclusion of beam dynamics, charged particle tracking in EM fields, synchrotron radiation analysis from beam tracking. It is *customizable*, offering complete freedom to include a user's C++ code to handle complex tasks such as data processing, data output, and engineering parameter scans.

MegatronG4 is a comprehensive Geant4 simulation for the analysis of radiation in the Megatron superconducting cyclotron. The simulation features, geometry and materials from Megatron engineering plans, superconducting coils overlaid with high-resolution 3D voxelizations for collection of radiation data, a parallel framework with OpenMPI for scalable processing of high statistics runs or large parameters scans, neutron detectors for assessing the feasibility of an ex-situ beam diagnostic, an internal beam target to simulate effects of lost beam striking metallic components and/or extraction apertures inboard of the cryostat that will allow us to characterize how material choice will affect the induced radiation field. A rendering of the MegatronG4 model is given in Fig. 8.3.

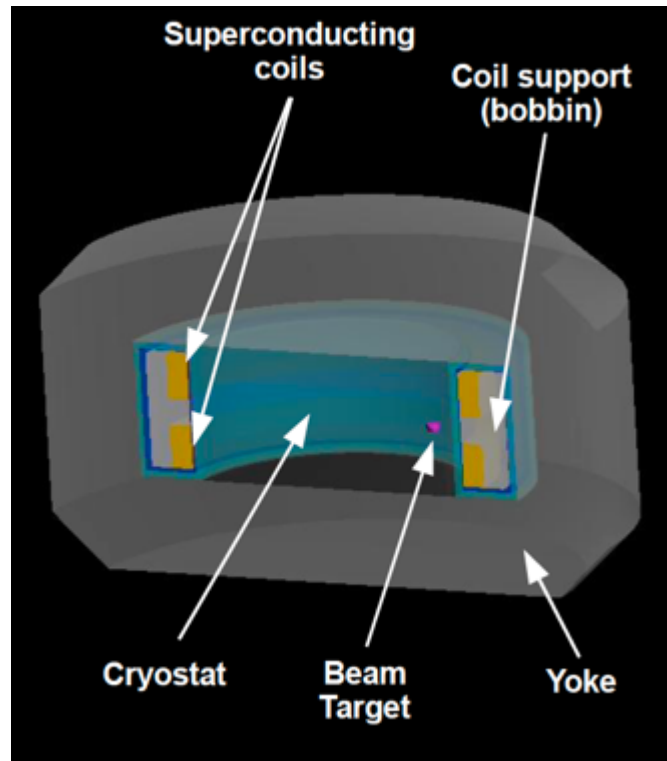


Fig. 8.3 Drawing of the Geant4 model of the Megatron.

A top-down view of the MegatronG4 geometry is shown in Fig. 8.4.

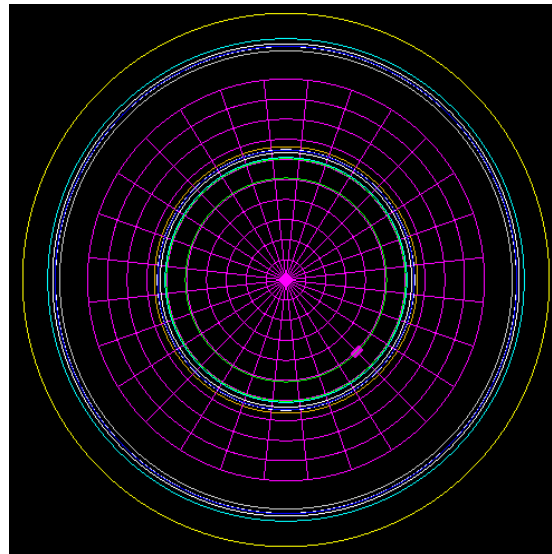


Fig. 8.4 3D voxelization of the MegatronG4 geometry. A low-resolution 3D voxelization of the SC coils (magenta) is imaged over the geometry. High resolution 3D voxelization are used for simulation with $r=40$, $\phi=180$, $z=5$ divisions for a total of 36000 voxels.

Simulated particle reactions are shown in Fig. 8.5.

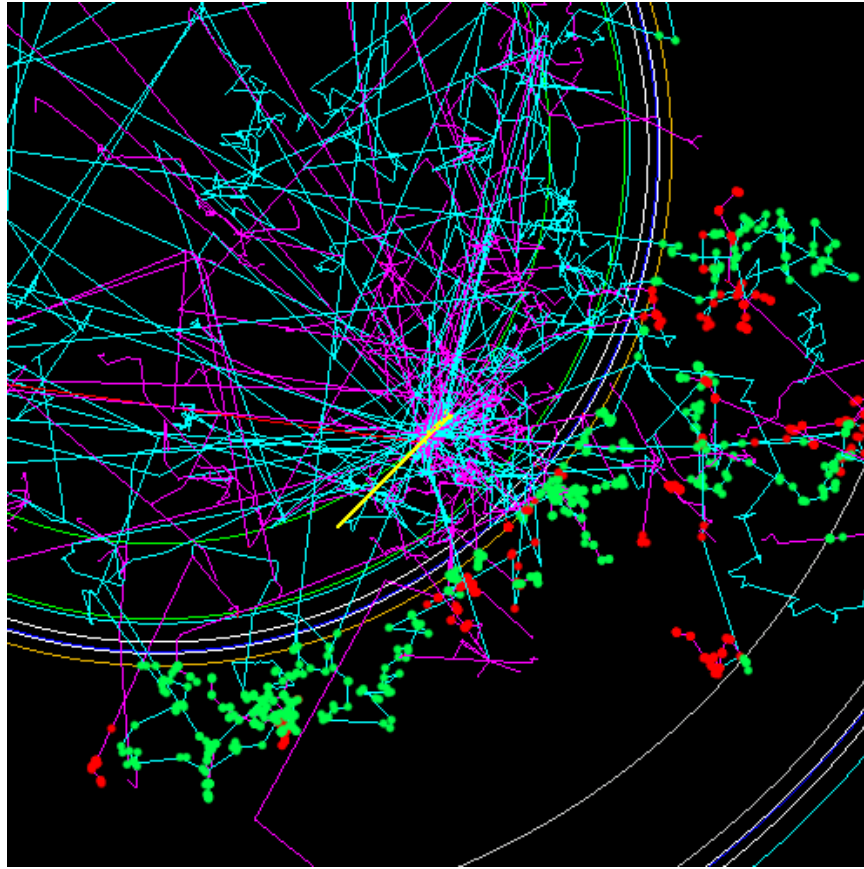


Fig. 8.5 Top down view of 250 MeV proton beam (yellow) incident into upon a copper target (obscured). Spallation neutrons (cyan) and induced gammas (magenta) scatter through the geometry and deposited energy into the SC coils (red) and SC coil bobbin (green).

8.3 Verification and validation of MegatronG4

Validation and verification of computational models is a critical step to increase our confidence in the results, especially when the model is used to analyze unprecedented experimental configurations and to extrapolate to regimes where experimental validation cannot be performed.

- **Validation:** *“The process of determining the degree to which a conceptual model is an accurate representation of the real world from the perspective of the intended uses”*

Due to the Megatron’s novelty, few comprehensive experimental results exist that can be used to validate radiation studies for ultra-compact superconducting cyclotrons, however, there is an opportunity to validate against data on proton spallation at 250 MeV.

- **Verification:** *“Substantiation that a computerized model and its solution represent a conceptual model within specified limits of accuracy”*

One method is a head-to-head comparison between computational codes. We use this opportunity to compare Geant4 and MCNPX for radiation studies of cyclotrons.

There are a few precedents for radiation analysis of compact superconducting cyclotrons. Work by F. Stichelbaut at IBA for the C400 (Diam = 6 m, Ht = 3 m) and the S2C2 (Diam = 2.6 m, Ht = 1.6 m) are excellent examples. Heating of the superconducting coil in the C400 from ^{12}C ions impacting the extraction aperture were done with a PHITS simulation (Fig. 8.6.).

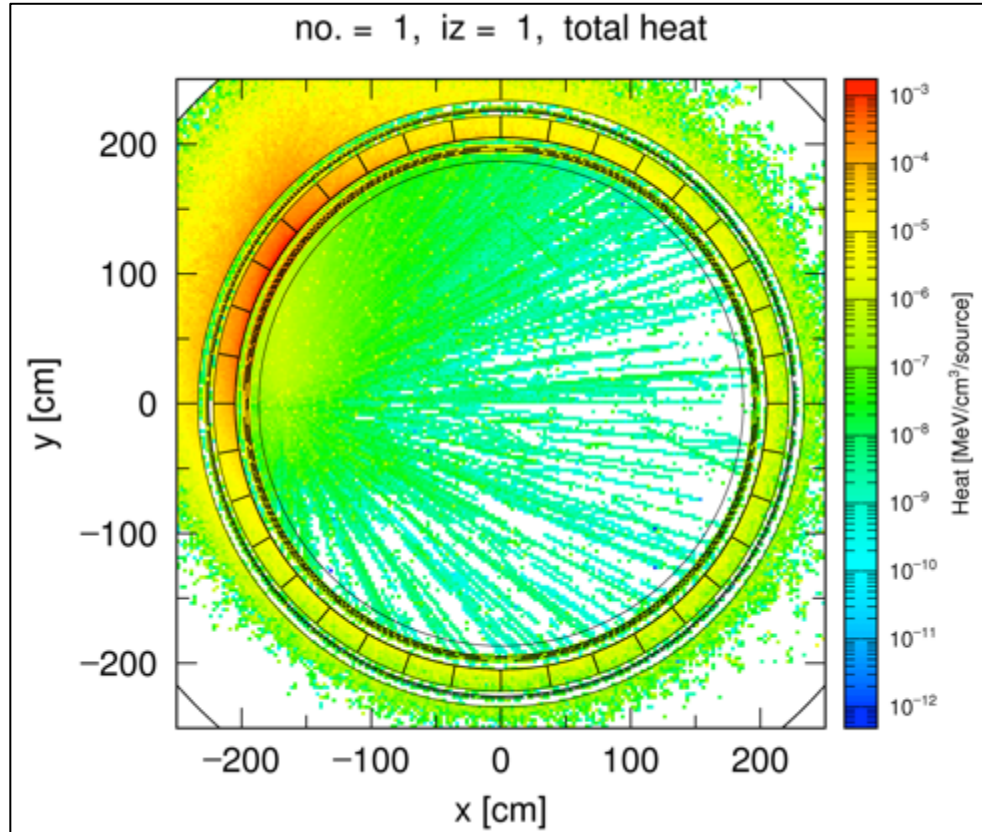


Fig. 8.6 Peak heating of a single superconducting coil from a $0.25 \times 10^{-6} \text{ W/cm}^3/\text{nA}$ beam. Top-down view of heating tally mesh in a C400 PHITS simulation.

The heat load in the cold mass in S2C2 is shown in Fig. 8.7 for a 250 MeV proton beam impacting the extraction aperture using an MCNPX simulation.

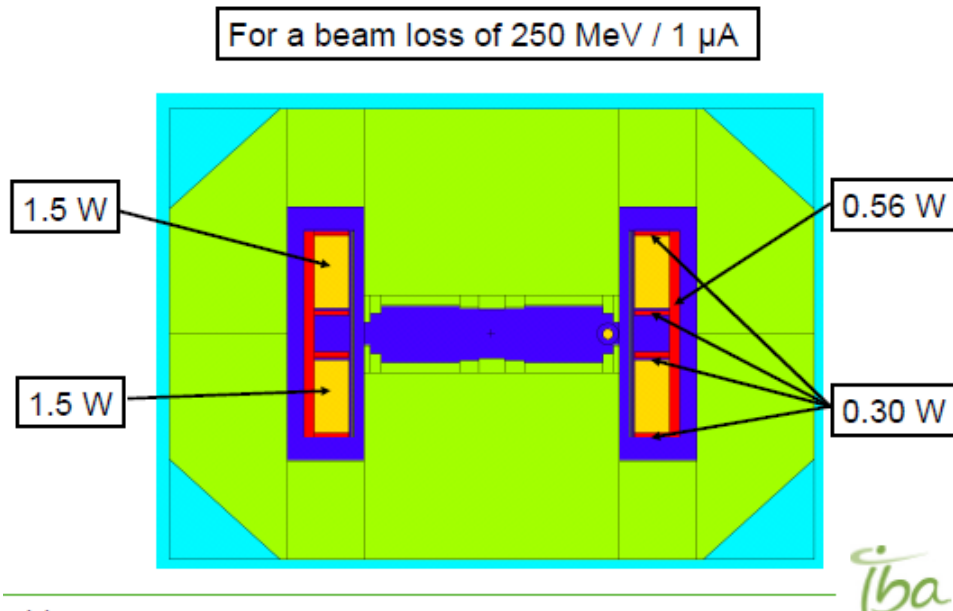


Fig. 8.7 MCNPX simulation of heating in the cold mass of the S2C2. Heating of single SC coil: 1.5 W/ μ A beam, peak heating of SC coil: 0.35×10^{-3} W/cm³/ μ A, total heating of cold masses: 3.86 W/ μ A.

We validated the spallation physics models in MegatronG4 against experimental spallation results. MegatronG4 was configured such that a 250 MeV proton beam was fully stopped in 5x5x10 cm lead target. The total number of spallation neutrons was scored and results were normalized to (spallation neutrons) / (primary proton) such that they could be compared to experimental results.

The experimental results we used for comparison are reported in Y.V. Ryabov, G.K. Matushko, and V.N. Slastnikov, “Experimentally measured neutron yield from 250 MeV protons on lead,” (Z. Phys. A, 311 (4) 363-365). Below are the results of the best validation effort using Geant4's Binary Ion Cascade for spallation physics:

- MegatronG4: (2.85 +/- 0.01) neutrons / proton
- Experiment: (2.56 +/- 0.27) neutrons / proton

As another leading Monte Carlo particle transport-in-matter simulation that has been used extensively for nuclear heating analysis, MCNPX represents an excellent candidate for benchmarking several features of the MegatronG4 simulation, including physics models for spallation, particle transport, energy deposition processes, and data collection using 3D voxelization of superconducting coils. MegatronG4 uses a simplified benchmarking geometry for direct comparison to MCNPX. An identical, simplified cyclotron geometry and identical materials were created in MegatronG4 and MCNPX to ensure that valid comparisons could be made. We used a nickel beam target for proton spallation and an isotropic point source of particles for heating. The model is shown in Fig. 8.8.

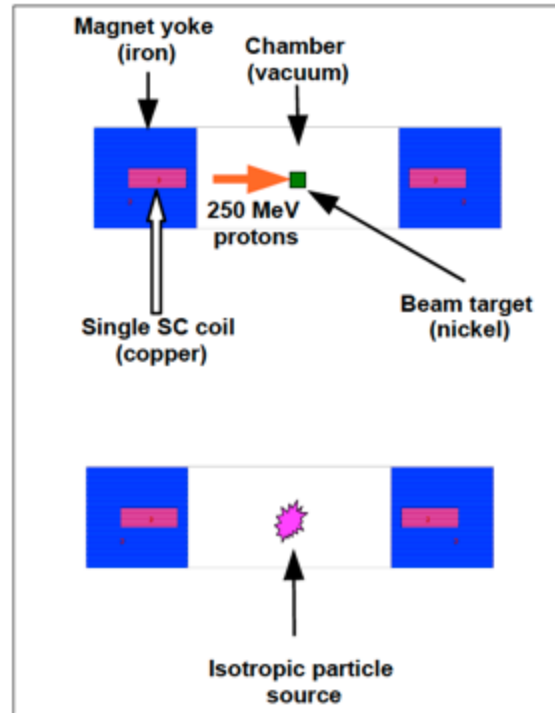


Fig. 8.8 A cross-section of the benchmarking geometry and two simulation setups in MCNPX.

Spallation particle productions for 5×10^4 protons incident at 250 MeV upon a nickel target for in MegatronG4 and MCNPX were tallied and compared. Geant4's Binary Ion Cascade and QBBC models for spallation production agreed reasonably well with MCNPX's Bertini, INCL4, and ISABEL models as shown in Fig. 8.9.

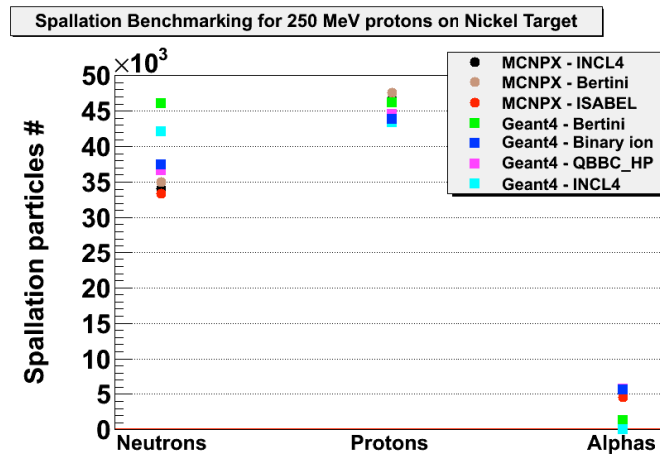


Fig. 8.9 Spallation benchmarking for 250 MeV protons on a nickel target.

Based on these results we proceeded with simulating the nuclear radiation and heating in the superconducting coil in MegatronG4 by benchmarking against MCNPX. We modeled an isotropic, monoenergetic neutron source of arbitrary strength placed in the center of the benchmarking geometry. Energy deposition (MeV) in the single SC coil at neutron energies between 0 and 150 MeV were tallied and converted into power

deposition (W). Two versions of the QGSP_BIC Geant4 physics list were compared to standard MCNPX physics:

- QGSP_BIC: parameterized models only
- QGSP_BIC_HP uses ENDF/B derived data for neutron transport below 20 MeV; parameterized models above 20 MeV
- MCNPX uses derived data for neutron transport below 20 MeV; parameterized models above 20 MeV

Results from these benchmark computations are shown in Fig. 8.10a and b.

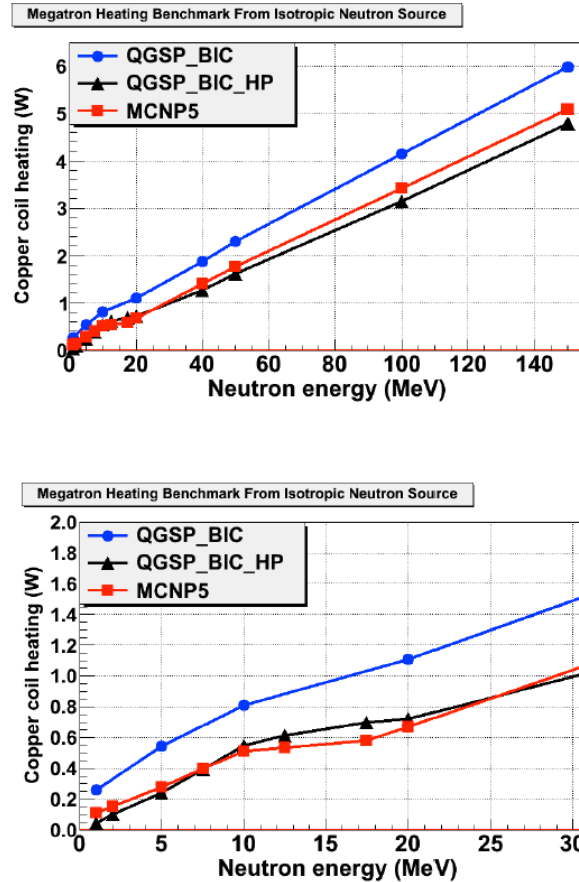


Fig. 8.10 a) (Top) shows heating in the coil copper in watts as a function of neutron energy in the range 0 to 150 MeV, b) (Bottom), expanded scale heating in the coil versus neutron energy in the range 0 to 20 MeV.

The agreement for neutron power deposition at energies below 30 MeV is excellent. The agreement for neutron power deposition at energies above 30 MeV is good. For example, at 150 MeV, $(P_{\text{geant4}} / P_{\text{MCNPX}}) = 0.94$.

Using the same models, we simulated energy deposition in a single coil from protons at energies between 0 and 250 MeV. These were tallied and converted into power deposition in W/ μA as shown in Fig. 8.11. Agreement for total power deposition is

excellent for proton energies below 150 MeV, however, there is a slight divergence in agreement at energies above 150 MeV. At 250 MeV ($P_{\text{geant4}} / P_{\text{MCNPX}} = 0.91$).

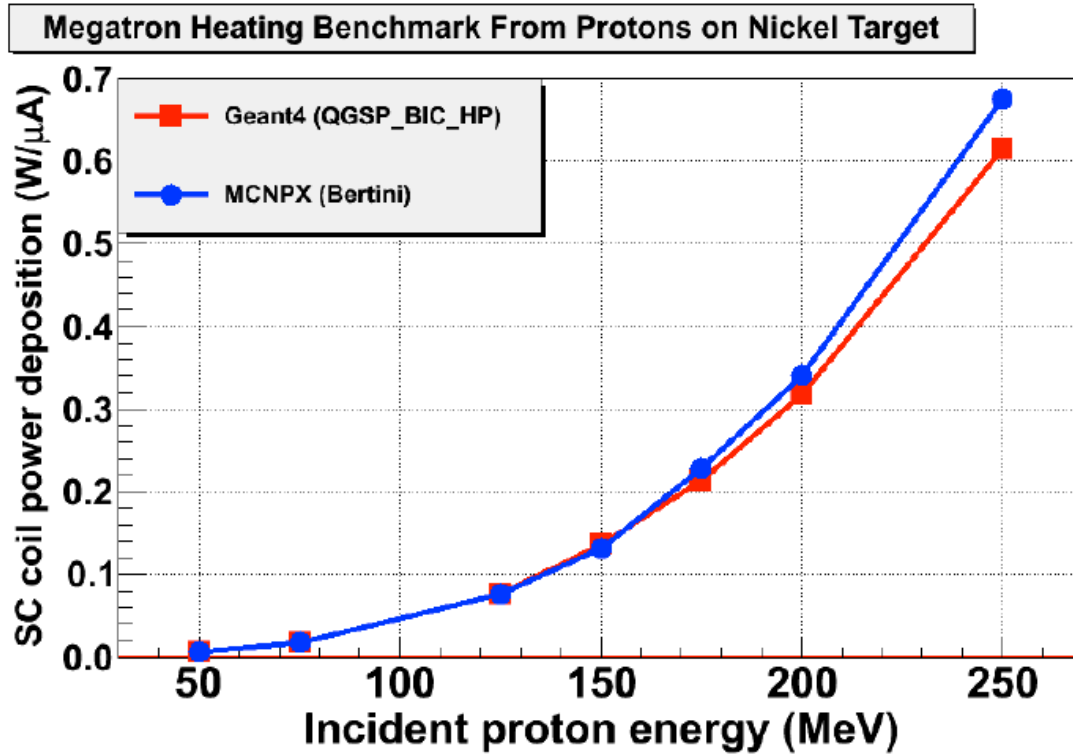


Fig. 8.11 Benchmark of heating in Megatron from protons on a nickel target, comparison between Geant4 and MCNPX.

8.4 Results from the MegatronG4 Simulation

Direct impact of the proton beam onto the cryostat results in extreme peak and total heating of the cold mass. If radial control of the beam is lost, protons will pass through the cryostat and be fully stopped by the SC coil bobbin, with the following consequences: extremely high energy deposition from primary protons in the coil bobbin, secondary radiation to the superconducting coil will be highly peaked in the region closest to the beam strike location, yielding a highly localized heating in the azimuth and vertical directions within the coil.

The location of the peak heating from the protons in the azimuthal direction can be seen in Fig. 8.12a, while the radial power peaking is shown in Fig. 8.12b.

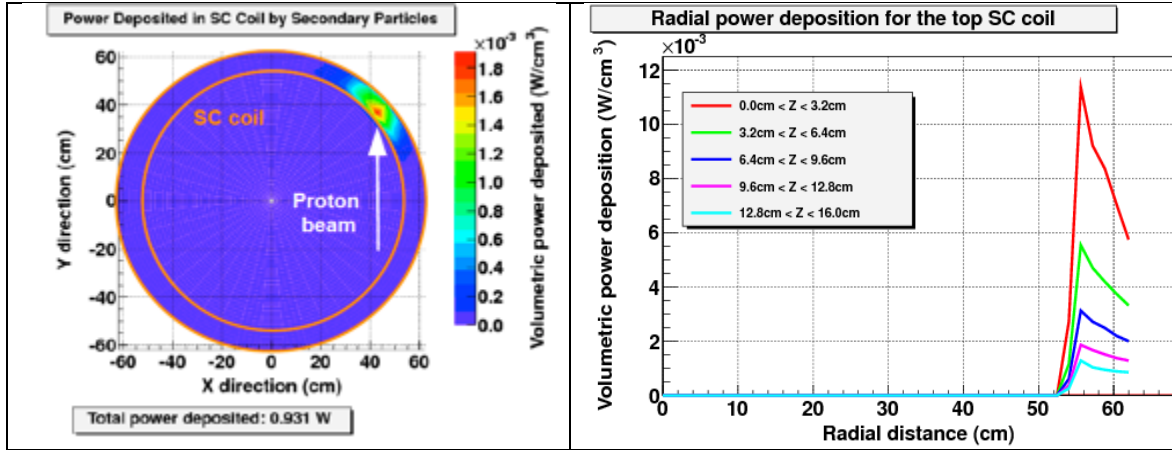


Fig. 8.12 a) Peak heating in the azimuthal direction from protons deposited in the superconducting magnet, b) peak heating in the radial direction, at different axial heights, from protons deposited in the superconducting magnet.

These results can be summarized:

- MegatronG4 Simulation Results (per μ A beam)
 - Heating of a single SC coil: **0.931 W**
 - Peak volumetric heating of single SC coil: **1.58×10^{-3} W/cm³**
 - Heating of cold mass (2 SC coils, 1 bobbin): **125.21 W**

Clearly, the magnet system cannot safely absorb 125 W of heating at 4 K, if the full 1 μ A beam were to impinge the cold mass. This demonstrates that the total maximum radiation to the coil must be limited. If control of the beam is lost, the current should be immediately terminated in order to avoid damage to the magnet.

The use of a dedicated in-situ beam target should reduce the nuclear heating issues of the cold mass. This would eliminate the extreme total heating of the cold mass, reduce the peak heating of cold mass including the superconducting coils, and distribute the heat deposition over a larger volume. The material choice for the beam target, however, is critical. The material should minimize secondary particle production, minimize the induced radioactivity of the target material, possess high proton stopping power to reduce the target size, and be relatively inexpensive and easy to machine/fabricate.

Mitigation with a beam target is a trade-off between target length, particle production, and radioactivity. We analyzed target length, particle production, and radioactivity for 7 solid materials used for intermediate energy proton beam dumps. The materials we considered are shown in Table 8.1.

Table 8.1 Target materials considered for an intermediate proton beam dump.

Target Material	Range, 250 MeV protons (cm) [†]
Graphite	18.8
Copper	6.3
Tungsten	3.8
Aluminum	17.9
Nickel	6.0
Tantalum	4.4
Iron	6.9

Figure. 8.13 shows the total power deposition for full stopping of the beam in the target for 7 different target materials.

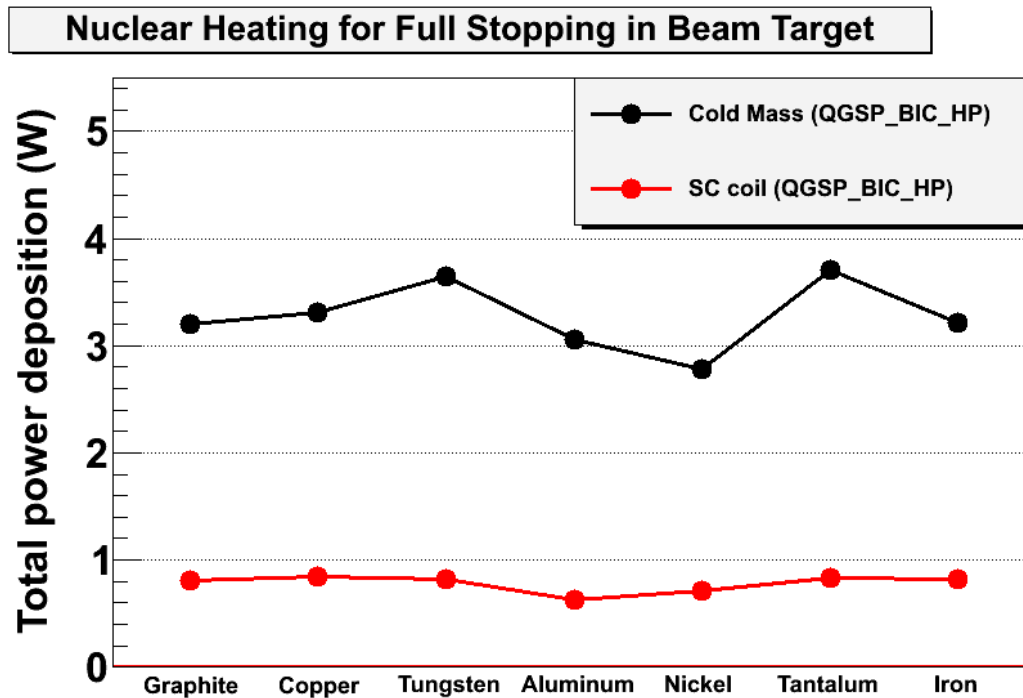


Fig. 8.11 Nuclear heating for full stopping of a 1 μ A proton beam in the beam target for 7 different target materials.

This code also allowed us to compute activation and cooling times for several target materials (Fig. 8.14).

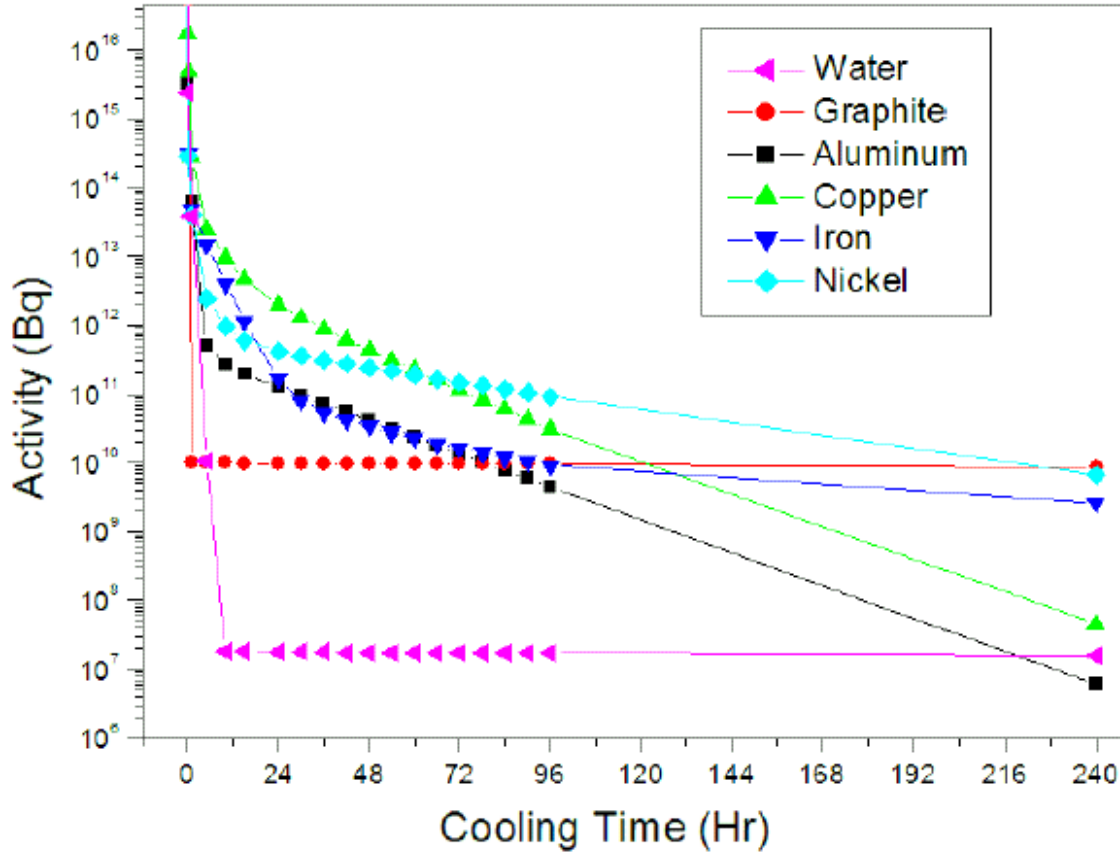


Fig. 8.12 Activated beam dump cooling times for 1.6 mA, 150 MeV proton beam.

Nickel is the superior choice to reduce nuclear heating in the cold masses with short target lengths, however, radioactivity may be an issue. Copper is the second best choice to reduce nuclear heating in the cold masses (~0.5 W more than Ni) but it is more favorable from an activation standpoint.

A 5x5x70 mm nickel beam target was used to absorb the full beam power at a radius of 42cm, preventing the proton beam from reaching the cold mass. Total heating of the cold mass was thus significantly reduced, especially in the coil bobbin. Peak heating was also reduced significantly and the total heating was distributed more broadly in the azimuthal and vertical directions. This can be seen in Figs. 8.15 a and b.

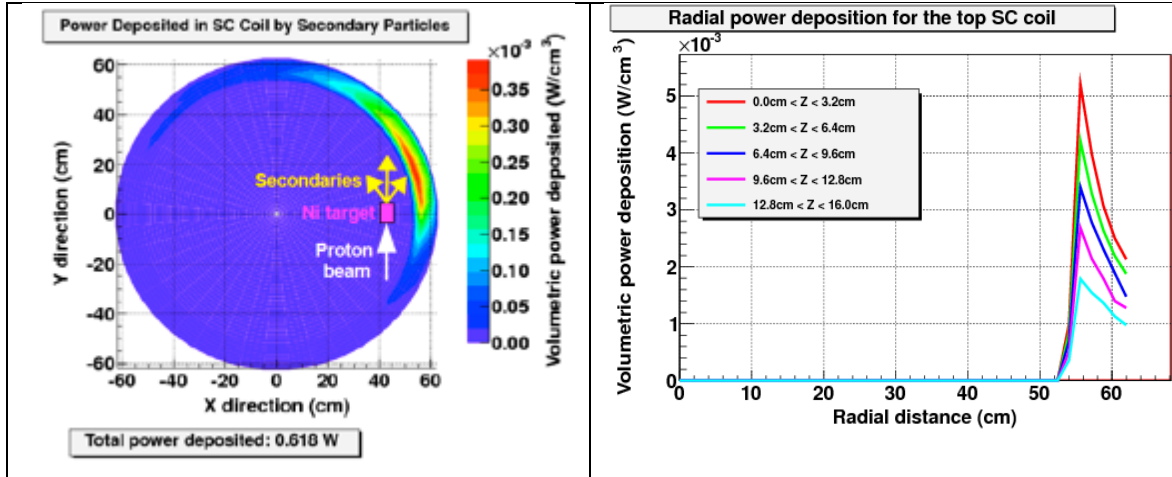


Fig. 8.13 a) Peak heating in the azimuthal direction from protons deposited in the superconducting magnet, b) peak heating in the radial direction, at different axial heights, from protons deposited in the superconducting magnet. Results are based on using a 5x5x70 mm nickel beam target.

The results can be summarized:

- MegatronG4 Simulation Results (per μA beam)
 - Heating of a single SC coil: **0.61 W**
 - Peak volumetric heating of single SC coil: **$0.15 \times 10^{-3} \text{ W/cm}^3$**
 - Heating of cold mass (2 SC coils, 1 bobbin): **2.51 W**

Here the cold mass losses are reduced to a tolerable 2.5 W from the unstopped beam loss of 125 W.

The 1 mA, 250 MeV proton beam proposed for Megatron creates significant heating challenges for the cold masses compared to other compact superconducting cyclotrons. This can be seen in Table 8.2 where full beam power into the cold mass will be 1000x greater for Megatron than in the other two cyclotrons. Thus, a fast beam abort option will be utilized in Megatron to prevent full beam power from reaching the cold masses.

Table 8.2 Comparison of beam loss in the cold mass for three different cyclotrons.

	Outer Diameter (m)	Beam energy (MeV)	Max. Beam current	SC coil heating (W / μA)	SC coil peak heating (W/cm ³ / μA)	Cold mass heating (W / μA)
C400	6.0	400 (¹² C)	~nA	-	0.25×10^{-3}	-
S2C2	2.6	250 (proton)	~ μA	1.5	0.35×10^{-3}	3.86
Megatron (with Ni target)	2.2	250 (proton)	~mA	0.61*	0.15×10^{-3} *	2.51*

8.5 Feasibility assessment of an ex-situ beam diagnostic

It is physically impossible to directly measure the current of a 1mA, 250 MeV proton beam because it would require absorbing 250 kW of power deposited directly on Faraday Cup. An alternative beam energy and current diagnostic must be found.

MegatronG4 has been used to assess the feasibility of using an external neutron detector to indirectly measure beam current. Neutron production is a function of beam energy and beam current. The detector count rate should be a unique measure of energy and current. MegatronG4 functions as a “synthetic diagnostic” for beam measurements. Synthetic detector count rates could be validated against experimental data from Megatron beam measurements at low current. The synthetic detector counts rates are then used to infer beam energy and current at high current.

Results of external beam diagnostic feasibility

In the MegatronG4 simulation, a 2.54 Φ x 50 cm cylindrical Helium-3 proportional counter was placed 1.5 m from the central axis of Megatron (external to the iron yoke). Neutron counting rates were calculated for primary protons impacting a Ni target at incident energies between 50 and 250 MeV. The model is shown in Fig. 8.16.

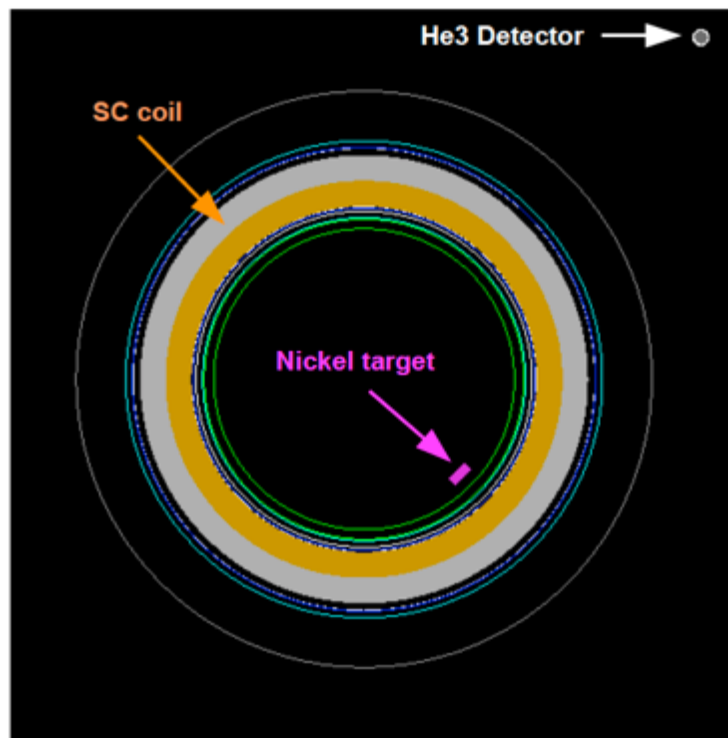


Fig. 8.14 Top-down view of Megatron with an external Helium-3 detector

Since neutron counting rates are single-valued functions of beam energy and current, this provides for unique determination of beam parameters using an external neutron detector. The results are shown in Fig. 8.17.

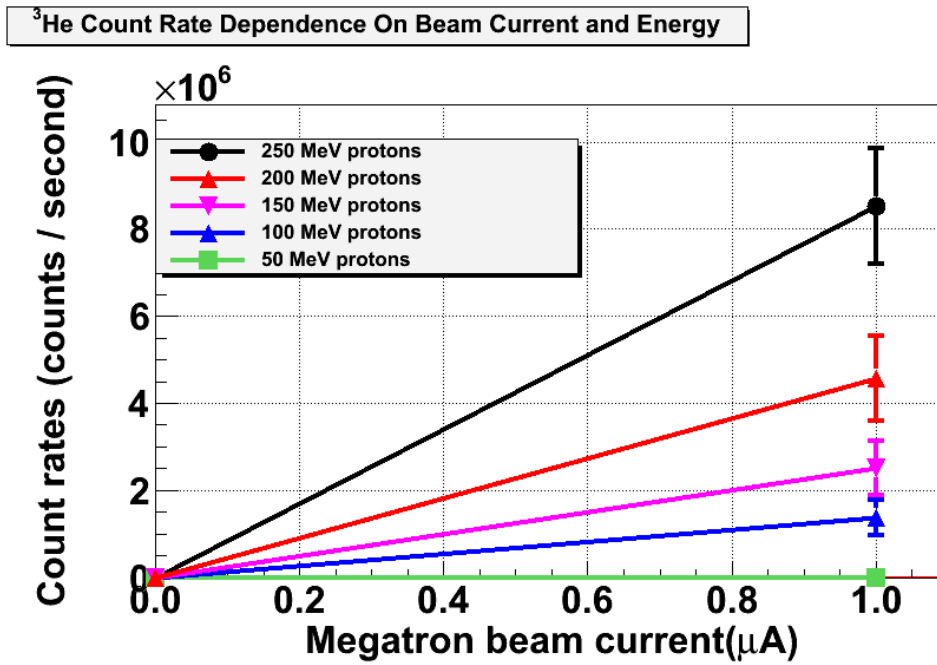


Fig. 8.15 ³He count rates as a function of Megatron beam currents at different energies.

9.0 Temperature Distribution in Winding Pack Due to Radiation Heating

The temperatures in the winding pack due to heating from high-energy particles was calculated based on the analysis from Section 8.0. The model uses a smeared winding pack, with orthotropic thermal conductivity (thermal conductivity that varies in different directions). The heat source from high energy particles has been adjusted from the radiation heating results by Zach Hartwig.

9.1 Thermal model

The main dimensions of the winding pack are shown in Table 9.1. The geometry used is shown in Fig. 9.1.

Table 9.1 Winding pack parameters used in the thermal calculations

r_min	0.54
r_max	0.62
height	0.16

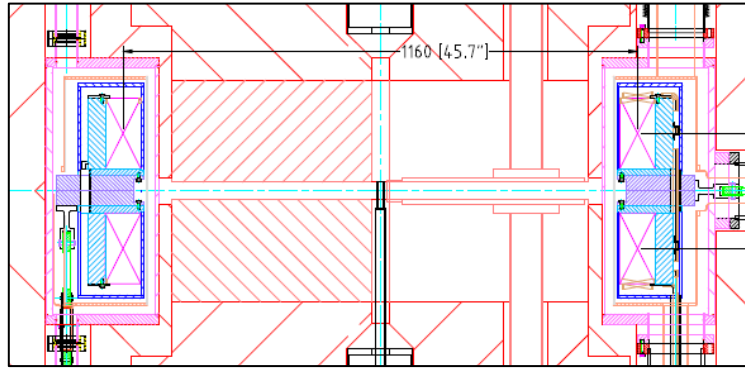


Fig. 9.1 Cyclotron geometry used for analysis.

The model assumes a smeared winding pack. The winding pack consists of an array of conductors, made from copper, superconductor, solder and insulation. Figure 9.2 shows the basic cable, including the insulation. The geometry in Fig. 9.2 is used to calculate the smeared properties of the winding pack.

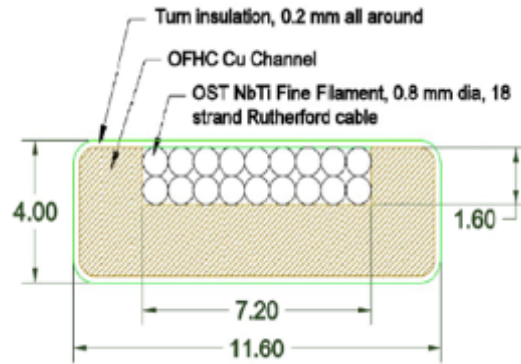


Fig. 9.2 Cable configuration used in the analysis

The thermal properties of the insulation, copper and steel are presented in Figs. 9.3-9.5. The units are in MKS (heat capacity in J/kg K, thermal conductivity in W/ m K). Because of the small temperature excursion in the coils, the assumed properties are $k_{Cu} = 621$ W/ m K, $k_{G10} = 0.064$ W/ m K, and $k_{SS} = 0.23$ W/ m K, independent of temperature.

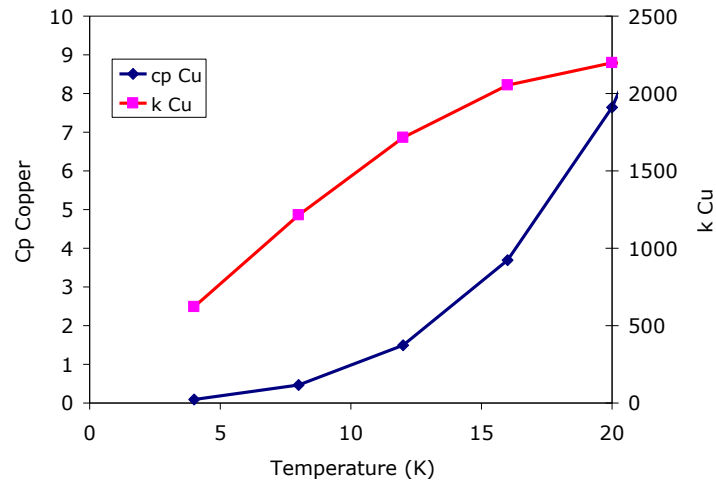


Fig. 9.3 Thermal properties of Cu at low temperatures.

The smeared properties of the winding pack are determined next. Because of the much lower thermal conductivity of the G10 compared with copper, the axial and radial thermal conductivity are determined mainly by the insulation. The calculated effective thermal conductivities are given in Table 9.2. It is assumed that the copper cross sectional area in calculating k_{eff} poloidal is 0.75, determined by the copper cross-section in the cable shown in Fig. 9.2. The thermal conductivity of the solder and the SC strands is neglected in this analysis.

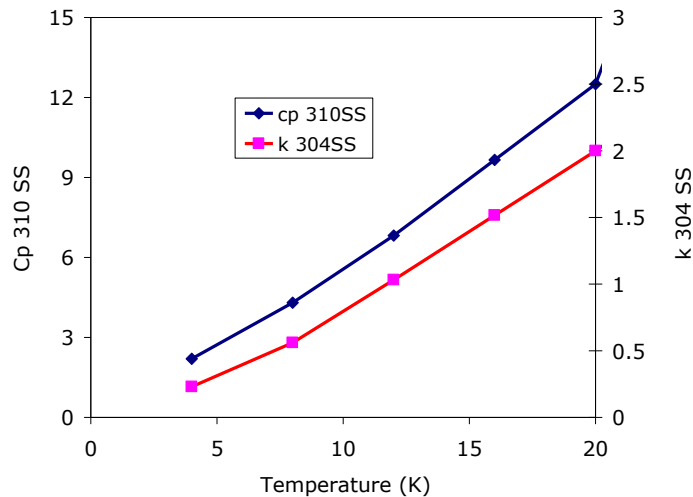


Fig. 9.4 Thermal properties of SS used in this analysis.

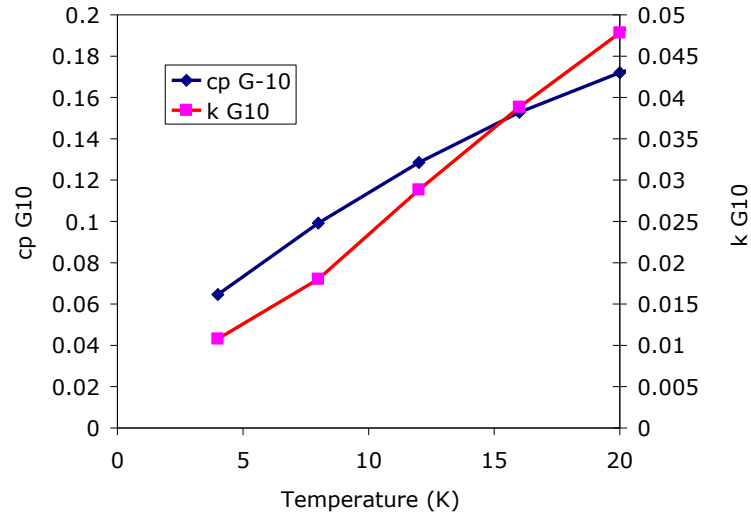


Fig. 9.5 Thermal properties of G10 at low temperatures

Table 9.2 Effective thermal conductivities in the smeared model

k_eff radial	0.64
k_eff axial	1.87
k_eff poloidal	467.10

9.2 Heating source

The heating source has been calculated by Zach Hartwig (Section 8.0), and is briefly presented here. The results from running Geant4 are shown in Fig. 9.6. The volume has been divided in 36000 cells, although the bulk of the cells are outside of the winding pack.

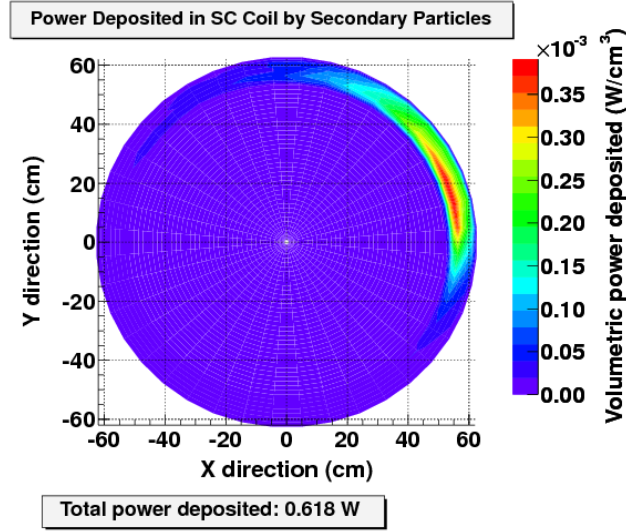


Fig. 9.6 Heating source determined by Hartwig using MCNP.

We have used regression to provide an analytical form for the heating source. The analytical form for the regression is:

$$H(r, z, \theta) = A \exp(-9.9 z) \exp(-21 r) \exp(-(\theta/25)^2)$$

Here, r is the radius in meters, z is the height in meters, and θ is the poloidal angle in degrees. Although it is possible to input directly the heating by interpolating, providing a smoother heating source provides for faster convergence. Also, the interpolation would result in the heating source increasing with radius at the inner radius, as shown in Fig. 9.6. By using the analytical model, it is possible to avoid this issue.

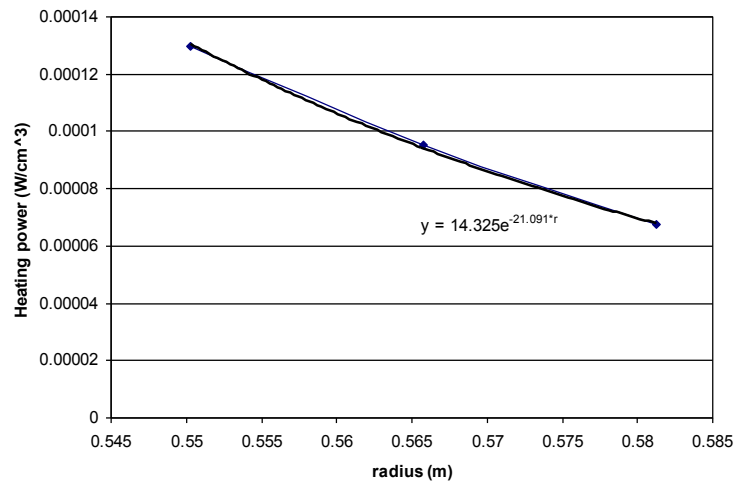


Fig. 9.7 Radial fit to the heating profile, for the cells at the bottom of the winding pack at the poloidal location near the peak of the heating.

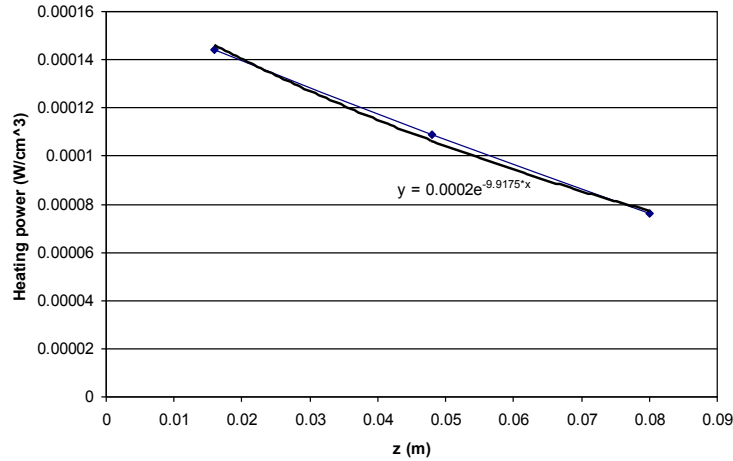


Fig. 9.8 Axial fit to the heating profile, for the cells at the innermost set of cells at the poloidal location near the peak of the heating.

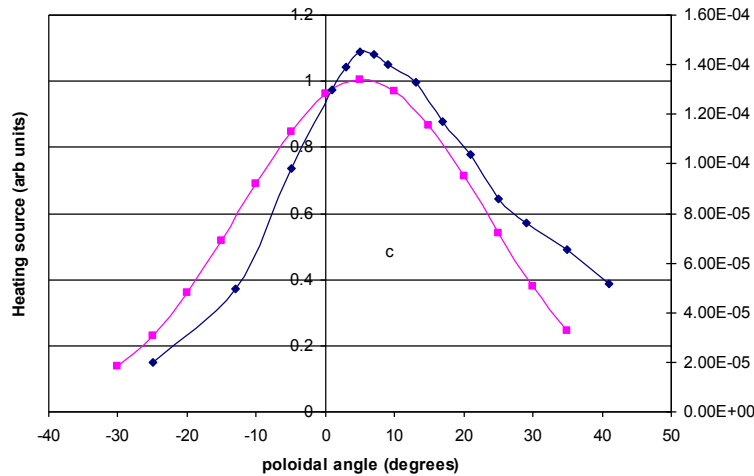


Fig. 9.9 Poloidal fit to the heating profile, for the cells at the innermost set of cells at the bottom of the winding pack.

The fits are shown in Fig. 9.7-9.9. The radial and poloidal profiles are calculated using the cells at the bottom of the winding pack (at 1.6 cm cell centroid), at the location of peak heat flux. The axial dependence is determined at the innermost cells of the winding pack, at a poloidal location with or near the highest flux.

The constant in front of the expression for the heating, A , is calculated by integrating numerically the heating source over the winding pack, and matching the number determined from the MCNP calculations (0.61 W over the winding pack). The constant is determined to be 453 W/m³, or about 0.5 mW/cm³, agreeing approximately with the peak heating shown in Fig. 9.6. The heating source in the model is shown in Fig. 9.10, on three planes at different heights of the coil. However, this heating source is about a factor of 3 larger than that shown in the Fig. 9.7-9.9. This issue is being investigated.

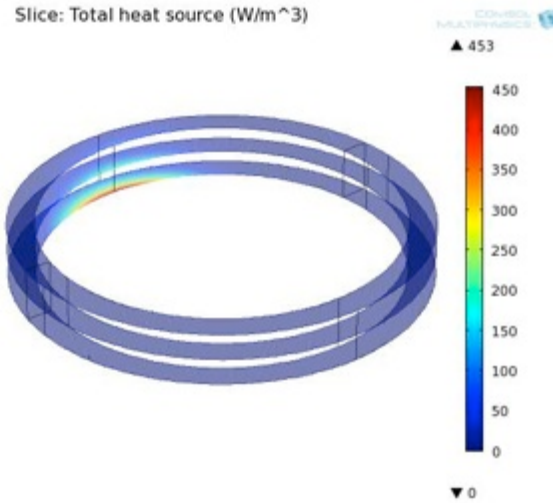


Fig. 9.10 Analytic heating source in the model.

9.3 Results without steel yoke

In the absence of the iron yoke in the calculations, the boundary conditions at the winding pack/steel interface is an insulator (that is, zero gradient). The boundary conditions on the rest of the winding pack are assumed to be 4.2 K. It is possible to set up a heat-flux like boundary condition, but the heat fluxes are so small that the temperature difference is negligible.

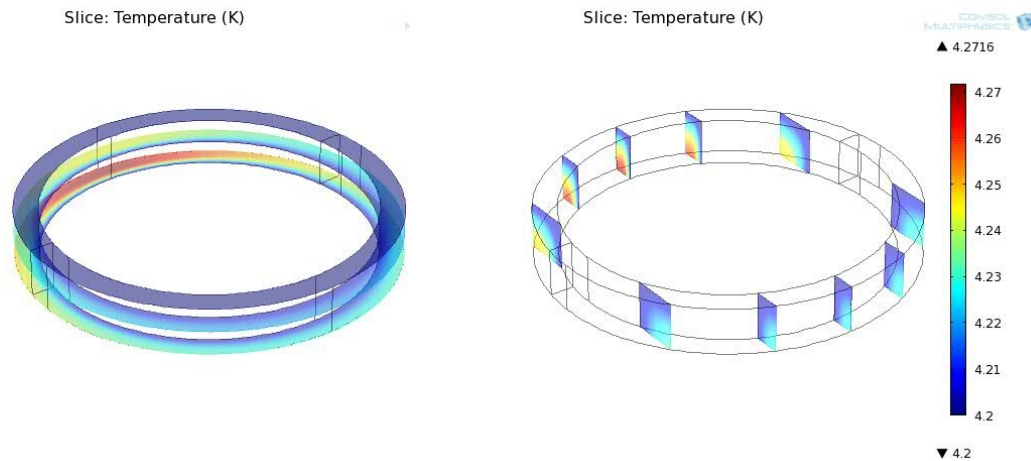


Fig. 9.11 Temperature along horizontal planes and along vertical planes on winding pack.

Figure 9.11 shows the temperature along a horizontal plane (left) and along vertical plane (right). The horizontal planes correspond to the bottom, top and in-between of the winding pack. The peak temperature is about 4.45 K, or a temperature excursion of about 0.3 K. The peak temperature occurs at the corner that is furthest away from the cooling surface, as the temperature needs to be monotonically increasing away from the cooling surface (no heat sinks, only heat sources). The peak temperature occurs in a region of relatively low magnetic field, in the outer section of the magnet.

9.4 Results with steel yoke.

In the case of the steel yoke, there is cooling on both the inner radius and the outer radius of the winding pack. All of the external regions model have a boundary condition at 4.2 K, with the exception of the bottom. The bottom region has a thermal insulation region (that is, zero gradient, from symmetry). The steel is isotropic, with a thermal conductivity of 0.23 W/ m K. The heating of the steel is neglected, but it can be added once it is determined.

The model is shown in Fig. 9.12. It is assume that there is a 2-cm thick steel at the bottom of the winding pack, and that the steel extends to a radius of 0.66 m, or 4 cm thick in the radial direction.



Fig. 9.12 Model with steel.

The temperatures are shown in Fig.9.13, for the same planes as Fig. 9.11. The peak temperature occurs in the bottom plane of the winding pack, but no longer at the corner. The steel reduces slightly the peak temperature, to about 4.4 K.

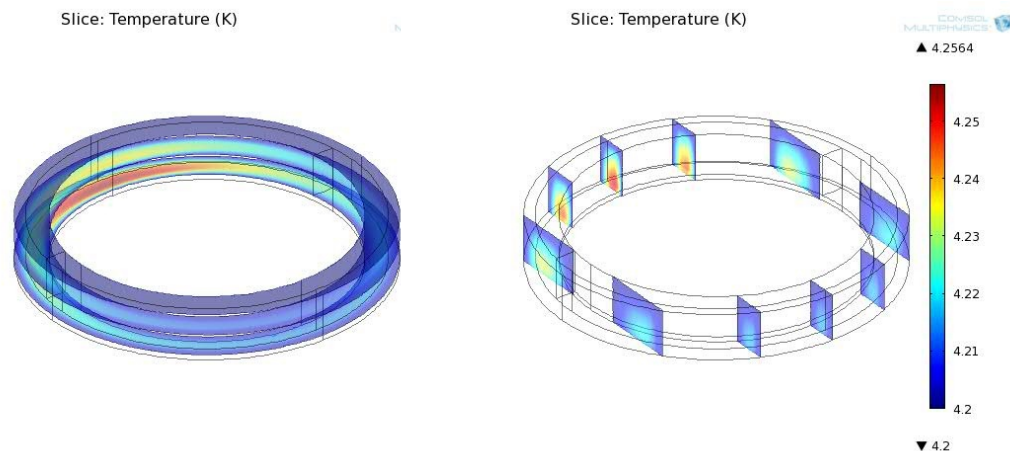


Fig. 9.13 Temperature profiles in the case with the steel.

9.5 Analytical model

In this section, an attempt to determine analytically the temperature excursions is presented. From the analytical heating model, the size of the radial and axial scales can be determined. They are:

$$\Delta r \sim 1/21 \sim 0.048 \text{ m}$$

$$\Delta z \sim 1/9.9 \sim 0.1 \text{ m}$$

The poloidal extent is determined by equating the flow times (radial and axial) with the poloidal. This assumption can be expressed as

$$k_{\text{axial}}/\Delta_{\text{pol}}^2 = k_{\text{radial}}/\Delta r^2 + k_{\text{axial}}/\Delta z^2$$

From this equation, it can be determined that $\Delta_{\text{pol}} \sim 1.4 \text{ m}$

The temperature excursion can be determined from the heat equation. By evaluating the heat flow due to axial temperature gradients and radial temperature gradients, the following approximation is obtained:

$$Q \sim \Delta T (k_{\text{radial}} \Delta_{\text{pol}} \Delta z / \Delta r + k_{\text{axial}} \Delta_{\text{pol}} \Delta r / \Delta z)$$

Where Q is the total heat into the model, $Q \sim .6 \text{ W}$ from the MegatronG4 calculations. The temperature excursion calculated from the above equation is $\Delta T \sim 0.1 \text{ K}$, approximately the same as the excursion from the FEM model.

10.0 Central Region Design

10.1 Introduction

A compact high field superconducting isochronous cyclotron, K250-42, is designed as a proof-of-principle for a single stage high power proton accelerator. This cyclotron is to accelerate proton to a final energy of 250 MeV with two 45° dees with a radius $\sim 40 \text{ cm}$. By employing a 20 mA external ECR proton source, the injected proton beam currents at high brightness are foreseen. Using phase selection in the center, a fully magnetized elliptical pole, low energy gain per turn, a precise relation between momentum and radius at large radius are expected. Two goals, a) to use this relationship to develop multi-turn extraction with passive elements only, to achieve a high external proton beam intensity ($\sim 1 \text{ mA}$); and b) to see if it is possible to achieve a high extraction efficiency ($> 99\%$) without single turn extraction, with an energy spread $|DE/E| \sim 0.1\%$. The RF acceleration is on the first harmonic with $\omega_{\text{rf}} = \omega_0 \sim 64 \text{ MHz}$. Note that this frequency was reduced from the originally assumed 84 MHz due to subsequent calculations. Superconductor coils will provide a central field of $B_0 \sim 4.3 \text{ T}$ and a peak hill field of 6.6 T.

Table 10.1 Principal parameters of the cyclotron

- 4 sectors, 2 Dees
- Synchronous Particle: $\Delta E = N_{\text{gap}} e V_0 \sin\left(\frac{h\theta_{\text{dee}}}{2}\right)$,

- h : harmonic $\# = 1$; $N_{\text{gap}} = 4$;
- $\theta_{\text{dee}} = 45^\circ$;
- $V_0 = 85.4 \text{ keV}$
- $\Delta E = 0.131 \text{ MeV}$
- 1900 acceleration turns
- $\omega_{RF} \sim 4 \times 10^8$, $f_{RF} \sim 60 \text{ Mhz}$
- $B_0 \sim 4.3 \text{ T}$

10.2 Magnetic field design

The isochronous field requires a complicated magnet design. In addition, to generating a sufficiently high field, a new ferromagnetic material-Holmium, is under investigation. The properties of Holmium shows better ferromagnetism than iron.

The following formulas show the isochronous requirement:

$$\omega = \frac{qB}{m} = \frac{qB}{\gamma m_0}$$

$$\gamma(r) = \frac{E(r)}{E_0} = \frac{1}{\sqrt{1 - \left(\frac{qB_0 c}{E_0}\right)^2 r^2}}$$

$$B(r) = \gamma(r)B_0 = B_0 \frac{1}{\sqrt{1 - \left(\frac{qB_0 c}{E_0}\right)^2 r^2}}$$

There are two basic characteristics of the beam dynamics: the isochronism of the field, and the betatron oscillation.

In a four-sector machine, for a synchronous particle to be accelerated, the acceleration per turn is

$$\Delta E = N_{\text{gap}} e V_0 \sin\left(\frac{h\theta_{\text{dee}}}{2}\right),$$

h : harmonic $\# = 1$; $N_{\text{gap}} = 4$; $\theta_{\text{dee}} = 45^\circ$; $V_0 = 85.4 \text{ keV}$

$\Delta E = 0.131 \text{ MeV}$ for 1900 accelerating turns.

While all the real particles are not synchronous, if we want them to be captured into acceleration, we should take into consideration the mis-isochronism, which is the differential phase error and the integral phase error for the whole accelerating path. The differential phase error is:

$$\frac{d\phi}{d\theta} = \left(\frac{\omega_{RF}}{\omega} - 1\right) = \frac{B_{\text{iso}} - B_{\text{ave}}}{B_{\text{ave}}}$$

With phase error, the acceleration ratio is

$$\Delta E = 4eV_0 \sin(22.5^\circ - d\phi)$$

A large phase error, either differential for big kick or integral for accumulative effect, may cause deceleration or particle loss.

Furthermore, tunes $v_r^2 = 1 - n$, $v_z^2 = n$ of the betatron oscillation indicate the stability of the acceleration. We require both to be larger than zero. An isochronous cyclotron is a strong focusing accelerator with field index $n = -\frac{r dB}{B dr} < 0$, which makes a strong focusing in the radial direction ($v_r^2 = 1 - n$), and a strong defocusing in the vertical direction ($v_z^2 = n$). Thus, we need to add flutter, the variance of the magnetic field between the hill magnet poles and the magnet valley.

The flutter is calculated as:

$$F(r) \equiv \frac{1}{2\pi} \int d\theta \left[\frac{B_z(r, \theta) - \langle B_z(r) \rangle}{\langle B_z(r) \rangle} \right]^2$$

And the new betatron tunes are:

$$\begin{aligned} v_r^2 &= 1 - n + F \times \frac{n^2}{N^2} + \dots \\ v_z^2 &= n + F(1 + 2\tan^2\zeta) + \dots \end{aligned}$$

With enough flutter, we can have stable acceleration.

10.3 Material: Holmium

With Holmium, we can easily get a field peak ~ 7 T and enough flutter for the focusing target which will be described later (see Fig. 10.1).

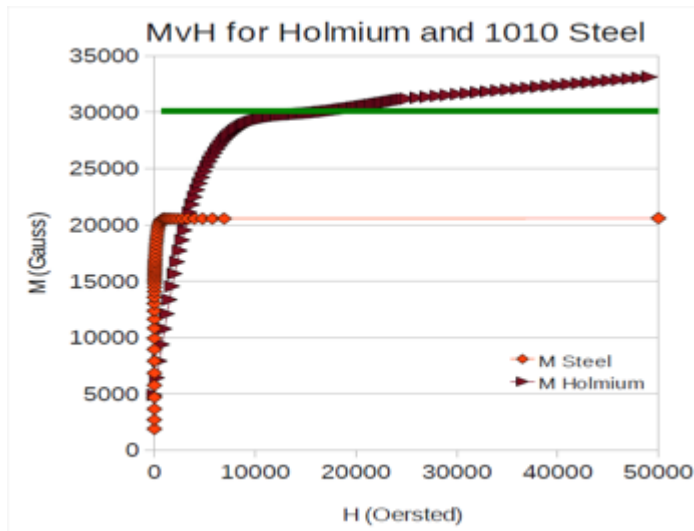


Fig. 10.1 Comparison of the magnetism of Holmium and Steel

10.4 Magnet design

Currently, we have two basic models of the magnet: one with higher field and one with a larger radius. The general beam properties will be shown. The models were built on OPERA-3D, and the beam properties were calculated on GENSPERO. Figure 10.2 shows the OPERA model for design 406.

10.4.1 Model 406

Model 406 has a larger radius with lower magnetic field. It reaches 250 MeV at radius $r = 0.52$ m.

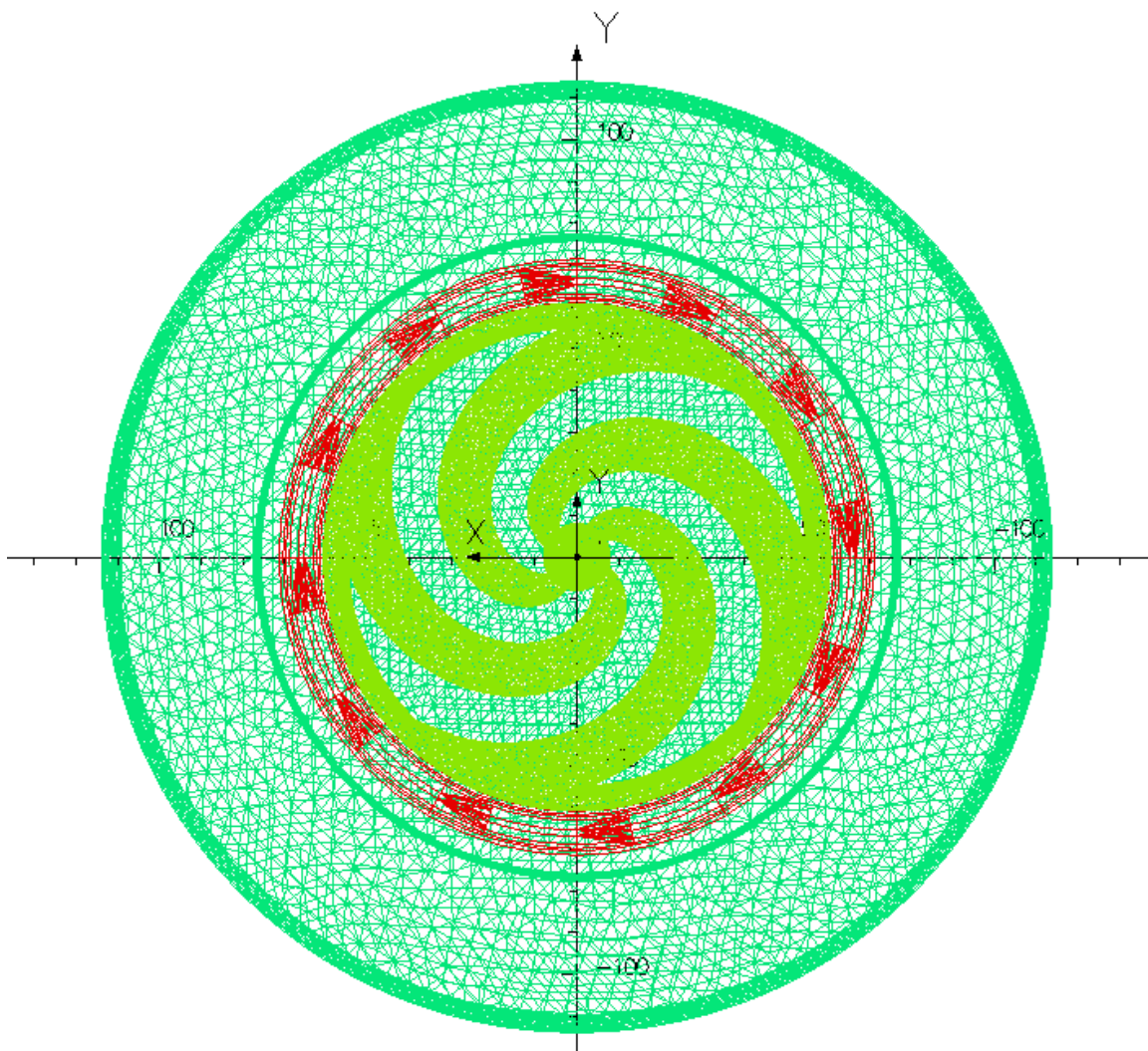


Fig. 10.2 OPERA design of the Model 406

The magnetic field and the beam properties of Model 406 are shown in Fig. 10.3.

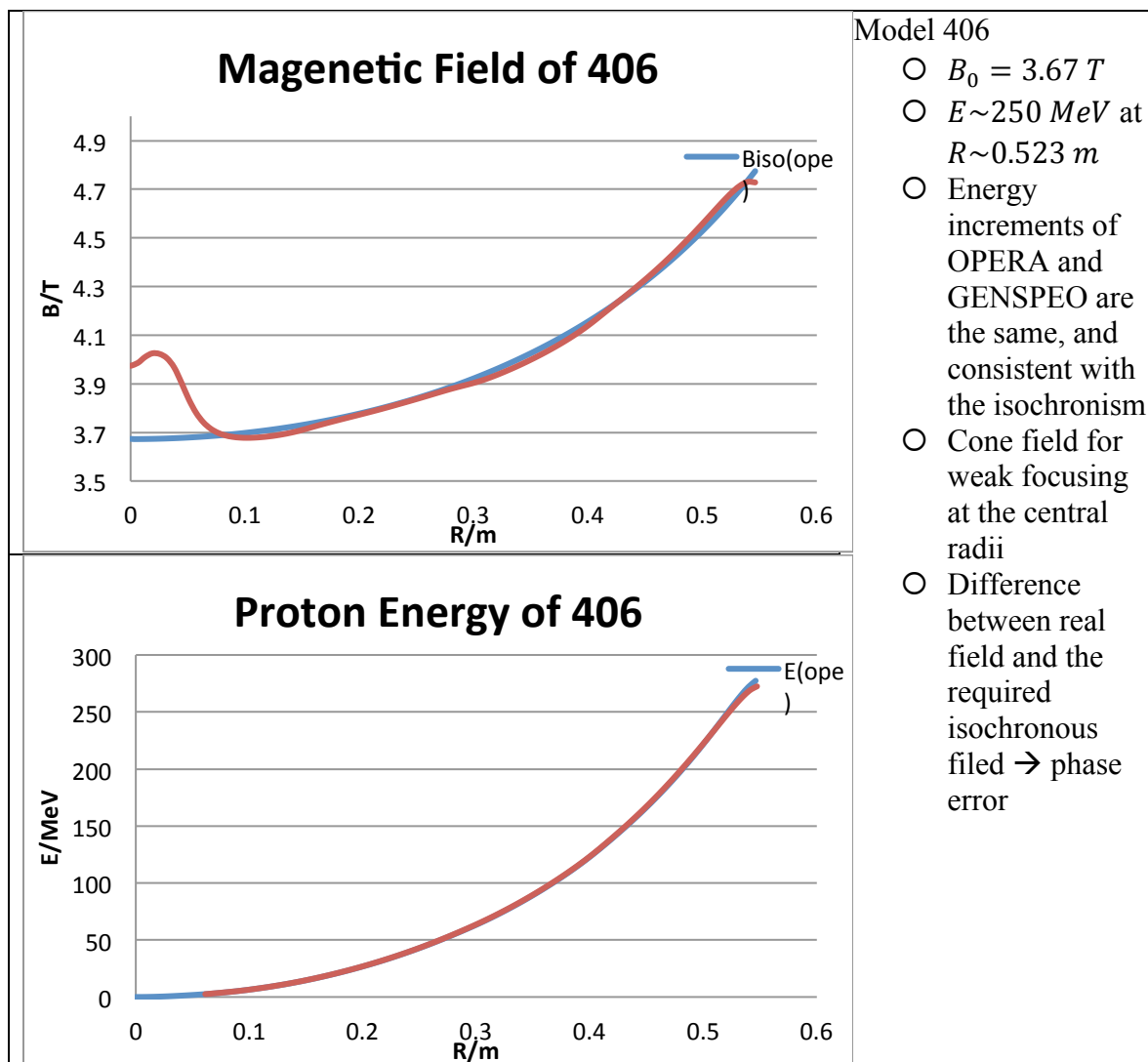


Fig. 10.3 The magnetic field and the proton energy of Model 406

The phase properties of Model 406 are shown in Fig. 10.4, and the betatron oscillations in Fig. 10.5.

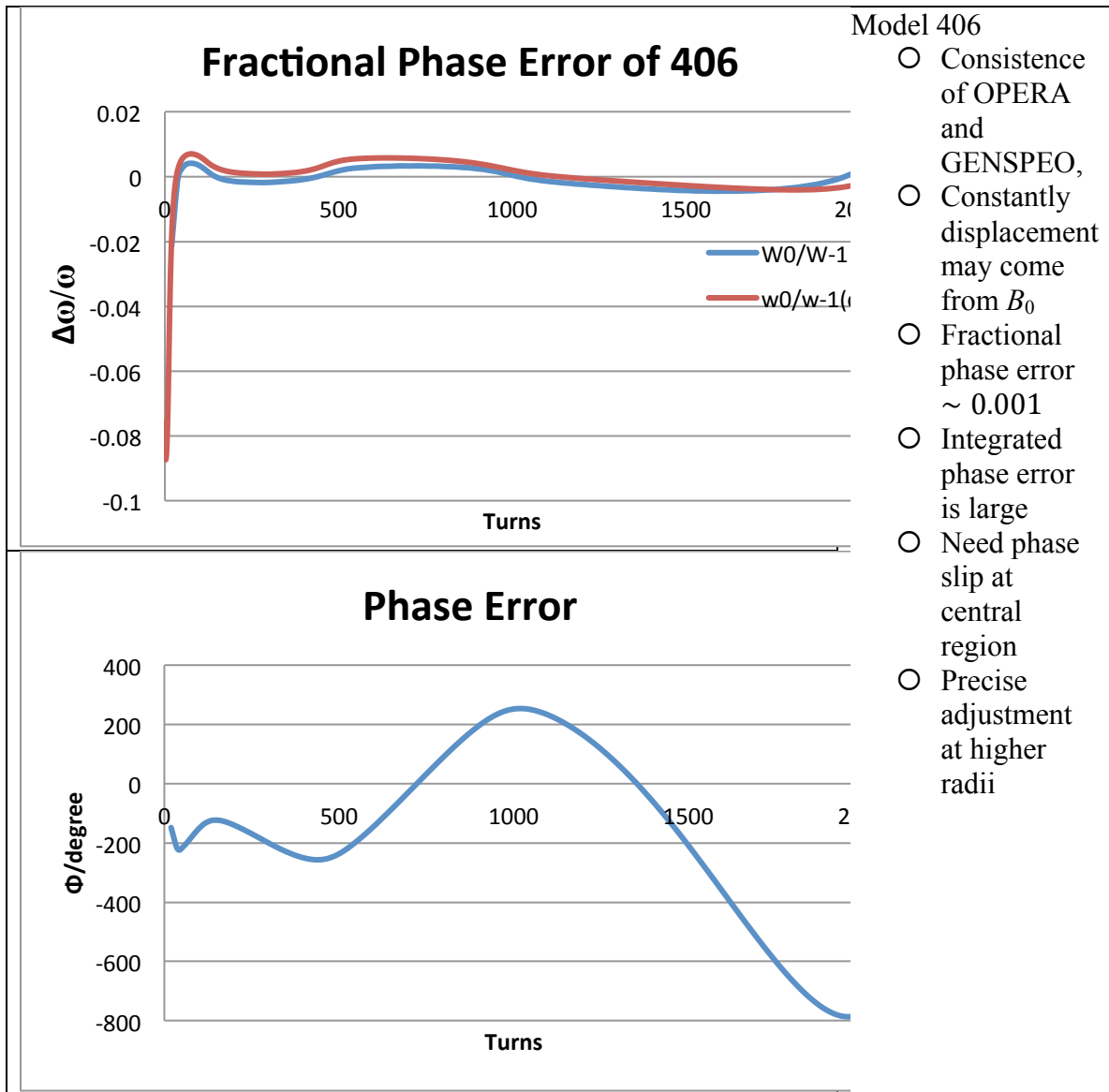


Fig. 10.4 Phase properties of Model 406

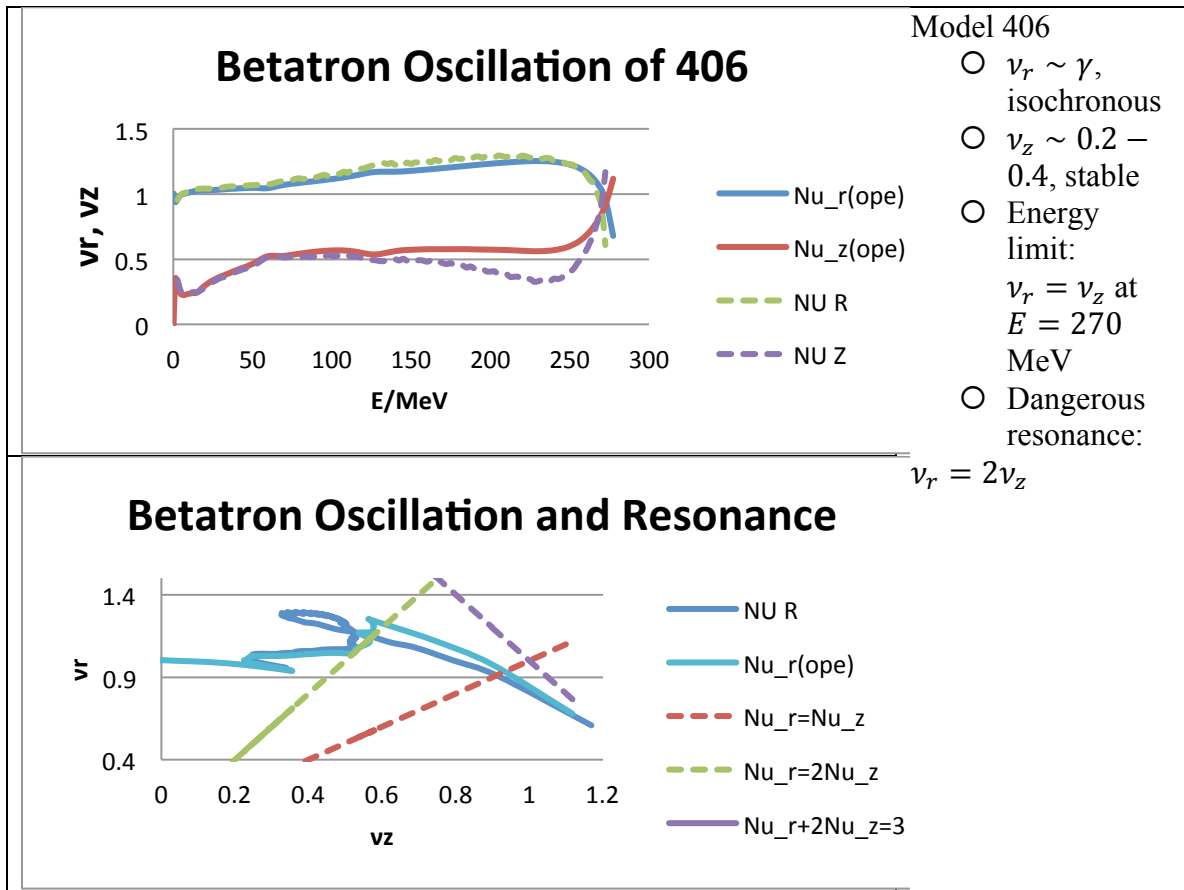
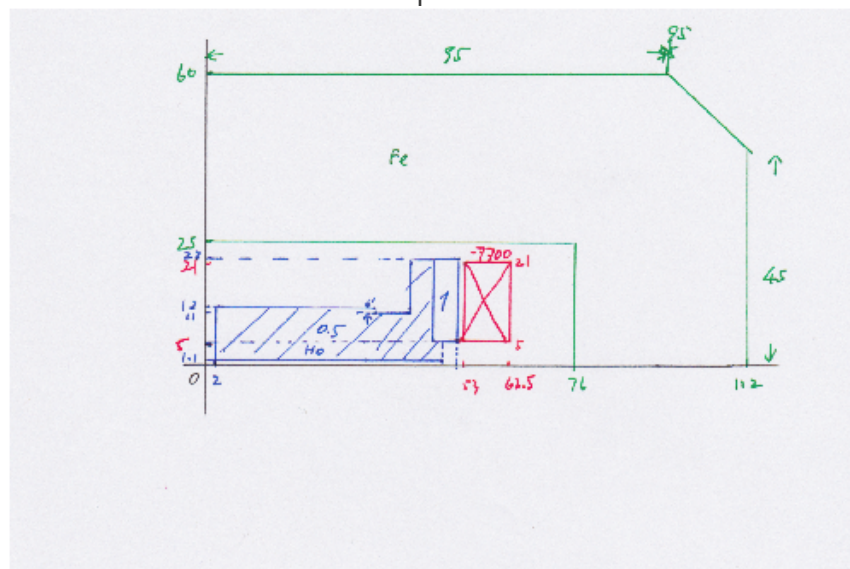


Fig. 10.5 Betatron tunes of Model 406

10.4.2 Model 018H

Model 018H has a smaller radius and a higher magnetic field. Due to the advanced design, we use this model to build an idealized magnetic field for following calculations as E-field and central field design. The OPERA model of design 018H is shown in Fig. 10.6.



82

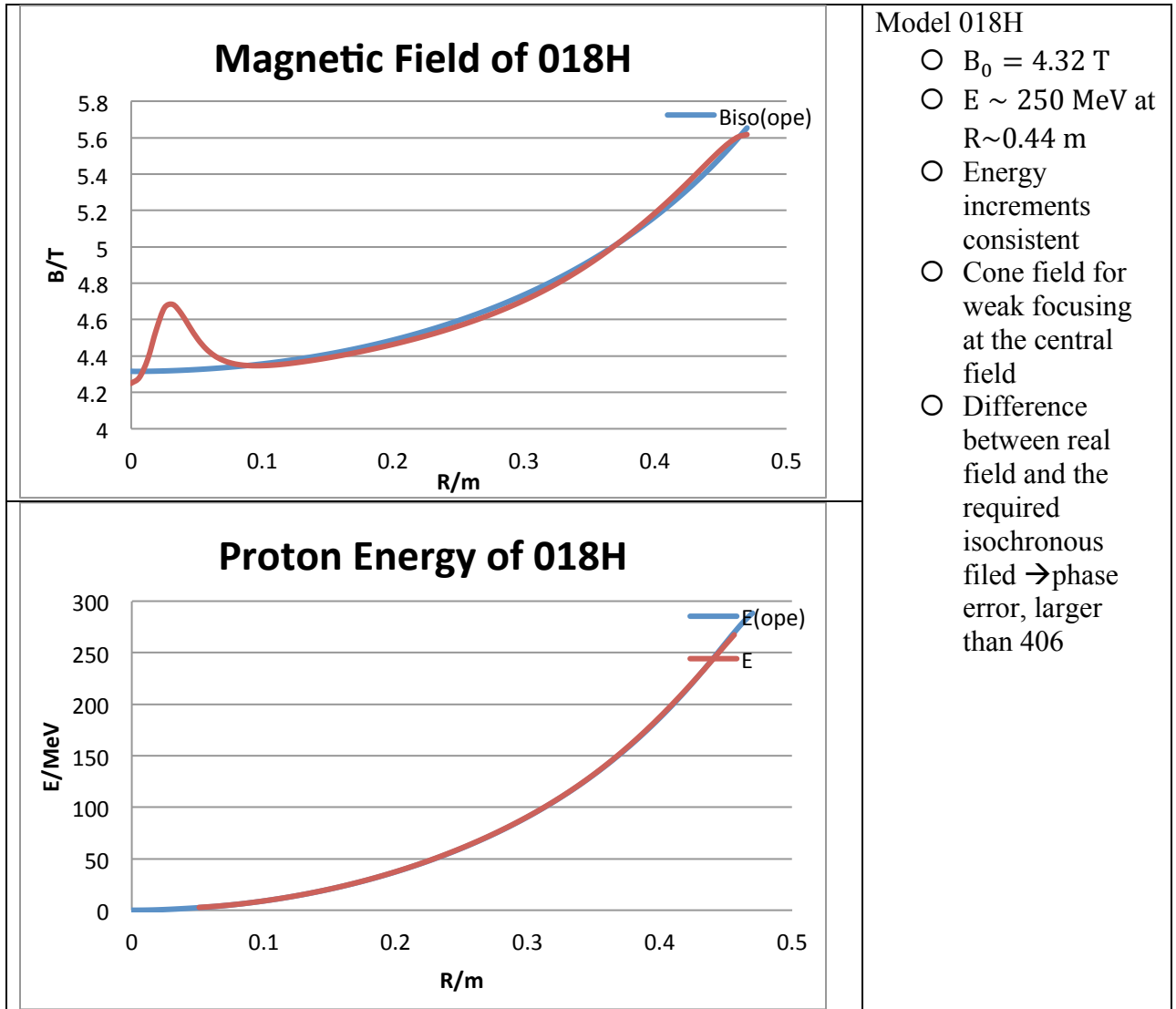


Fig. 10.7 The magnetic field and the proton energy of Model 018H

The magnetic field distribution and the proton energy of Model 018H are shown in Fig. 10.7.

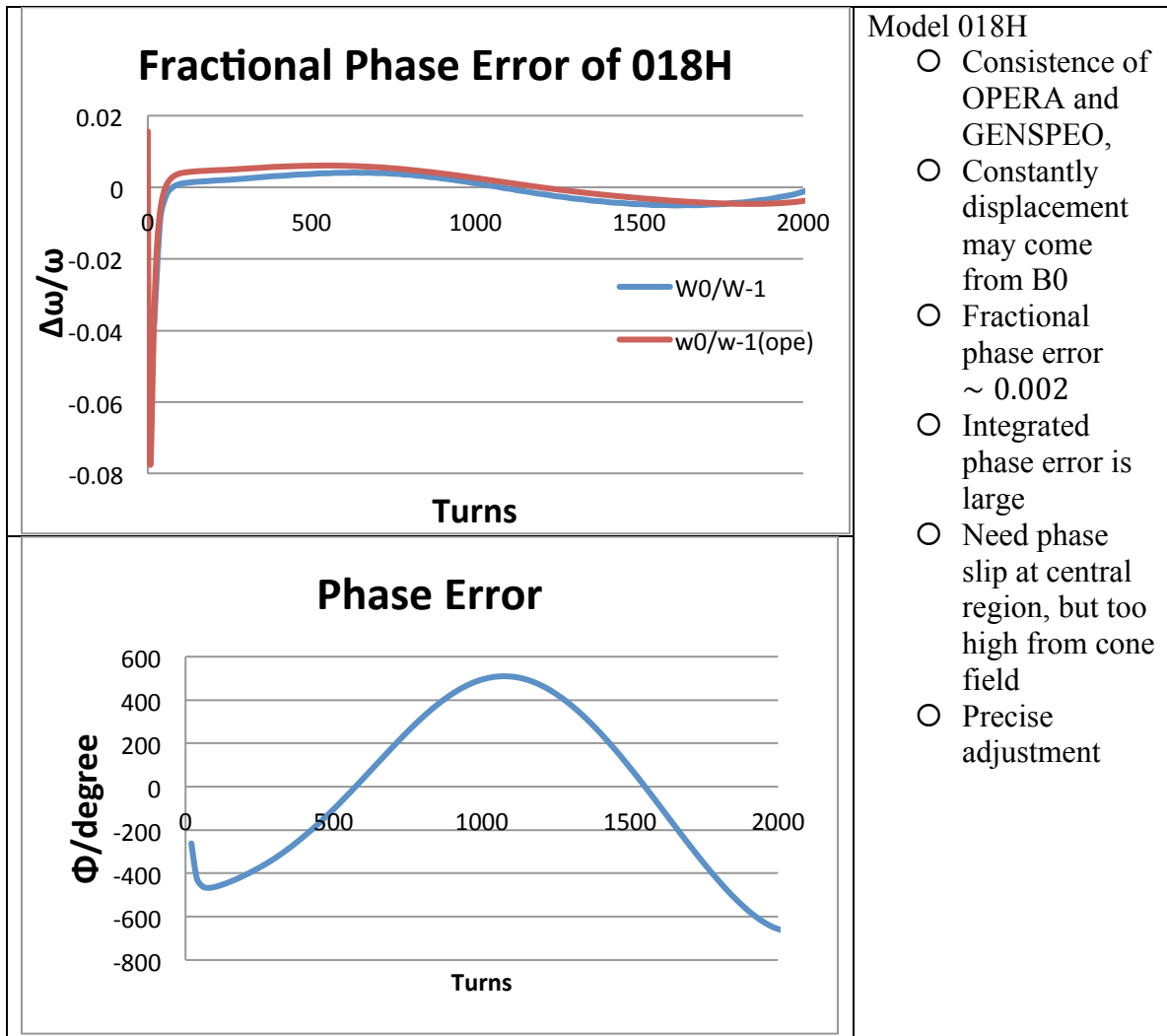


Fig. 10.8 Phase properties of Model 018H

The phase properties of Model 018H are shown in Fig. 10.8, and the betatron oscillations in Fig. 10.9

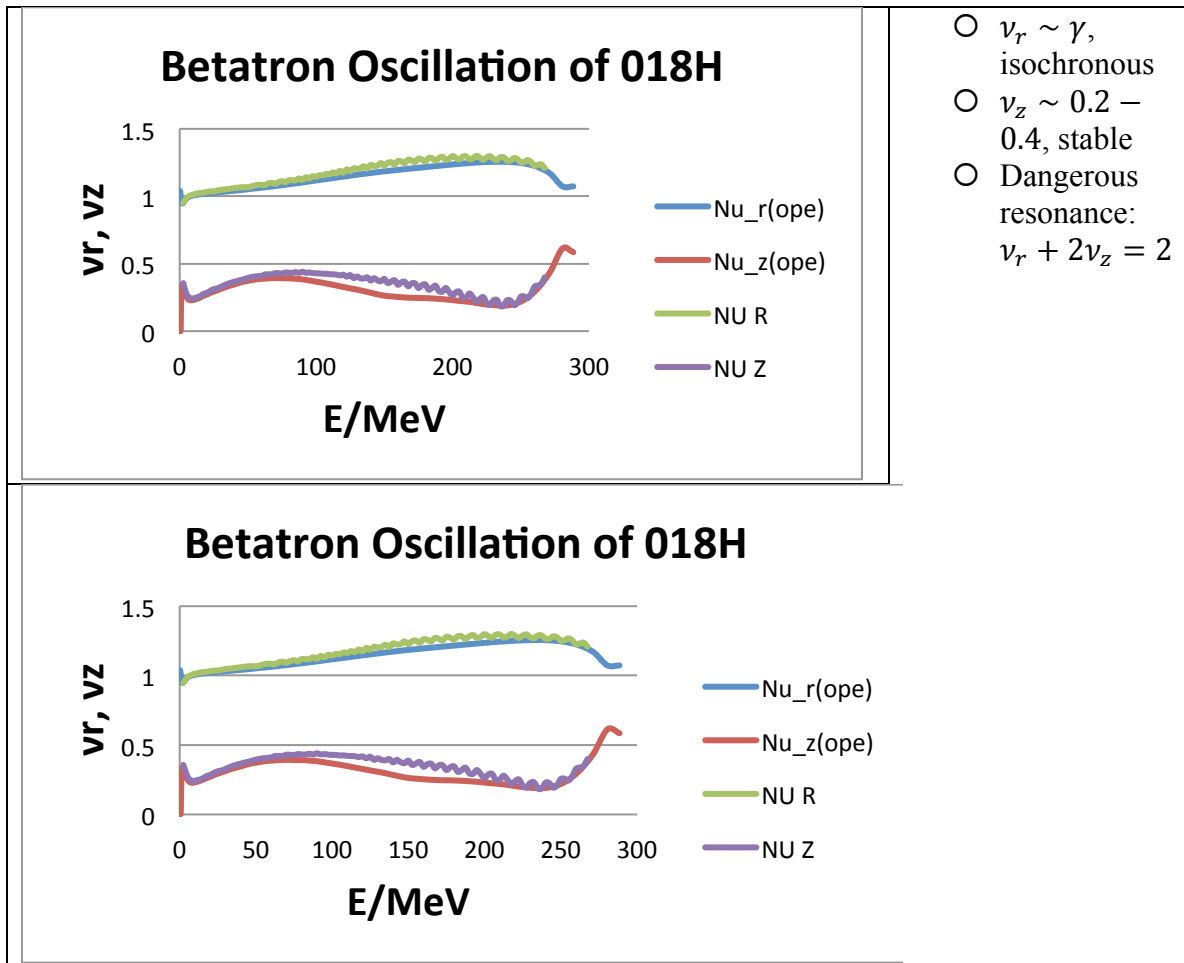


Fig. 10.9 Betatron tunes of Model 018H

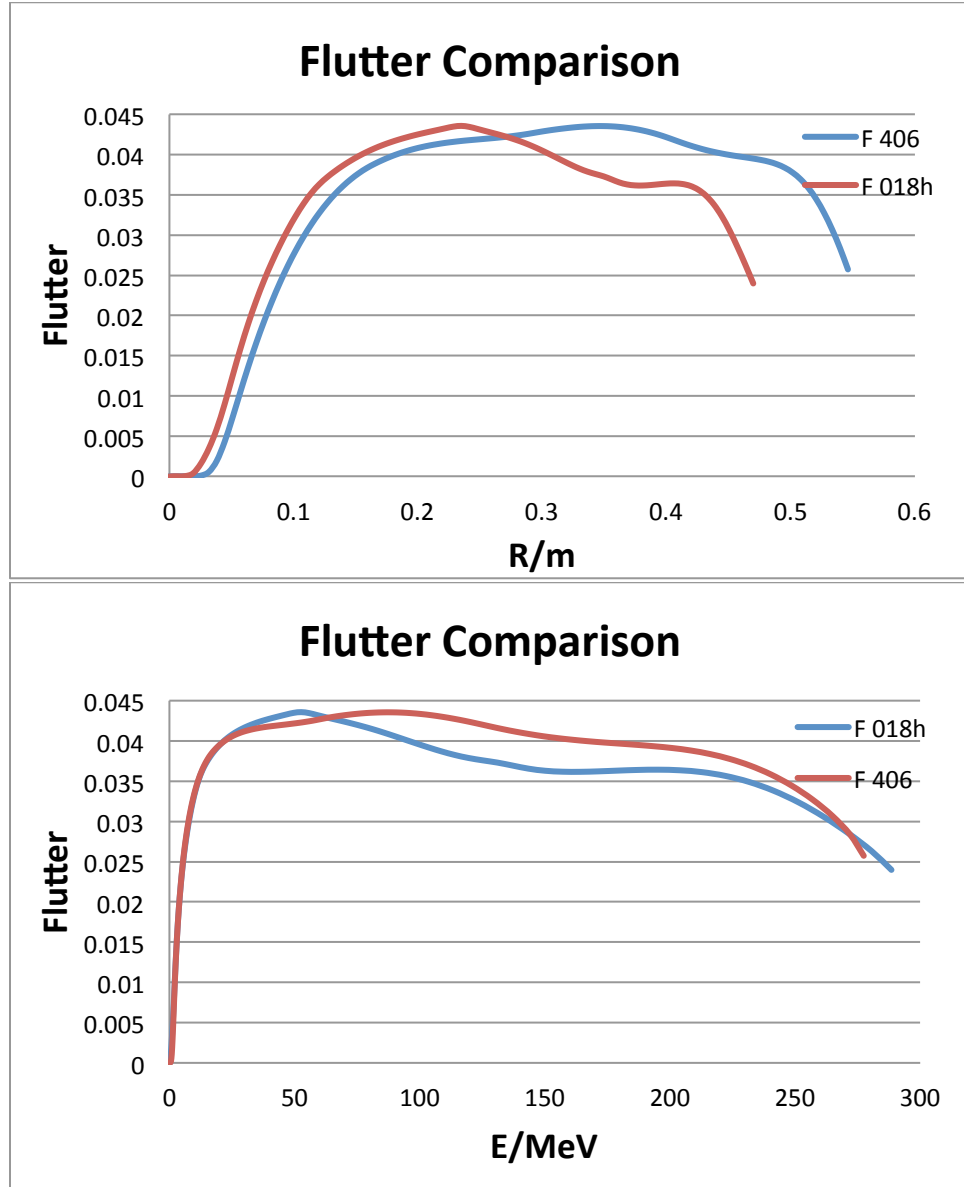


Fig. 10.10 Flutter comparison of the two models

Comparing the two models for betatron oscillation and flutter (Fig. 10.10), both show enough flutter for the major radial and energy range.

10.4.3 Idealized Magnetic Field

The above two models show general good beam properties (Fig. 10.10). But yet the careful adjustment is needed to meet the precise requirement. And the magnet design also requires the iteration of the beam dynamics in electric acceleration and the magnetic field. In order to get down to the beam dynamics calculation quickly, we idealize the magnetic field to best match the requirement first.

Method to generate the ideal isochronous field is: based on the model 018H, employing uniform M approximation, we can generate the ideal magnetic field. Because the ferromagnetic material, Holmium, is saturated, so we can change the average magnetic field over one turn, $B_{ave}(R)$, without changing the absolute difference of the field between the valley and the hill, ΔB . So

$$\begin{aligned}
 B_{ideal}(R, \theta) &= B_{sim}(R, \theta) - B_{ave}(R) + B_{iso}(R) \\
 B'_{ave} &= \frac{1}{2\pi} \int_0^{2\pi} B_{ideal}(R, \theta) d\theta = \frac{1}{2\pi} \int_0^{2\pi} (B_{sim}(R, \theta) - B_{ave}(R) + B_{iso}(R)) d\theta \\
 &= \frac{1}{2\pi} \int_0^{2\pi} B_{sim}(R, \theta) - B_{ave}(R) + B_{iso}(R) = B_{ave}(R) - B_{ave}(R) + B_{iso}(R) = B_{iso} \\
 Flutter' &= \frac{1}{2\pi} \int_0^{2\pi} \frac{(B_{ideal}(R, \theta) - B'_{ave}(R))^2}{B'_{ave}(R)^2} d\theta \\
 &= \frac{1}{2\pi} \int_0^{2\pi} \frac{(B_{sim}(R, \theta) - B_{ave}(R) + B_{iso}(R) - B_{iso}(R))^2}{B_{iso}(R)^2} d\theta \\
 &= \frac{1}{2\pi} \int_0^{2\pi} \frac{\Delta B_{sim}(R, \theta)^2}{B_{iso}^2} d\theta
 \end{aligned}$$

In addition, in the central region, a cone field is necessary for vertical focusing because the flutter is so small in the few turns. So a $\sim 30^\circ$ phase shift within the first turn is natural. Based on Henry Blosser's Notes of the MSU Cyclotron, a few tens of Gauss of pump up of the magnetic field meets the requirement.

Based on the Model 018H, an idealized magnetic field is shown Fig. 10.11 and in Figs. 10.12 and 10.13.

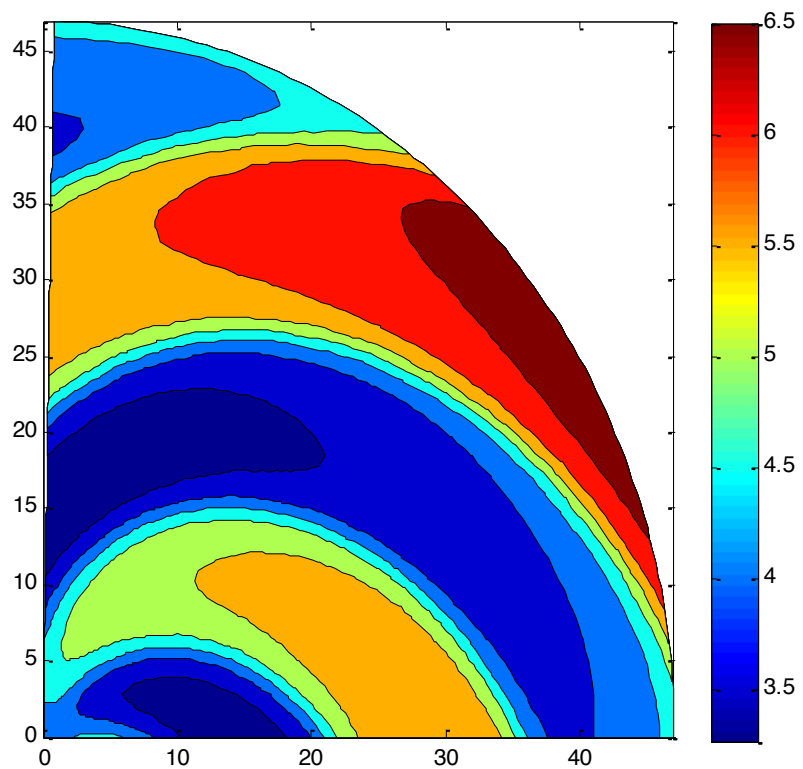


Fig. 10.11 Ideal Isochronous Magnetic Field contours for Model 018H.

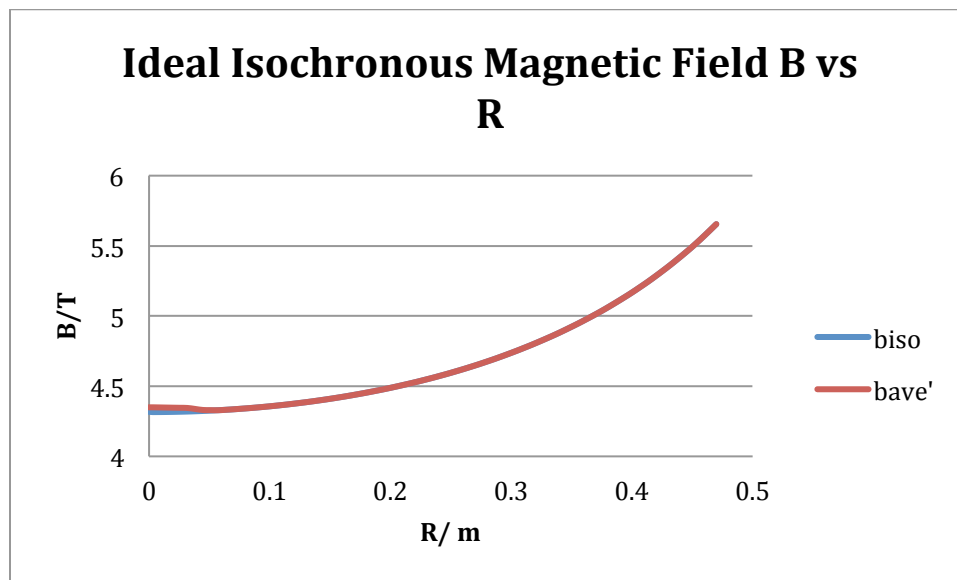


Fig. 10.12 Ideal Isochronous Magnetic Field B vs R

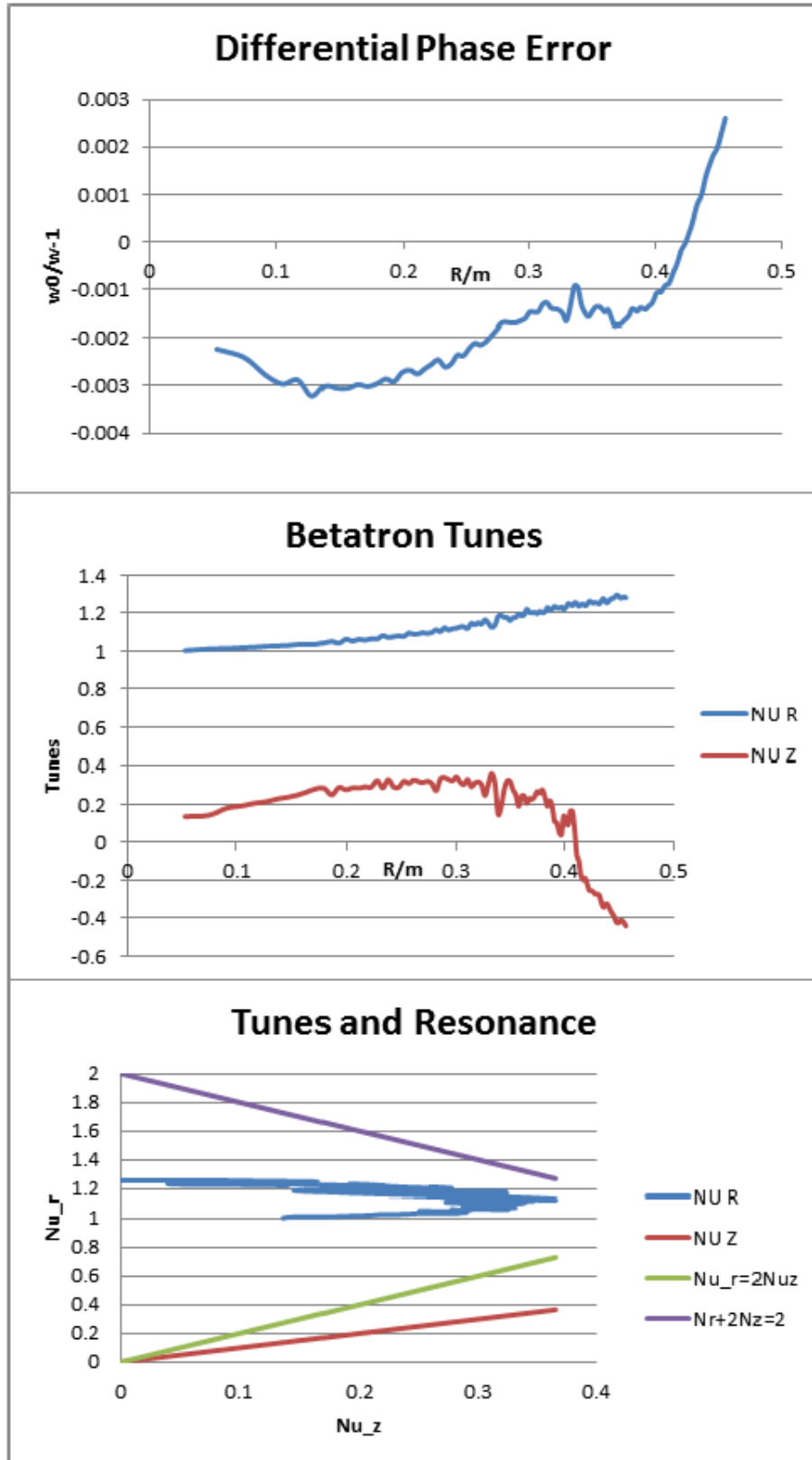


Fig. 10.13 The general beam dynamics of the ideal magnetic field

10.4.4 Summary

Generally, the two models, 406 and 018H are primarily in good shape. Careful modifications are under design, which requires the calculation of beam dynamics through acceleration. To get things started first, based on the model 018H, we generated an idealized magnetic field for the future simulation. The final magnet design will begin with the idealized field and the new calculation. Also, due to the higher flutter and higher energy limit properties, a 3-sector machine is also under consideration.

10.5 Central Region

The first accelerating gap is between the ion source and the first dee tip, also called the "puller". The energy gain of the particle in the first gap is critical. Without enough energy gain, particles will be pulled back to the source or will hit the puller, leading to huge particle loss at the very beginning. It is, thus, very important to study the particle trajectories in the first gap for different injecting conditions. In addition, it is important to try to make the optimum injection time match the peak accelerating RF electric field. Fortunately the transit time effect is limited due to the high magnetic field. This makes it easier to perform a precise study of the central region.

10.5.1 Part I: Source to Puller Gap

The software OPERA-3D was used to generate a simplified source-to-puller electric field map. Figure 10.14 shows the OPERA electric field model for the puller. The source-to-puller distance is 0.5 cm, the same as the accelerating spiral gap at $r \leq 5$ cm in the cyclotron. The amplitude of the accelerating field is about 86 KV.

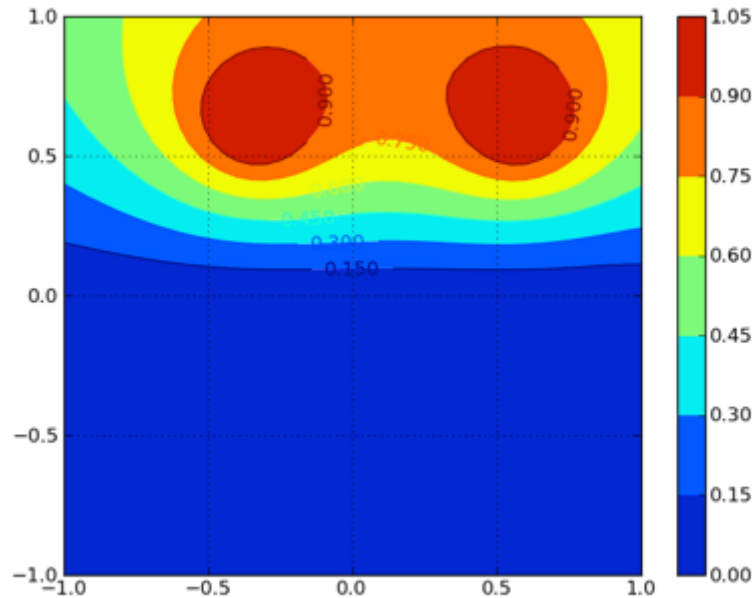


Fig. 10.14 The source-to-puller electric field map

The beam code Z3CYCLONE was employed to calculate the ion trajectories in the first gap for different starting conditions. For all the cases, the field map is laid with a -30° rotation angle with respect to the magnetic field map due to the configuration of an ECR ion source and a spiral inflector. In Z3CYCLONE, two coordinate systems are overlapped. One is the absolute coordinate (x, y) matching the magnetic field and the other is the particle coordinate (ξ, η) based on the particle source. Four different cases are shown in Fig. 10.1d with varied starting time phase, injecting angle, injecting ξ_0 and η_0 positions.

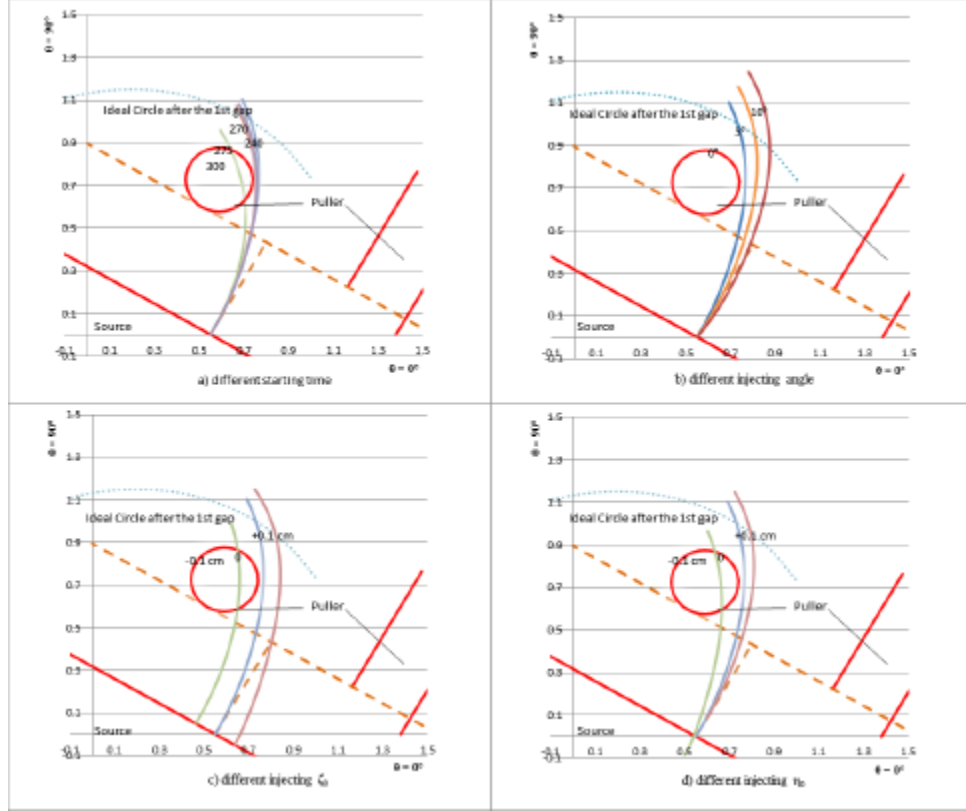


Fig. 10.15 Ion trajectories with different injecting situations of a) starting time, b) injecting angle, c) injecting position ξ_0 , d) injecting position η_0

In order to be accelerated to the final energy, it requires particles not to hit the puller or to strike back to the source. In addition, the particles need to gain more energy and the system to be operated easily. Figure 10.15 shows that the best way to inject protons on the starting phase of $\tau = 240^\circ$ with respect to the RF electric field of the first dee, and setting the injecting angle to be 0° , the injecting position should at be $\xi_0 = 0$, $\eta_0 = 0$. Setting the injecting angle to be either 5° or 10° is also a good option.

10.5.2 Part II: Inner Large E-Map

The part II of Z3CYCLONE concerns the first few turns, so it is used to generate the small electric field map. The software SOLIDWORKS was used to build the precise model first, Fig. 10.16, which was then imported to OPERA-3D to generate the static electric field map, Fig. 10.17.

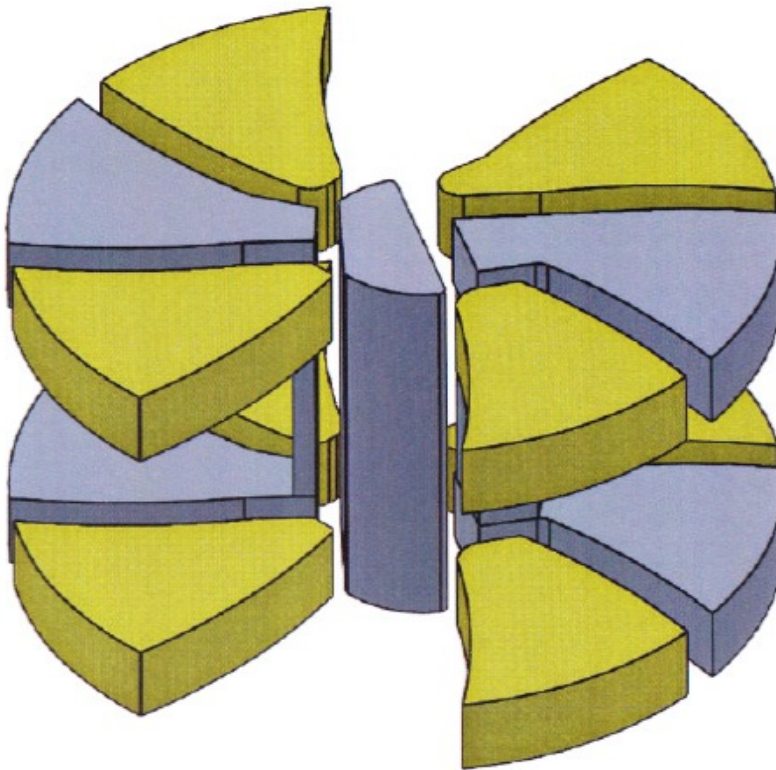


Fig. 10.16 Design of the cyclotron central region part II

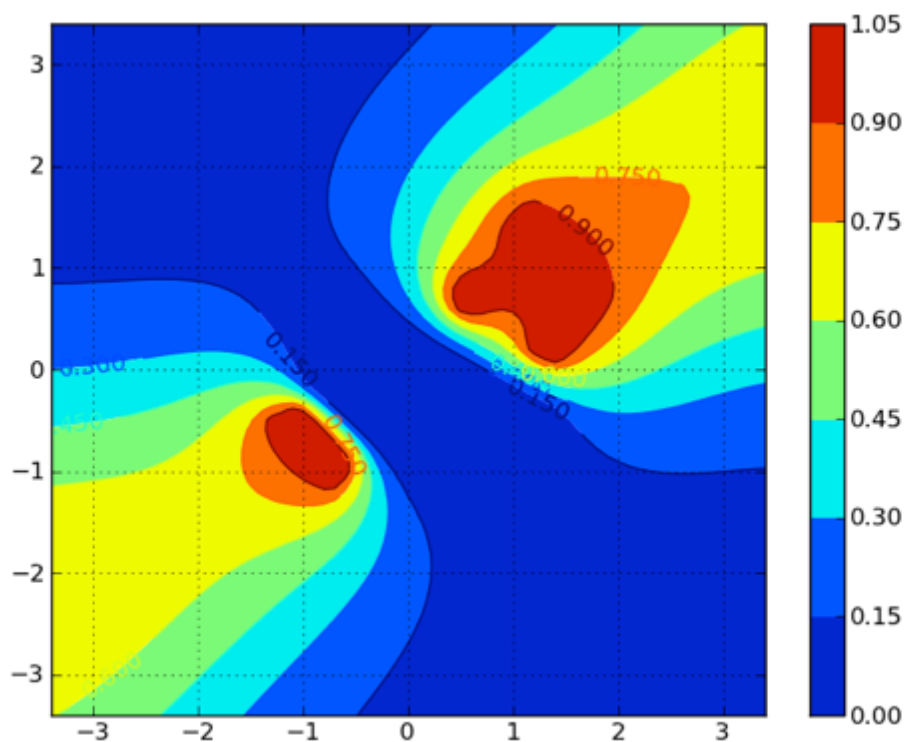


Fig. 10.17 The electric field of part II

The Z3CYCLONE part I and II were being calculated at the time of contract termination, so this work was not completed. The initial results for Part I are given in Fig. 10.17 and 10.18 which shows the E field after four turns. It shows that the ion may hit the puller during acceleration. Careful modifications, both about the shape of the poles in OPERA-3D, and the initial conditions in the Z3CYCLONE code will have to be made to correct this issue.

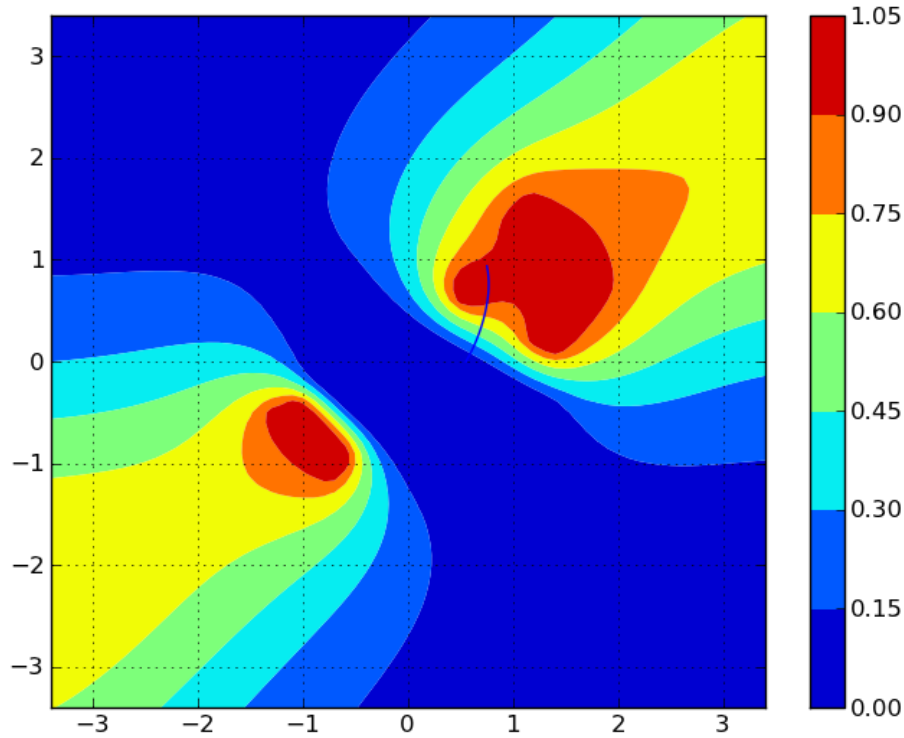


Fig. 10.18 The ion trajectory from Z3CYCLONE part I

10.6 Future Work

The next step will be to employ Z3CYCLONE to achieve full acceleration from the exit of the inflector to the extraction location. The ion path with zero current (no space charge effect) under the magnetic field will be performed. Based on the iteration of the beam dynamics calculation and the design of the pole shapes, new requirements for the entire magnetic field map will be proposed that will call for precise modification of the magnet design of the existing Model 018H.

The external ECR ion source should be designed and then the trajectory from the injection path to the inflector will be performed. Due to the high intensity, the space charge effect should then be added to the zero current calculation, especially in the inflector and the central region.

The compact size does not allow space for septum extraction. We will consider using the methods of field kick or resonance to achieve extraction “automatically”. Thus the possibility of non-resonant multi-turn self-extraction should be studied and the shape of the outer-edge magnet should be re-designed.

10.7 References

- [1] T. Antaya and J. Feng, MIT PSFC RR-07-11. 2007
- [2] T. Antaya, PSFC RR-09-16. 2009
- [3] M. Norsworthy, MIT Thesis. 2010
- [4] H. Blosser, D. Johnson, NIM. I21 (1974) 301
- [5] H. Blosser, MSUCP. 1971
- [6] E. Liukko

11.0 RF System Design

The RF system was designed by Dr. John Vincent at Michigan State University (MSU) under a subcontract from MIT. He completed his Phase 2a work statement within the limitations of the technical information provided to him by MIT and consistent with the directed work closeout directions from PSU.

11.1 System Introduction

The RF system components are shown schematically as a block diagram in Fig. 11.1.

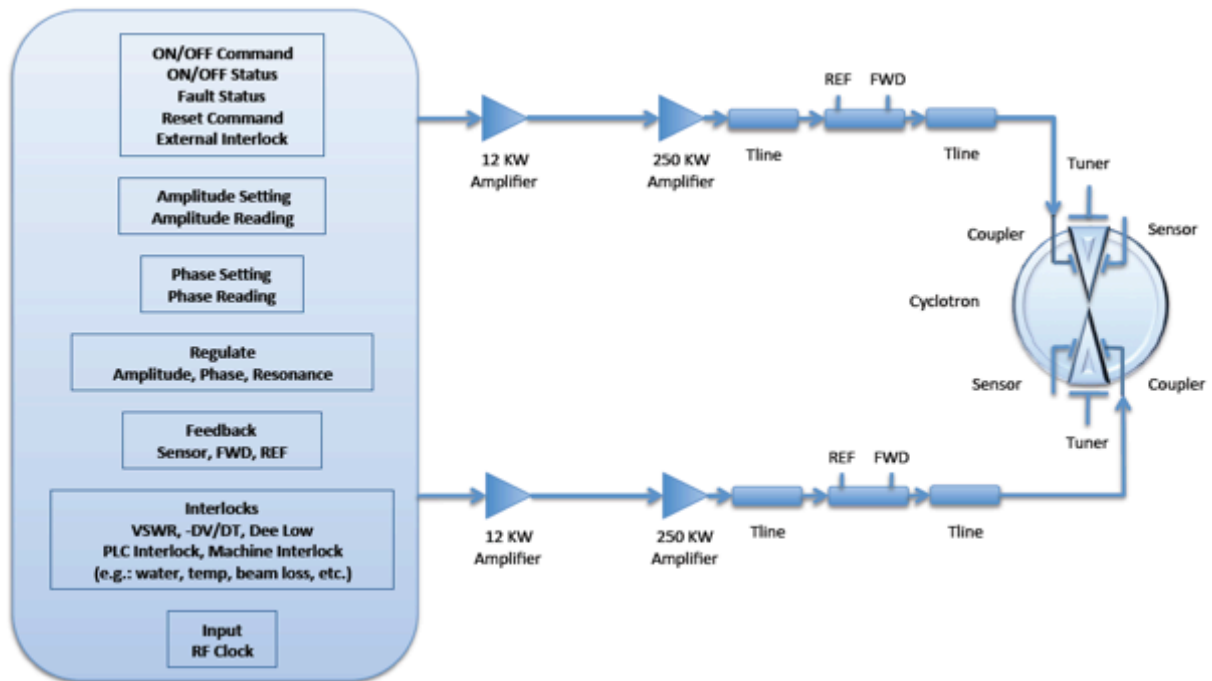


Fig. 11.1 Schematic of Megatron RF system components.

11.2 System Outline and Parameters

The system geometry and operating parameters are given in Table 11.1.

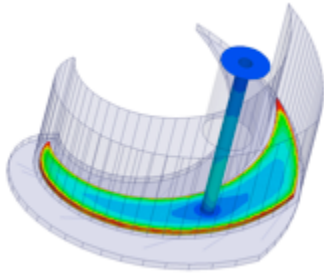
Table 11.1 System geometry and operating parameters

Liner Inner Radius	2.2 cm
Liner Outer Radius	45.24 cm
Dee Inner Radius	4.5 cm
Dee Outer Radius	43.75 cm
Pole-to-Pole Angle	45 degrees
Valley Depth from MP	30 cm
Dee surface to MP	1.25 cm
Dee Plate Thickness	1 cm
Dee to liner minimum gap	1 cm
Number of Turns	2000 turns
Fundamental Frequency	66.99 MHz
Spiral Equation	$\Theta = r/18$, r in cm
Max Energy	250 MeV/u
Effective Transit Time Gap	3.5 cm = $1.0 + 2 \times 1.25$
Gap Transit Time Factor (TT)	$\approx 0.99 = \sin(\Phi)/\Phi$
Dee Effective Transit Angle (ψ)	43.00 degrees
Dee acceleration factor	$0.726 = 2 \times TT \times \sin(\psi/2)$
Acceleration Factor per Turn	$1.451 = 2 \times 0.726$
Dee Peak Voltage	86.15 KV = $(250,000/2000)/(1.451)$
Amplitude Regulation	0.5 % RMS
Phase Regulation	0.5 Degrees RMS

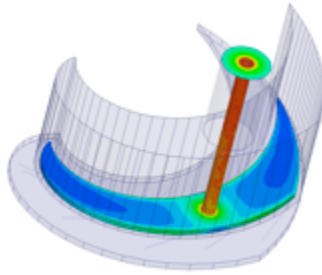
11.3 RF Resonator Electromagnetic Design

The RF resonator is analyzed using Ansoft HFSS software. Models are based on the MIT defined spiral equation. A classic single stem design is compared against a flat-topping design. The stem(s) radial position(s) are chosen to balance the voltage distribution along the Dee.

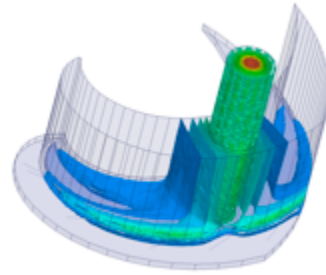
11.3.1 HFSS Single Stem Case



Surface E Field



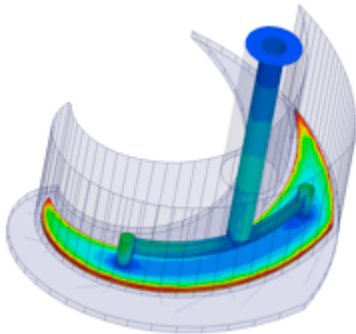
Surface H Field



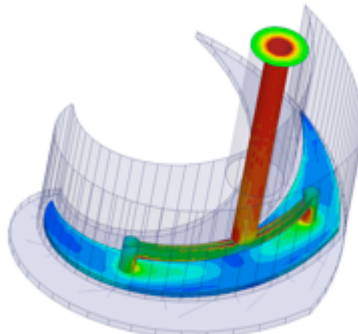
Volume H Field

Results	Operating Values	Mechanical
F = 69.3 MHz	Tip Peak Voltage = 100 KV	Valley Depth = 20 cm
Qu = 3120	Driver Power = 65.9 KW	Stem Radial Position = 31 cm
	Stem Current = 1478 Arms	Stem Length = 16.5 cm

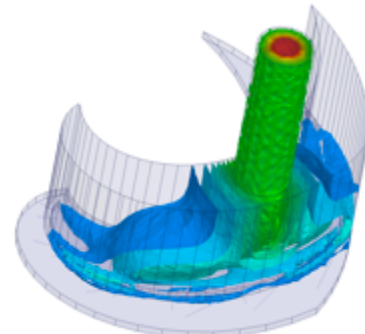
11.3.2 HFSS “Flat-Top” Case



Surface E Field



Surface H Field



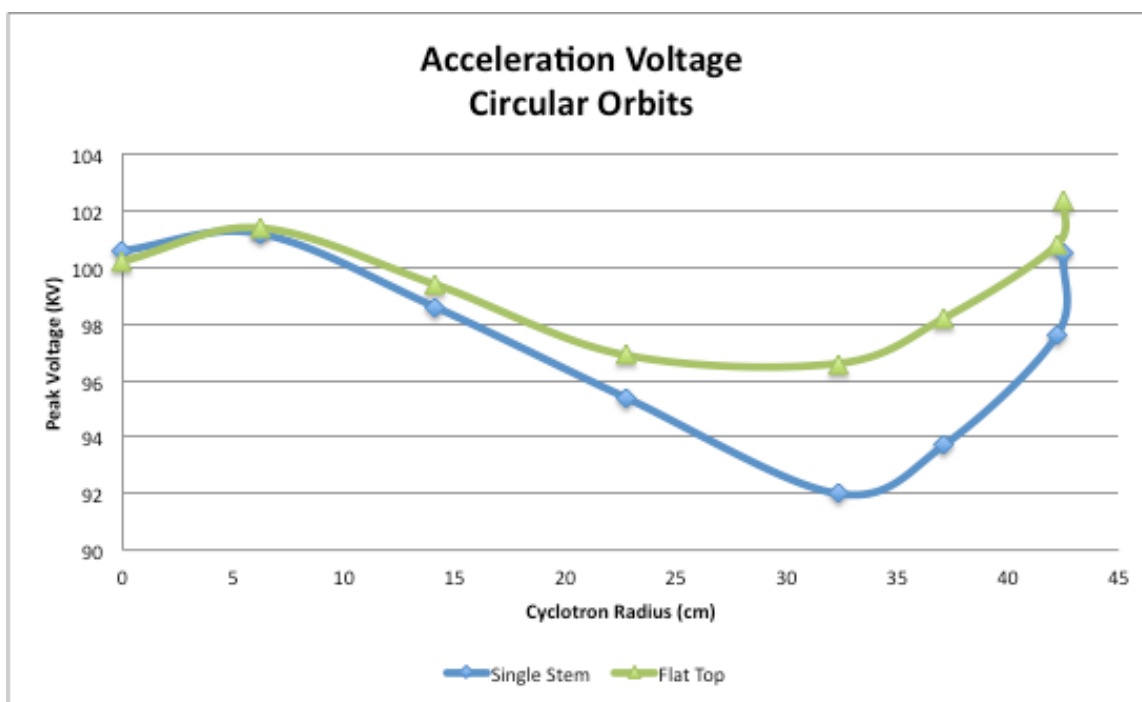
Volume H Field

Results	Operating Values	Mechanical
F = 66.9 MHz	Tip Peak Voltage = 100 KV	Valley Depth = 20 cm
Qu = 2799	Driver Power = 87.1 KW	Stem Radial Position = 30.5 cm
	Stem Current = 1710 Arms	Stem Length = 27 cm

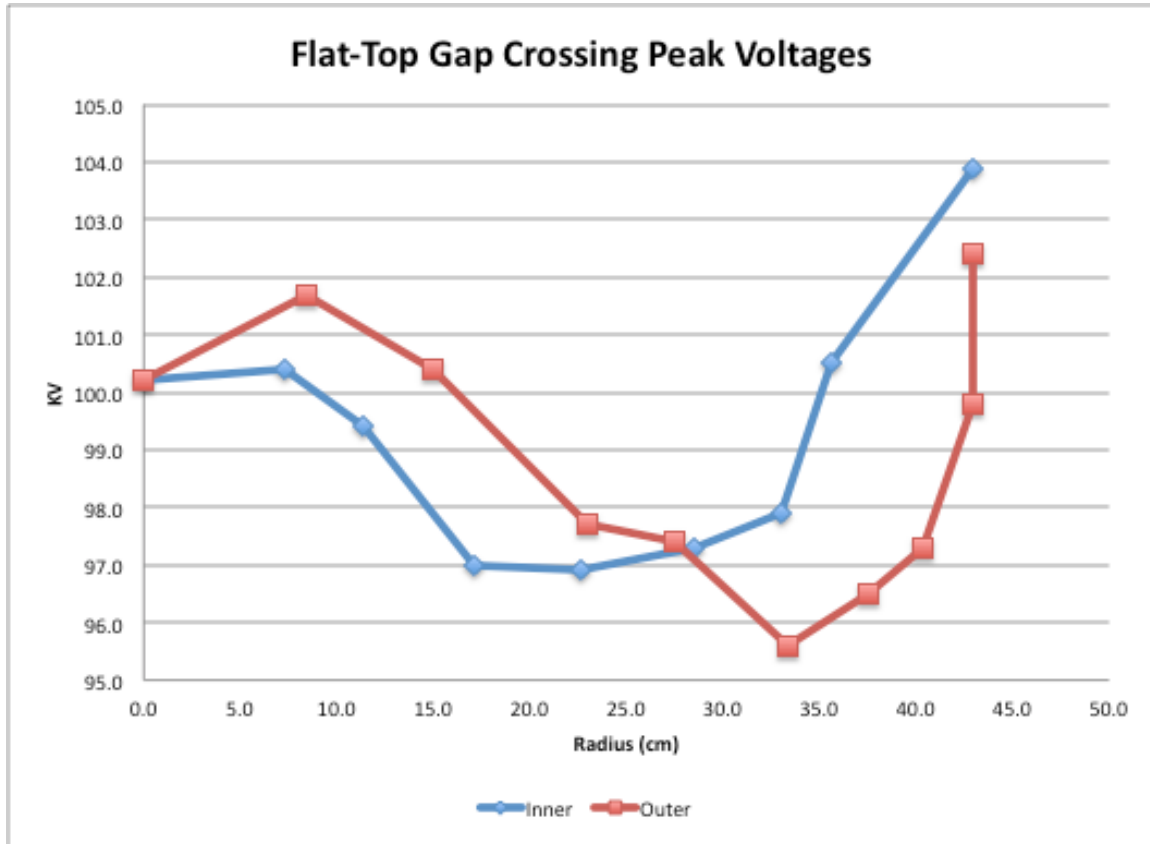
Table 11.2 Resulting Resonator Parameters

	Single Stem	Flat Top
HFSS		
Qu	3120	2799
Wc (KW)	66.0	87.1
Vc (KV) peak at Dee Tip	100.6	100.2
f _{oc} (MHz)	69.3	66.9
Stem Current (Amperes RMS)	1478	1710
Specs		
WB (KW)	125	125
Model (at Dee Tip)		
Q _L	1560	1400
f _c = (2πf _{oc})/2Q _L (KHz)	140	150.2
R _e (KΩ)	19.7	16.8
IDrive (Amperes Peak)	7.6	8.5
IBeam (Amperes Peak)	2.5	2.5

11.3.3 Resonator Voltage Distribution



11.3.4 Resonator Voltage Distribution



11.3.5 Resonator Plans

- Final resonator model will be analyzed following detailed mechanical design.
 - Dee and Stem design.
 - Input Coupler and Fine Tuner.
 - HFSS model updated with the actual mechanical design to finalize design details – such as stem length.
- Since the stem current is too high to allow a sliding short with fingers, a design and manufacturing method must be found to allow setting the center frequency experimentally with the tuner in a fixed specified location.

11.4 RF System Stability Modeling and Analysis

11.4.1 System Modeling Introduction

A linear resonant RF cavity behaves exactly as a resonant RLC circuit within its bandwidth about resonance.

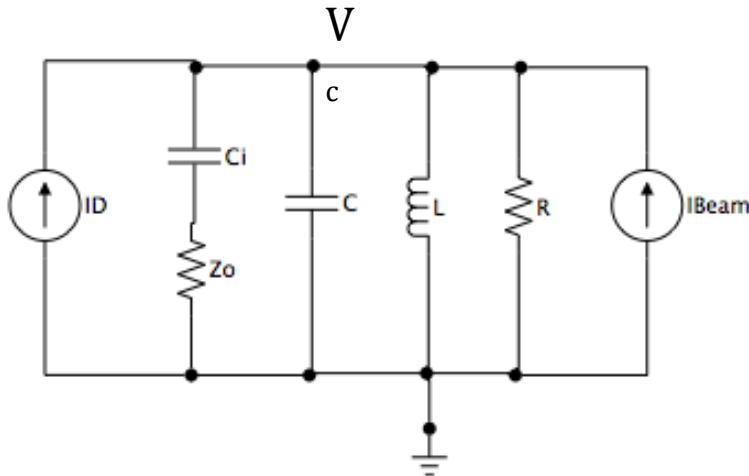
The equivalent circuit will be designed to match the resonator parameters as if measured at the cyclotron center.

A systems model of the circuit is derived in the frequency domain using Laplace transform techniques.

The model is designed for the “loaded Q” condition without beam loading.

Beam loading is modeled as a disturbance input.

11.4.2 System Modeling – Dee Cavity 1



Plant: Resonator Equivalent Circuit

Circuit Elements

R, L, and C represent a cyclotron resonator

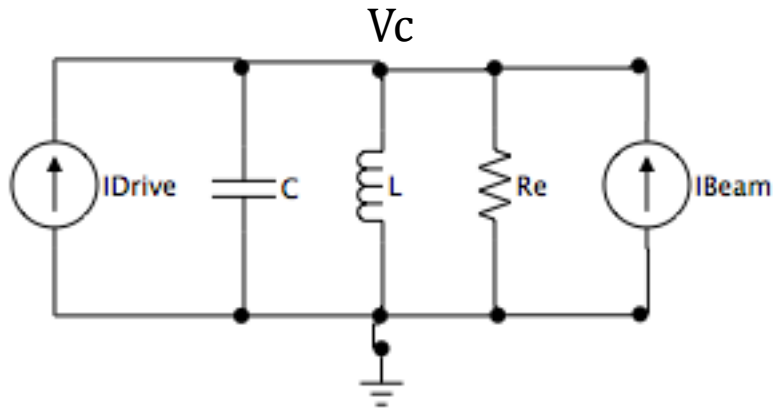
Ci, and Zo represent the input coupler and 50 Ohm line.

ID represents the effective drive current phasor

Ibeam represents the effective beam current phasor

11.4.3 System Modeling – Dee Cavity 2

The previous model may be simplified to:



The coupling circuit is designed to “match” a 50 Ohm feed-line to the cavity at full voltage and beam power.

The coupling circuit causes $Q_L = \frac{1}{2}Q_u$ at full beam power

HFSS calculates the:

Q_u : Unloaded Q

W_c : Cavity losses at V_c

U : Stored energy at V_c

ω_{oc} : Resonant Frequency

Other parameters include:

W_B : Beam Power

W_i : Coupler Load

Q_L : Loaded Q

11.4.4 System Modeling – Dee Cavity 3

The circuit is designed to respond accurately to two inputs I_{drive} and I_{beam} . This requires R_e be chosen as:

$$R_e = \frac{V_c^2}{2(2W_c + W_B)}$$

The rest of the elements are chosen as normal:

$$C = \frac{2W_c Q_u}{\omega_{oc} V_c^2}$$

$$L = \frac{1}{\omega_{oc}^2 C}$$

$$I_{Beam} = \frac{2W_B}{V_c} \angle 180^\circ$$

$$I_{Drive} = \frac{4(W_c + W_B)}{V_c} \angle 0^\circ$$

Note: I_{drive} is twice the actual value to account for the loaded Q being $\frac{1}{2}$ the cavity Q. This is an anomaly of the model needed to get the proper dynamic response. The actual drive requirement is $\frac{1}{2}$ of this value. Current and voltage values are peak sinusoidal values. (power = $\frac{1}{2} v \cdot i$)

11.4.5 System Modeling – Dee Cavity 4

Transfer Function = Plant Impedance

$$\frac{V_c}{I} = Z = \frac{\frac{1}{C}s}{s^2 + \frac{1}{R_e C}s + \frac{1}{LC}}$$

This equation is recast as:

$$\frac{V_c}{I} = Z = \frac{\frac{\omega_{oc} R_e}{Q_L} s}{s^2 + \frac{\omega_{oc}}{Q_L} s + \omega_{oc}^2}$$

11.4.6 System Modeling – Dee Cavity 5

We seek the “envelope response” for amplitude and phase at modulation frequencies $\ll \omega_0$, in other words within the cavity bandwidth $\Delta\omega = Q_L/\omega_0$

Determine $Z(s + j\omega)$ to remove the RF frequency and noting once the RF frequency is removed $s \ll \omega_0$ and the small bandwidth causes $\omega_0 \cong \omega$. After much manipulation this yields:

$$Z(s + j\omega) \approx \frac{R_e \frac{\omega_{oc}}{2Q_L}}{s - j(\omega_{oc} - \omega) + \frac{\omega_{oc}}{2Q_L}}$$

The quantity $(\omega_0 - \omega)$ in the above expression is referred to as “The Detuning Frequency” in the accelerator community and expresses the amount the cavity is being driven off resonance. Notice when this term is 0, the above expression becomes a simple first order transfer function.

11.4.7 System Modeling – Dee Cavity 6

Defining $V_c = V_I + jV_Q$, $I_{drive} = I_I + jI_Q$ and recasting $Z(s + j\omega)$ as V_c/I_{drive} then converting back into the time domain and separating into real and imaginary parts yields the MIMO system:

$$\begin{bmatrix} \frac{d}{dt} V_I \\ \frac{d}{dt} V_Q \end{bmatrix} = \begin{bmatrix} -\frac{\omega_{oc}}{2Q_L} & -(\omega_{oc} - \omega) \\ (\omega_{oc} - \omega) & -\frac{\omega_{oc}}{2Q_L} \end{bmatrix} \begin{bmatrix} V_I \\ V_Q \end{bmatrix} + \begin{bmatrix} R \frac{\omega_{oc}}{2Q_L} \\ R \frac{\omega_{oc}}{2Q_L} \end{bmatrix} \begin{bmatrix} I_I \\ I_Q \end{bmatrix}$$

Notice when the detuning frequency is 0, the equations are totally decoupled.

The RF amplitude and phase are:

$$|V_c| = \sqrt{V_I^2 + V_Q^2}$$

$$\phi = \tan^{-1} \left(\frac{V_Q}{V_I} \right)$$

11.4.8 System Modeling – Transfer Function 1

Previously it has been shown that the I and Q signals are decoupled when the cavity is driven at the resonant frequency and that these signals are first order ($n = 1$). The amplifier string adds an additional pole ($n = 1 + 1 = 2$).

The response of these loops will be designed and analyzed for both the PID and ADRC type control.

I and Q, eventually leading to “amplitude” and “phase” control, will be separate control loops with ADRC treating the particular dynamics and coupling between them as unspecified dynamics to be observed and dealt with in real time.

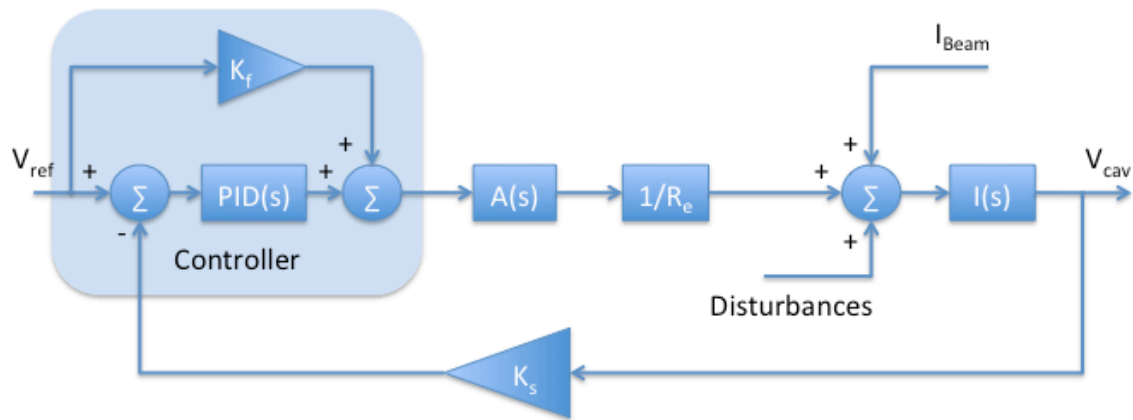
11.4.9 System Modeling – Transfer Function 2

$$I(s) = \frac{R_e \frac{\Delta\omega}{2}}{s + \frac{\Delta\omega}{2}} \equiv \frac{R_e \omega_c}{s + \omega_c}, \quad A(s) \equiv \frac{K_v \omega_a}{s + \omega_a}$$

$$G(s) = I(s)A(s) = \frac{R_e K_v \omega_c \omega_a}{s^2 + (\omega_c + \omega_a)s + \omega_c \omega_a} \equiv \frac{b_0}{s^2 + (\omega_c + \omega_a)s + \omega_0^2}$$

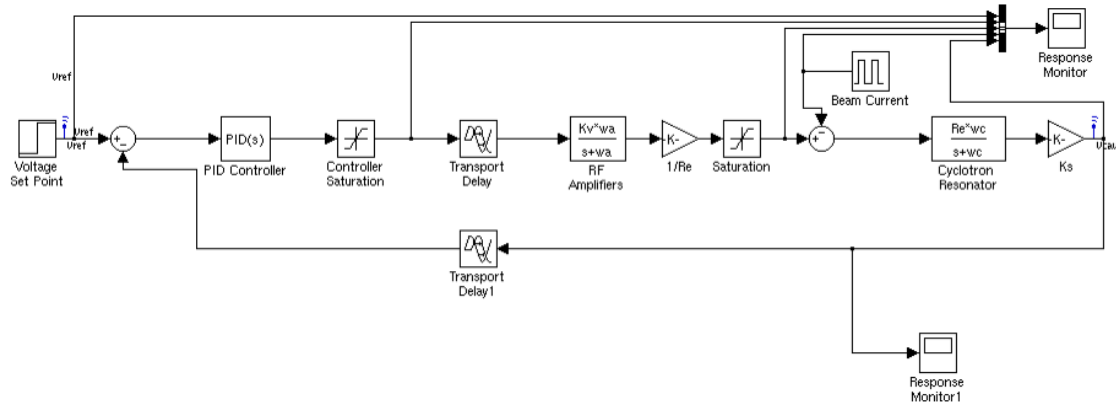
$$y'' + (\omega_c + \omega_a)y' + \omega_0^2 y = b_0 u_o$$

11.4.10 System Modeling – PID



V_{ref} : Cavity Setpoint
 K_f : Feed-Forward Gain
 K_s : Sensor Gain
 $PID(s)$: Control TF
 $A(s)$: Amplifier TF
 $I(s)$: Dee Cavity TF

11.4.11 System Modeling – Simulink PID

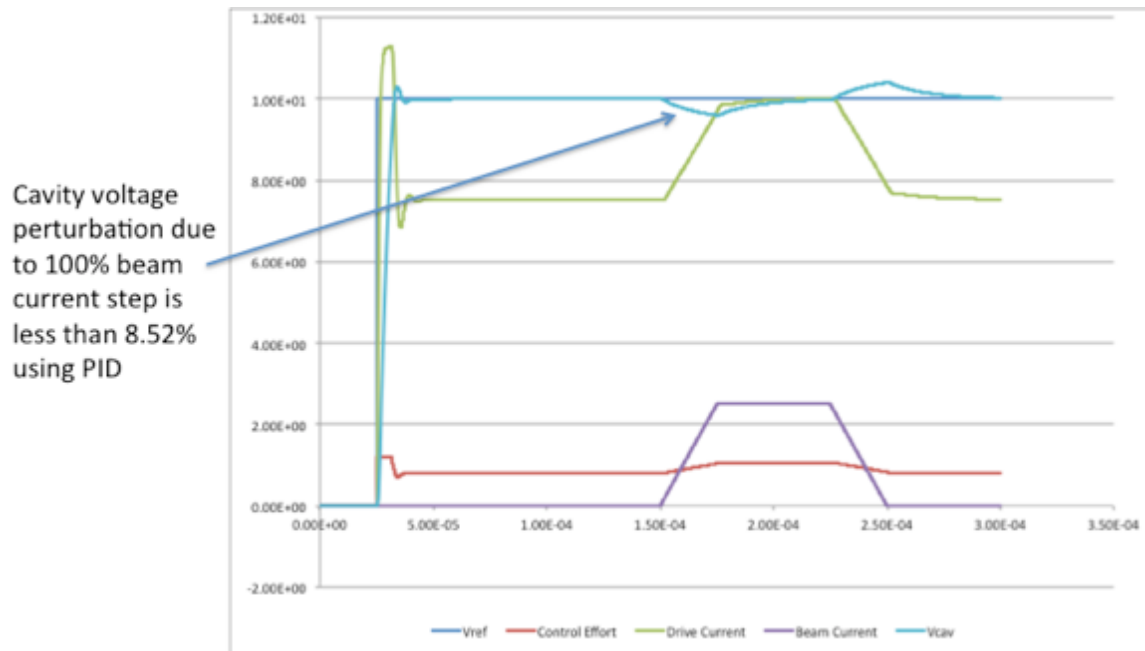


The K_v gain transforms 10V from the controller to 125KV.

The $1/R_e$ gain transforms the 100KV voltage into the effective drive current.

The “Saturation” blocks clamp the control efforts and current to the real world equivalents.

11.4.12 System Modeling – PID Response



11.4.13 ADRC – Active Disturbance Rejection Control

ADRC is now introduced, applied, simulated, and compared to the PID results.

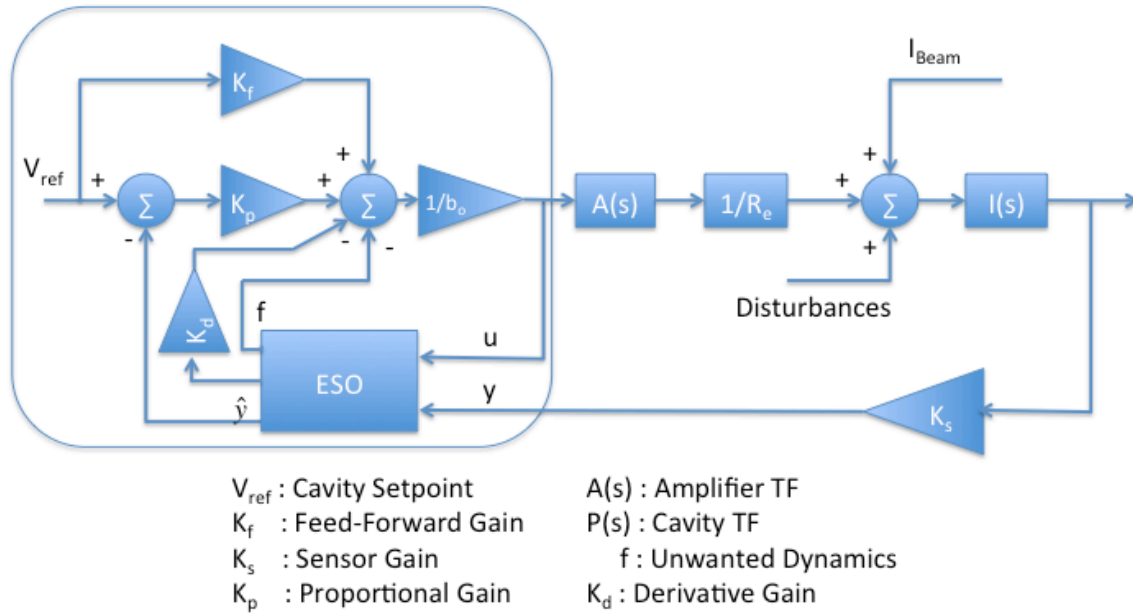
John Vincent, et. al, “On active disturbance rejection based control design for superconducting RF cavities” Nuclear Instruments and Methods in Physics Research, A , 643: 1, pp. 11-16, 2011.

Basic ADRC Premise: ADRC creates an additional state to the system that captures the unknown dynamics, non-stationary dynamics, or disturbances consistent with the system order.

The additional state increases the order of the original system by 1 to $n + 1$.

The additional state is created through the application of an “Extended State Observer” (ESO) that separates the desired dynamics from the undesired signals and outputs them separately.

11.4.14 ADRC Block Diagram



11.4.15 ARDC 3rd Order ESO

$$z' = Az + Bu + L(y - \hat{y}), \quad \hat{y} = Cz = z_1, \quad z_3 \equiv f$$

$$L \equiv \begin{bmatrix} \beta_1 \\ \beta_2 \\ \beta_3 \end{bmatrix}, \quad C = \begin{bmatrix} 1 \\ 0 \\ 0 \end{bmatrix}$$

$$\begin{bmatrix} z'_1 \\ z'_2 \\ z'_3 \end{bmatrix} = \begin{bmatrix} -\beta_1 & 1 & 0 \\ -\beta_2 & 0 & 1 \\ -\beta_3 & 0 & 0 \end{bmatrix} \begin{bmatrix} z_1 \\ z_2 \\ z_3 \end{bmatrix} + \begin{bmatrix} \beta_1 & 0 \\ \beta_2 & b_o \\ \beta_3 & 0 \end{bmatrix} \begin{bmatrix} y \\ u \end{bmatrix}$$

$$A = \begin{bmatrix} -\beta_1 & 1 & 0 \\ -\beta_2 & 0 & 1 \\ -\beta_3 & 0 & 0 \end{bmatrix}, \quad B = \begin{bmatrix} \beta_1 & 0 \\ \beta_2 & b_o \\ \beta_3 & 0 \end{bmatrix}$$

11.4.16 ADRC Mechanics - 2

Desired Eigenvalues:

$$(\lambda + \omega_o)^3 = \lambda^3 + 3\omega_o\lambda^2 + 3\omega_o^2\lambda + \omega_o^3 = 0$$

ESO Eigenvalues:

$$|I\lambda - A| = \begin{vmatrix} \lambda + \beta_1 & -1 & 0 \\ \beta_2 & \lambda & -1 \\ \beta_3 & 0 & \lambda \end{vmatrix} = \lambda^3 + \beta_1\lambda^2 + \beta_2\lambda + \beta_3 = 0$$

$$\therefore \beta_1 = 3\omega_o, \beta_2 = 3\omega_o^2, \beta_3 = \omega_o^3$$

$\omega_o \rightarrow$ Desired ESO bandwidth

11.4.17ADRC Mechanics - 3

Final ESO:

$$\begin{bmatrix} z_1' \\ z_2' \\ z_3' \end{bmatrix} = \begin{bmatrix} -3\omega_o & 1 & 0 \\ -3\omega_o^2 & 0 & 1 \\ -\omega_o^3 & 0 & 0 \end{bmatrix} \begin{bmatrix} z_1 \\ z_2 \\ z_3 \end{bmatrix} + \begin{bmatrix} 3\omega_o & 0 \\ 3\omega_o^2 & b_o \\ \omega_o^3 & 0 \end{bmatrix} \begin{bmatrix} y \\ u \end{bmatrix}$$

$$\hat{y} = z_1 = \hat{V}_{cav}, z_3 \equiv f$$

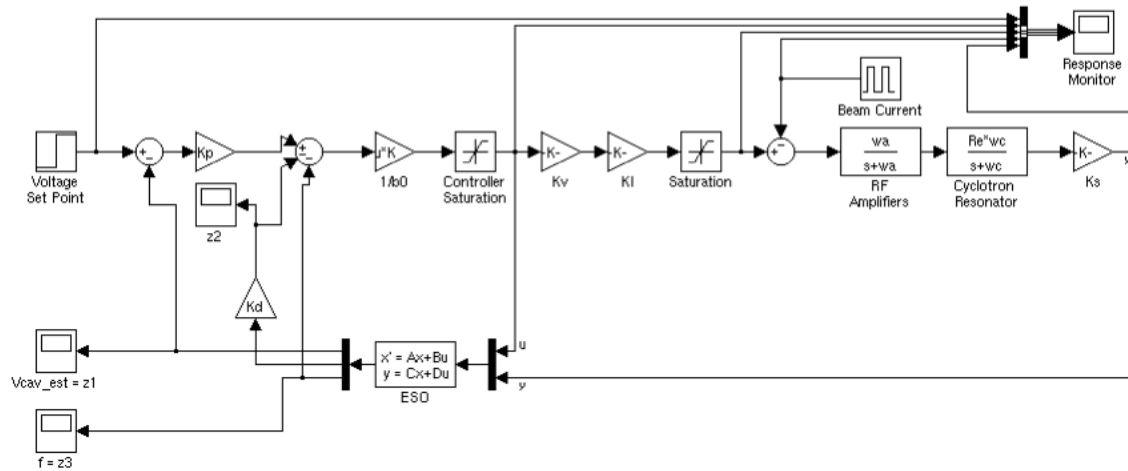
Control Design:

$$u \equiv \frac{u_o - z_3}{b_o} \Rightarrow y'' = V_{cav}'' = b_o \left[\frac{u_o - f}{b_o} \right] + f = u_o$$

$$u_o \equiv K_p (V_{ref} - \hat{V}_{cav}) - K_d (\hat{V}_{cav}') \quad (11.4.17)$$

$$\therefore V_{cav}'' = K_p (V_{ref} - \hat{V}_{cav}) - K_d (\hat{V}_{cav}')$$

11.4.18 System Modeling – Simulink ADRC

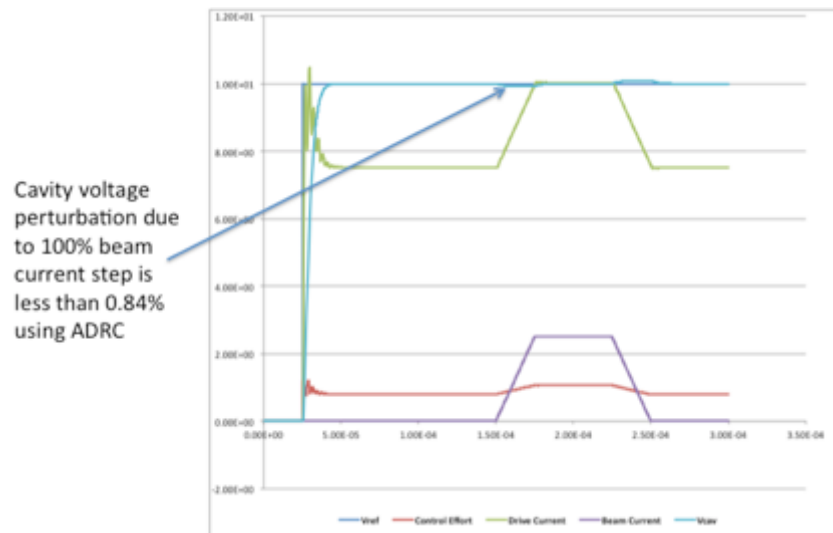


The Kv gain transforms 10V from the controller to 125KV.

The 1/Re gain transforms the 100KV voltage into the effective drive current.

The “Saturation” blocks clamp the control efforts and current to the real world equivalents.

11.4.19 Third Order ADRC Simulation



11.4.20 System Modeling & Control Summary

The cyclotron RF system was modeled and two control strategies were evaluated: PID and ADRC. The results make ADRC the clear choice.



11.5 Necessary Technology

RF Amplifiers and Controls

250KW RF Amplifier parts package delivered to MIT for fabrication.

RF Controls & Instrumentation to be fabricated in Phase 2B by MSU.

Components list delivered to MIT and substantially procured.

MIT to Mechanically Design

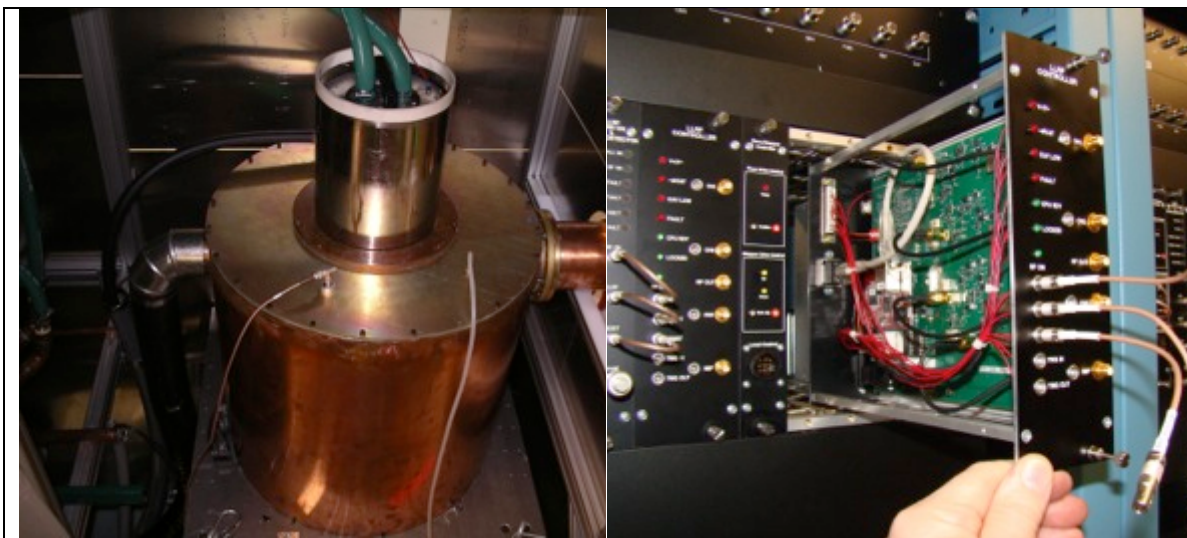
Cyclotron Resonators

RF Input Couplers & Drives

RF Tuners & Drives

Issues to be addressed by MSU

Reflected power & tuning



11.6 Estimated Cost

A cost estimate was made for the system components including equipment, materials, and labor as given in Table 11.2. Many of these components have either been procured or on order as reported to PSU in a separate, final cost report.

Table 11.3 Estimated costs of RF system components

Description	Qty	Cost Each			Cost Total		
		Materials (\$)	Engineering (hrs)	Trades (hrs)	Materials (\$)	Engineering (hrs)	Trades (hrs)
RF Support & Management	2.5	\$3,000	925	925	\$7,500	2313	2313
RF Controls & Instrumentation							
LLRF System	2	\$15,097	24	94	\$30,193	48	187
RF Clock	1	\$8,886	23	25	\$8,886	23	25
RF Amplifiers							
Driver Amplifier	2	\$75,850	80	80	\$151,700	160	160
Final Amplifier	2	\$779,600	1134	2119	\$1,559,200	2267	4238
Cyclotron Components							
Resonator	2	\$25,000	925	1850	\$50,000	1850	3700
Coupler	2	\$15,000	240	160	\$30,000	480	320
Trimmer	2	\$5,000	160	160	\$10,000	320	320
Recommended Spares							
50KW DC Module	2	\$55,000	2	2	\$110,000	4	4
2KW Amplifier Module	2	\$8,000			\$16,000	0	0
LLRF Module	2	\$12,564	23	87	\$25,128	47	174
Total					\$1,998,607	7512	11441
with Contingency					\$2,500,000	9000	13500

11.7 RF Summary Summary

The total RF System cost including materials and labor is expected to be less than \$5M. With regard to the RF amplifier and controls, the amplifier design is complete and may be procured, fabricated, and assembled by MIT. Suitable control strategies have been

designed and the electronics may be procured, fabricated, assembled and programmed by MSU in phase 2b. A manual will be prepared by MSU in Phase 2b. The cyclotron resonators, couplers, and trimmers require mechanical design and detailing by MIT.

12.0 Evolution of Proton Bunches in HI Cyclotrons: a Preliminary Study

12.1 Introduction

In this task, we focus on understanding the evolution of proton bunches in isochronous cyclotrons in a regime sometimes referred to as the “high-intensity regime”. This is a regime in which the bunch density is so high that electrostatic space-charge forces cannot be neglected, and modify the dynamics of the bunch as calculated from single-particle theories.

12.2 Geometrical effects

The approach that we follow here can be qualified as “bottom-up”. Specifically, we do not start by constructing a very complicated numerical solver, which would account for all the geometrical intricacies of an isochronous cyclotron, but perhaps not yield many insights. Instead, we choose to build our physical intuition of the physical processes at stake little by little. In the first stage of our analysis, we will therefore ignore all the possible complications arising from the cyclotron geometry: we will study the evolution of the proton bunch in a classical cyclotron.

In fact, in the preliminary stage which we describe below, we will do even simpler than that. We will assume that the cyclotron magnetic field is homogeneous in space, and study space-charge and temperature effects on a proton bunch which is drifting in this homogeneous magnetic field. We will see that this extremely simple case already yields some very interesting insights. The next steps, not described in this report, will be to add the accelerating gaps, then the spatial variations of the magnetic field, etc.

12.3 Physical models for the evolution of the proton bunch

Beside the complications due to the geometry of the cyclotron, there also are several possible levels of complication for the equations used to describe the evolution of the bunch.

12.3.1 A. Kinetic description

Ideally, we would solve for the phase-space distribution function of the proton bunch, $f(\vec{r}, \vec{v}, t)$, such that $f(\vec{r}, \vec{v}, t) d\vec{r} d\vec{v}$ is the number of proton particles near point \vec{r} , having velocity \vec{v} , at time t . Indeed, if we found a way to compute f for any time, at any place, and for any velocity, we would then exactly know all the bunch physical quantities that could be of interest. For instance, the density of the bunch at any point in time and any point in space is

$$n(\vec{r}, t) \equiv \int f(\vec{r}, \vec{v}, t) d\vec{v}$$

the flow velocity is

$$\vec{V}(\vec{r}, t) \equiv \frac{1}{n(\vec{r}, t)} \int f(\vec{r}, \vec{v}, t) \vec{v} d\vec{v}$$

and the pressure is

$$\vec{p} \equiv m \int f(\vec{v} - \vec{V})(\vec{v} - \vec{V}) d\vec{v}$$

In the absence of Coulomb collisions between the protons (usually a good assumption for bunches in cyclotrons), and assuming that relativistic effects can be neglected, the equation for the distribution function is

$$\frac{\partial f}{\partial t} + \vec{v} \cdot \nabla f + \frac{e}{m} (\vec{E} + \vec{v} \times \vec{B}) \cdot \nabla_{\vec{v}} f = 0 \quad (0.1)$$

This equation can be seen as a consequence of Liouville's theorem. It simply states that the proton distribution function must be constant along the particle trajectories, given by

$$\frac{d\vec{r}}{dt} = \vec{v}; \quad \frac{d\vec{v}}{dt} = \vec{a} = \frac{e}{m} (\vec{E} + \vec{v} \times \vec{B})$$

Eq.(0.1) looks deceptively simple, and one may be tempted to think that it can be solved easily. The reason it is not so is three-folds:

1. The unknown function f depends on 7 independent variables: 3 for space, 3 for the velocities, and 1 for time
2. The equation is nonlinear. Indeed, as f changes in time, the electric field \vec{E} and the magnetic field \vec{B} also evolve, since the charge density and the electric current density are given by

$$\rho(\vec{r}, t) = e \int f(\vec{r}, \vec{v}, t) d\vec{v} \quad \vec{J}(\vec{r}, t) = e \int f(\vec{r}, \vec{v}, t) \vec{v} d\vec{v}$$

3. The equation describes processes occurring over very different length scales (e.g. the typical length scale of the bunch vs. the radius of the bunch orbit) and time scales (e.g. the cyclotron frequency vs. the slow time scale associated with the expansion of the bunch due to space-charge effects)

The bottom line is that a kinetic treatment quickly becomes fairly involved, and computationally intensive. Still, in many cases, it cannot be avoided. For example, beam phase-space instabilities, or viscosity effects can only be treated properly if one uses a kinetic description of the proton bunch. In the future, we are therefore very likely to use such a kinetic description to develop a proper theory for the MEGATRON. For this

preliminary stage however, we will use a simplified fluid treatment of the proton bunch to get our first insights into space-charge and temperature effects.

12.3.2 Fluid description

By taking moments of the kinetic equation, *exact* fluid equations can be derived. For example, by integrating the kinetic equation over all velocities, we have:

$$\frac{\partial n}{\partial t} + \nabla \cdot (n \vec{V}) = 0 \quad \text{conservation of mass} \quad (0.2)$$

where n and \vec{V} , the density and the flow velocity, have been defined above. Multiplying the kinetic equation by \vec{v} and integrating over all velocities, we have

$$mn \left(\frac{\partial \vec{V}}{\partial t} + \vec{V} \cdot \nabla \vec{V} \right) + \nabla \cdot \vec{p} = en (\vec{E} + \vec{V} \times \vec{B}) \quad \text{conservation of momentum} \quad (0.3)$$

where \vec{p} has been defined previously.

With these two equations, a well-known problem associated with taking moments of the kinetic equation becomes apparent. It is often called the *closure problem*, and can be explained as follows.

Eq.(0.2) is an equation for the density n , but we also need to know the flow velocity \vec{V} to solve it. Eq.(0.3) is such an equation for \vec{V} (also involving n), but we need to know the pressure tensor \vec{p} to solve it (provided \vec{E} and \vec{B} are known through Maxwell's equations, which we did not write here). To determine \vec{p} , we would thus need to take a higher moment of the kinetic equation, and obtain a fluid-like equation for this tensor. Unfortunately, such an equation would also involve another new unknown physical quantity, sometimes called the stress flux tensor, for which we would need a new equation as well. There is clearly no end to this infinite process.

In other words, the closure problem is the somewhat discouraging observation that each exact fluid moment depends on the next higher moment.

There are several strategies to avoid this fundamental obstacle. One of them is to treat the problem fully kinetically, i.e. to solve the kinetic equation (Eq.(0.1)), with all the advantages and disadvantages described in the previous section.

Another strategy is *truncation*. The idea is to assume more or less arbitrarily (depending on the level of accuracy that one desires) that since high-order moments of the kinetic equation carry information which only leads to slight modifications of the quantities defined in the low-order moment equations (typically density, velocity, and pressure), they are negligible. The moments that are kept in the

analysis and considered as relevant depend on the level of accuracy that one desires for the calculation.

In the present case, we will only retain the first two moments of the kinetic equation, Eq.(0.2) and Eq.(0.3). To close the system of equations, we will assume that the pressure tensor \vec{p} is isotropic, so that $\vec{p} = p\vec{I}$ and $\nabla \cdot \vec{p} = \nabla p$. Furthermore, we will assume that the pressure of the bunch behaves in the same way as the pressure of an ideal monoatomic gas, so that

$$\frac{\partial p}{\partial t} + \vec{V} \cdot \nabla p + \gamma p \nabla \cdot \vec{V} = 0 \quad \text{with } \gamma = \frac{5}{3} \quad (0.4)$$

Note that with this approximation, Equations (0.2), (0.3) and (0.4) form a set of 5 equations for 5 unknowns, so the problem is now well-posed, and we can try to solve it.

In several types of plasmas, the assumptions that the pressure tensor is isotropic and that the scalar pressure evolves as in Eq.(0.4) are not valid. This is in particular the case for the non-neutral plasma of interest in our case: with the beam parameters of the proton bunch in the MEGATRON and the magnitude of the electromagnetic fields, the two assumptions used to write Eq.(0.4) cannot be rigorously justified. This is the reason why a kinetic treatment of the problem will probably be necessary in later stages of this project.

Still, Eq.(0.4) remains an reasonable choice for this preliminary study, for the following reasons:

- It is simple
- We are mostly interested in space-charge effects, and in the proton bunch, forces associated with space-charge effects dominate forces associated with temperature effects, with a ratio of about 4 to 1 (see Section II below)
- At zero temperature ($p=0$), Eq.(0.2) and Eq.(0.3) are *exact*, i.e. they would take exactly the same form in a fully kinetic treatment of the problem
- As we will show in section III.3.B, when the pressure tensor is assumed to be isotropic the exact details of Eq.(0.4) do not have any effect on the evolution of the bunch density. They only matter for the evolution of the pressure itself

12.3.3 Electromagnetic fields

We will initially ignore relativistic effects. Therefore, the self-electric field due to the proton charges is very well approximated by an electrostatic electric field, determined by solving Poisson's equation:

$$\vec{E} = -\nabla \phi \quad \nabla^2 \phi = -\frac{en}{\epsilon_0}$$

If we ignore relativistic effects, then we can also ignore the self-magnetic field of the moving proton bunch, and consider that the magnetic force on the bunch is purely that of the known externally applied magnetic field.

12.4 Summary

In summary, in this preliminary study we will study the evolution of a proton bunch drifting in a homogeneous externally applied magnetic field \vec{B} , and subject to space-charge and temperature effects. In the lab frame, the fluid equations describing this evolution self-consistently are the following:

$$\begin{aligned}
 \frac{\partial n}{\partial t} + \nabla \cdot (n \vec{V}) &= 0 \\
 mn \left(\frac{\partial \vec{V}}{\partial t} + \vec{V} \cdot \nabla \vec{V} \right) &= en \left(-\nabla \phi + \vec{V} \times \vec{B} \right) - \nabla p \\
 \frac{\partial p}{\partial t} + \vec{V} \cdot \nabla p + \gamma p \nabla \cdot \vec{V} &= 0 \\
 \nabla^2 \phi &= -\frac{en}{\epsilon_0}
 \end{aligned} \tag{0.5}$$

12.5 Starting fluid equations: Non-dimensional equations in moving frame

From Eq.(0.5), one can easily derive the following set of normalized equations, describing the bunch as a warm fluid in the frame rotating at the cyclotron frequency:

$$\begin{aligned}
 \frac{dn}{dt} + n \nabla \cdot \vec{v} &= 0 \\
 \frac{d\vec{v}}{dt} + \vec{v} \times \vec{e}_z &= -\epsilon^2 \left(\nabla \phi + \frac{\alpha^2}{n} \nabla p \right) \\
 \frac{dp}{dt} + \gamma p \nabla \cdot \vec{v} &= 0 \\
 \nabla^2 \phi &= -n
 \end{aligned} \tag{0.6}$$

The following quantities are involved in Eq.(0.6):

$$\begin{aligned}
 \frac{d}{dt} &= \frac{\partial}{\partial t} + \vec{v} \cdot \vec{\nabla} & t &= \Omega t' \\
 \vec{r} &= \frac{\vec{r}'}{a} & \nabla &= a \nabla' \\
 \vec{v} &= \frac{\vec{v}'}{a\Omega} & n &= \frac{n'}{N_0} \\
 p &= \frac{p'}{N_0 T_0} & \phi &= \frac{\epsilon_0}{e N_0 a^2} \phi' \\
 \epsilon^2 &= \frac{\omega_p^2}{\Omega_c^2} & \omega_p^2 &= \frac{N_0 e^2}{m \epsilon_0} \\
 \alpha^2 &= \frac{T_0}{m a^2 \omega_p^2} = \frac{\lambda_D^2}{a^2}
 \end{aligned} \tag{0.7}$$

a is the characteristic size of the proton bunch (its radius if the bunch is spherical), N_0 the peak density of the bunch, and T_0 its peak temperature. For the MEGATRON parameters, \tilde{U}^2 is a very small number: $\tilde{U}^2 \approx 0.0028$. We also have $a^2 \approx 0.23$. All the ' quantities correspond to the "real" physical quantities, i.e. the quantities measured in the lab units, but in the moving frame, which was defined by the following transformation:

$$\begin{aligned}
 r' &= \bar{r} & \theta' &= \bar{\theta} + \Omega t \\
 z' &= \bar{z} & t' &= \bar{t} \\
 v_r' &= \bar{v}_r & v_\theta' &= \bar{v}_\theta + r\Omega \\
 v_z' &= \bar{v}_z & n' &= \bar{n} \\
 p' &= \bar{p} & \phi' &= \bar{\phi}
 \end{aligned} \tag{0.8}$$

In Eq.(0.8), we have introduced the natural cylindrical coordinates associated with the cyclotron geometry: the z -direction is along the magnetic field, r is the radial coordinate in the plane perpendicular to the magnetic field, and θ the angle coordinate in that plane. All the quantities with the symbol $\bar{}$ over them refer to quantities measured in the (non-moving) lab frame.

12.6 Ideal focusing model

For this analysis, as a first step, we will work with a model which can be described as the *ideal focusing model*. It assumes that there is a perfect focusing force parallel to the magnetic field, which is in the z direction. Consequently, for all times, we

have $v_z(\vec{r}, t) = 0$. This assumption simplifies the analysis, and is partly justified by the fact that cyclotron engineers usually do not encounter any difficulties in focusing the bunch in the vertical direction. If in the future experimental evidence shows that there in fact is a strong coupling between the vertical beam dynamics and the dynamics in the plane perpendicular to the magnetic field, we may have to get rid of this assumption, and consider the motion of the bunch in the z direction.

12.7 Asymptotic analysis: Asymptotic expansion

Given the difference in the time scale associated with the betatron oscillation and that associated with the expansion of the beam due to electrostatic and thermal forces, we perform an asymptotic analysis of the equations (0.6). The asymptotic expansion is carried out by means of a multiple time scale expansion. Each quantity Q is assumed to vary according to the different time scales as follows:

$$Q(\vec{r}, t) = Q(\vec{r}, t_0, t_2, t_4, \dots) = Q(\vec{r}, t, \varepsilon^2 t, \varepsilon^4 t, \dots) \quad (0.9)$$

With this formal expansion, we have

$$\frac{\partial Q}{\partial t} = \frac{\partial Q}{\partial t_0} + \varepsilon^2 \frac{\partial Q}{\partial t_2} + \dots \quad (0.10)$$

It is convenient for the rest of the calculation to separate the quantities Q into the sum of a rapidly oscillating part \tilde{Q} varying due to the betatron oscillations, and a slow monotonic evolution \bar{Q} due space charge and thermal effects:

$$Q(\vec{r}, t_0, t_2, \dots) = \tilde{Q}(\vec{r}, t_0, t_2, \dots) + \bar{Q}(\vec{r}, t_2, \dots) \quad (0.11)$$

Now, under the assumption that the betatron oscillations are small in amplitude, the appropriate expansion for the relevant physical quantities is the following:

$$\begin{aligned} n &= \bar{n}_0 + \varepsilon(\tilde{n}_1 + \bar{n}_1) + \varepsilon^2(\tilde{n}_2 + \bar{n}_2) + O(\varepsilon^3) \\ p &= \bar{p}_0 + \varepsilon(\tilde{p}_1 + \bar{p}_1) + \varepsilon^2(\tilde{p}_2 + \bar{p}_2) + O(\varepsilon^3) \\ \phi &= \bar{\phi}_0 + \varepsilon(\tilde{\phi}_1 + \bar{\phi}_1) + \varepsilon^2(\tilde{\phi}_2 + \bar{\phi}_2) + O(\varepsilon^3) \\ \vec{v} &= \varepsilon\tilde{v}_1 + \varepsilon^2(\tilde{v}_2 + \bar{v}_2) + \varepsilon^3(\tilde{v}_3 + \bar{v}_3) + O(\varepsilon^4) \end{aligned} \quad (0.12)$$

12.8 Asymptotic analysis

We now introduce this expansion in the set of equations given by Eq.(0.6), and solve order by order in ε . We start with Poisson's equation. To lowest order, we have

$$\nabla^2 \bar{\phi}_0 = -\bar{n}_0 \quad (0.13)$$

As we will later see, this is all we need to know from Poisson's equation.

We now turn to the continuity equation. The first non-trivial equation comes to first order in U , and we have

$$\frac{\partial \tilde{n}_1}{\partial t_0} + \nabla \cdot (\bar{n}_0 \tilde{\mathbf{v}}_1) = 0 \quad (0.14)$$

This equation describes the evolution of the density on the fast time scale, due to the betatron oscillations. To next order, the mass conservation equation takes the form:

$$\frac{\partial \tilde{n}_2}{\partial t_0} + \frac{\partial \bar{n}_0}{\partial t_2} + \nabla \cdot \left[(\tilde{n}_1 + \bar{n}_1) \tilde{\mathbf{v}}_1 + \bar{n}_0 (\tilde{\mathbf{v}}_2 + \bar{\mathbf{v}}_2) \right] = 0 \quad (0.15)$$

Averaging this equation over the fast time scale, we get, because of the periodicity of the % quantities in t_0 :

$$\frac{\partial \bar{n}_0}{\partial t_2} + \nabla \cdot (\langle \tilde{n}_1 \tilde{\mathbf{v}}_1 \rangle + \bar{n}_0 \bar{\mathbf{v}}_2) = 0 \quad (0.16)$$

where we have introduced the notation

$$\langle Q \rangle = \frac{1}{2\pi} \int_0^{2\pi} Q dt_0$$

Eq.(0.16) describes the evolution of the bunch density on the slow time scale. This is where the influence of the electrostatic effects and the beam temperature will come in, and this is therefore all we need from the continuity equation.

In a very similar way, we obtain the following equations for the evolution of the pressure, to order U and \tilde{U} :

$$\frac{\partial \tilde{p}_1}{\partial t_0} + \tilde{\mathbf{v}}_1 \cdot \nabla \bar{p}_0 + \gamma \bar{p}_0 \nabla \cdot \tilde{\mathbf{v}}_1 = 0 \quad (0.17)$$

$$\frac{\partial \bar{p}_0}{\partial t_2} + \langle \tilde{\mathbf{v}}_1 \cdot \nabla \tilde{p}_1 \rangle + \bar{\mathbf{v}}_2 \cdot \nabla \bar{p}_0 + \gamma \bar{p}_0 \nabla \cdot \bar{\mathbf{v}}_2 + \gamma \langle \tilde{p}_1 \nabla \cdot \tilde{\mathbf{v}}_1 \rangle = 0 \quad (0.18)$$

This is all we need from the energy equation. We finally look at the momentum equation. The first equation that is not trivially satisfied is of order U :

$$\frac{\partial \tilde{\mathbf{v}}_1}{\partial t_0} + \tilde{\mathbf{v}}_1 \times \bar{\mathbf{e}}_z = \vec{0} \quad (0.19)$$

This is the expected equation determining the velocity of the betatron oscillations. To next order, we have

$$\frac{\partial \tilde{\vec{v}}_2}{\partial t_0} + \tilde{\vec{v}}_1 \cdot \nabla \tilde{\vec{v}}_1 + (\tilde{\vec{v}}_2 + \tilde{\vec{v}}_2) \times \vec{e}_z = -\nabla \bar{\phi}_0 - \frac{\alpha^2}{\bar{n}_0} \nabla \bar{p}_0 \quad (0.20)$$

In the same way as it was done before, we can now average over the fast time scale, to find

$$\bar{\vec{v}}_2 = \langle \tilde{\vec{v}}_1 \cdot \nabla \tilde{\vec{v}}_1 \rangle \times \vec{e}_z + \nabla \bar{\phi}_0 \times \vec{e}_z + \frac{\alpha^2}{\bar{n}_0} \nabla \bar{p}_0 \times \vec{e}_z \quad (0.21)$$

At this point, all the relevant equations have been derived. Indeed, Eq.(0.13), Eq.(0.14), Eq.(0.16), Eq.(0.17), Eq.(0.18), Eq.(0.19), and Eq.(0.21) form a set of 9 equations for the 9 unknowns \bar{f}_0 , \bar{n}_0 , \bar{n}_1 , \bar{p}_0 , \bar{p}_1 , $\bar{\vec{v}}_1$ and $\bar{\vec{v}}_2$.

12.9 Solving the equations

We now solve the set of 9 equations derived previously. The calculation can be decomposed in two parts: 1) a first part corresponding to the description of the betatron oscillations to lowest order, and their effect on the bunch pressure and the bunch density; 2) a second part describing the combined influence of the betatron oscillations and the electrostatic and temperature effects on the slow time scale evolution of the bunch density and bunch pressure.

12.9.1 The betatron oscillations

The subset of equations describing betatron oscillations to lowest order are repeated below for convenience:

$$\begin{aligned} \frac{\partial \tilde{\vec{v}}_1}{\partial t_0} + \tilde{\vec{v}}_1 \times \vec{e}_z &= \vec{0} \\ \frac{\partial \tilde{n}_1}{\partial t_0} + \nabla \cdot (\bar{n}_0 \tilde{\vec{v}}_1) &= 0 \\ \frac{\partial \tilde{p}_1}{\partial t_0} + \tilde{\vec{v}}_1 \cdot \nabla \bar{p}_0 + \gamma \bar{p}_0 \nabla \cdot \tilde{\vec{v}}_1 &= 0 \end{aligned} \quad (0.22)$$

The first equation in (0.22) is the equation of a particle immersed in a uniform magnetic field. It is easily solved:

$$\tilde{\vec{v}}_1(\vec{r}, t_0, t_2, \dots) = \vec{u}_1 \cos t_0 + \vec{e}_z \times \vec{u}_1 \sin t_0 \quad (0.23)$$

where $\vec{u}_1(\vec{r}, t_2, \dots)$ is the “initial” betatron velocity, i.e. $\tilde{\vec{v}}_1$ at time t_0 . The initial density and pressure are given by

$$\begin{aligned}\tilde{n}_1 &= \tilde{N}_1(\vec{r}) - \tilde{\xi}_1 \cdot \nabla \bar{n}_0 - \bar{n}_0 \nabla \cdot \tilde{\xi}_1 \\ \tilde{p}_1 &= \tilde{P}_1(\vec{r}) - \tilde{\xi}_1 \cdot \nabla \bar{p}_0 - \gamma \bar{p}_0 \nabla \cdot \tilde{\xi}_1\end{aligned}$$

The second and third equations in (0.22) are most easily solved by introducing the displacement vector $\tilde{\xi}_1(\vec{r}, t_0, t_2, \dots)$ associated with the betatron oscillations, defined by

$$\tilde{\vec{v}}_1 = \frac{\partial \tilde{\xi}_1}{\partial t_0}; \quad \tilde{\xi}_1(\vec{r}, t_0 = 0, t_2, \dots) = \vec{0} \quad (0.24)$$

Indeed, the second equation in (0.22) then takes the form:

$$\frac{\partial}{\partial t_0} \left[\tilde{n}_1 + \nabla \cdot (\bar{n}_0 \tilde{\xi}_1) \right] = 0 \quad (0.25)$$

and the third equation in (0.22) is

$$\frac{\partial}{\partial t_0} \left(\tilde{p}_1 + \tilde{\xi}_1 \cdot \nabla \bar{p}_0 + \gamma \bar{p}_0 \nabla \cdot \tilde{\xi}_1 \right) = 0 \quad (0.26)$$

These two equations can be solved immediately:

$$\begin{aligned}\tilde{n}_1 &= \tilde{N}_1(\vec{r}) - \tilde{\xi}_1 \cdot \nabla \bar{n}_0 - \bar{n}_0 \nabla \cdot \tilde{\xi}_1 \\ \tilde{p}_1 &= \tilde{P}_1(\vec{r}) - \tilde{\xi}_1 \cdot \nabla \bar{p}_0 - \gamma \bar{p}_0 \nabla \cdot \tilde{\xi}_1\end{aligned} \quad (0.27)$$

where \tilde{N}_1 and \tilde{P}_1 are the initial density and pressure of the bunch at time $t_0 = 0$. $\tilde{\xi}_1$ is just as easily calculated, by integrating Eq.(0.24) using (0.23). We find

$$\tilde{\xi}_1 = \vec{u}_1 \sin t_0 + \vec{u}_1 \times \vec{e}_z (\cos t_0 - 1) = (\tilde{\vec{v}}_1 - \vec{u}_1) \times \vec{e}_z \quad (0.28)$$

We thus showed how to calculate $\tilde{\vec{v}}_1$, \tilde{n}_1 and \tilde{p}_1 . Since we now know \tilde{n}_1 , we could also compute $\tilde{\phi}_1$, through Poisson's equation, $\nabla^2 \tilde{\phi}_1 = -\tilde{n}_1$, and we would therefore know all the physical quantities associated with the betatron motion to lowest order.

As we will see in the next section, it turns out that $\tilde{\phi}_1$ is not necessary to determine what we are really interested in: the slow time scale evolution of the lowest order

density \bar{n}_0 and lowest order pressure \bar{p}_0 due to space-charge and temperature effects.

12.9.2 The slow time scale evolution

In this section we use the results derived in the previous section, describing the betatron motion to lowest order, to determine the equations that we will have to solve to determine the evolution of the bunch density and pressure on the slow time scale.

We start with the time-averaged (over the fast time scale) density equation, Eq.(0.16), repeated here for convenience:

$$\frac{\partial \bar{n}_0}{\partial t_2} + \nabla \cdot (\langle \tilde{n}_1 \tilde{v}_1 \rangle + \bar{n}_0 \bar{v}_2) = 0$$

where \bar{v}_2 was given by Eq.(0.21):

$$\bar{v}_2 = \langle \tilde{v}_1 \cdot \nabla \tilde{v}_1 \rangle \times \bar{e}_z + \nabla \bar{\phi}_0 \times \bar{e}_z + \frac{\alpha^2}{\bar{n}_0} \nabla \bar{p}_0 \times \bar{e}_z$$

Using the results derived previously, we find

$$\langle \tilde{n}_1 \tilde{v}_1 \rangle = \frac{1}{2} \left[\nabla \cdot (\bar{n}_0 \bar{u}_1) \bar{u}_1 \times \bar{e}_z - \nabla \cdot (\bar{n}_0 \bar{u}_1 \times \bar{e}_z) \bar{u}_1 \right] \quad (0.29)$$

and

$$\langle \tilde{v}_1 \cdot \nabla \tilde{v}_1 \rangle \times \bar{e}_z = \frac{1}{2} \left[\bar{u}_1 \cdot \nabla \bar{u}_1 + (\bar{e}_z \times \bar{u}_1) \cdot \nabla (\bar{e}_z \times \bar{u}_1) \right] \times \bar{e}_z \quad (0.30)$$

Combining Eq.(0.29) and Eq.(0.30), we find:

$$\langle \tilde{n}_1 \tilde{v}_1 \rangle + \bar{n}_0 \langle \tilde{v}_1 \cdot \nabla \tilde{v}_1 \rangle \times \bar{e}_z = \frac{1}{2} \nabla \times (\bar{n}_0 \bar{u}_1^2 \bar{e}_z) \quad (0.31)$$

This is a very nice result: it shows that when we order the betatron oscillations as small (they only come to first order in our expansion), they do not play any role in the slow time evolution of the bunch! Indeed, the divergence of a curl is always zero, so Eq.(0.16) can now be written

$$\begin{aligned} \frac{\partial \bar{n}_0}{\partial t_2} + \nabla \cdot (\bar{n}_0 \nabla \bar{\phi}_0 \times \bar{e}_z) + \alpha^2 \nabla \cdot (\nabla \bar{p}_0 \times \bar{e}_z) &= 0 \\ \Leftrightarrow \frac{\partial \bar{n}_0}{\partial t_2} + \nabla \bar{\phi}_0 \times \bar{e}_z \cdot \nabla \bar{n}_0 &= 0 \end{aligned} \quad (0.32)$$

This is another interesting result. It shows that to lowest order, the slow time evolution of the bunch density is *not* influenced by temperature effects. This is a direct consequence of the choice we made for the pressure equation. By assuming that the pressure was isotropic, we reduced the divergence of the pressure tensor to the gradient of the scalar quantity \bar{p}_0 . And the term $\nabla \bar{p}_0 \times \vec{e}_z$ which appears in the density equation can be written as a curl, which is obviously divergence free.

The bottom line is that to determine the slow evolution of the bunch density, we only have to solve the following two coupled equations:

$$\begin{aligned} \frac{\partial \bar{n}_0}{\partial t_2} + \nabla \bar{\phi}_0 \times \vec{e}_z \cdot \nabla \bar{n}_0 &= 0 \\ \nabla^2 \bar{\phi}_0 &= -\bar{n}_0 \end{aligned} \quad (0.33)$$

Note that the slow time evolution of the bunch pressure can also be obtained by evaluating all the terms in Eq.(0.18), i.e. $\langle \tilde{v}_1 \cdot \nabla \tilde{p}_1 \rangle$, $\bar{v}_2 \cdot \nabla \bar{p}_0$, $\gamma \bar{p}_0 \nabla \cdot \bar{v}_2$, $\gamma \langle \tilde{p}_1 \nabla \cdot \tilde{v}_1 \rangle$, using the expressions given in Eqs.(0.23), (0.27), and (0.28). After some straightforward but slightly tedious algebra, one finds:

$$\frac{\partial \bar{p}_0}{\partial t_2} + \left(\nabla \bar{\phi}_0 + \gamma \frac{p_0}{n_0^2} \alpha^2 \nabla \bar{n}_0 \right) \times \vec{e}_z \cdot \nabla \bar{p}_0 = 0 \quad (0.34)$$

In principle, after calculating the evolution of \bar{n}_0 and \bar{f}_0 for all time steps, we could evolve \bar{p}_0 using Eq.(0.34). However, the information we would get from doing this would be limited, and perhaps even misleading. Indeed, the energy equation we used for the closure of the fluid equations (the third equation in (0.6)) is hard to justify in the physical regime of interest.

12.10 Numerical results

In this section, we show the results we obtained when numerically solving the equations for the evolution of the bunch density on the slow time scale. For convenience, we repeat here these two equations:

$$\begin{aligned} \frac{\partial \bar{n}_0}{\partial t_2} + \nabla \bar{\phi}_0 \times \vec{e}_z \cdot \nabla \bar{n}_0 &= 0 \\ \nabla^2 \bar{\phi}_0 &= -\bar{n}_0 \end{aligned} \quad (0.35)$$

The first equation in Eq.(0.35) has a simple interpretation: it describes the convection of the density profile in the velocity field $\vec{E} \times \vec{B} / B^2$, the so-called $\vec{E} \times \vec{B}$ velocity (there is no - sign in front of $\nabla \bar{\phi}_0$ because the Lorentz force is in the opposite direction in the moving frame, see Eq.(0.6)).

This is not very surprising. In the absence of accelerating gaps, the effect of the betatron oscillations on the density profile averages out to zero on the slow time scale. Thus, the density profile simply follows the slow, averaged motion of the ions. In a homogeneous magnetic field, in the presence of an electric field created by the charges in the bunch themselves, this slow motion is just the $\vec{E} \times \vec{B}$ motion.

12.10.1 Numerical method

In order to solve Eq.(0.35) numerically, we first rewrite it in conservative form:

$$\begin{aligned} \frac{\partial \bar{n}_0}{\partial t_2} + \nabla \cdot (\bar{n}_0 \nabla \bar{\phi}_0 \times \vec{e}_z) &= 0 \\ \nabla^2 \bar{\phi}_0 &= -\bar{n}_0 \end{aligned} \tag{0.36}$$

The first equation in (0.36) is hyperbolic, and we integrate it using a scheme known as the *leap-frog method*, which has the advantage of being non-dissipative. At each time step, the density profile changes, so the electrostatic potential has to be recalculated. We use the integral form of Poisson's equation (second equation in Eq.(0.36)) to perform this task.

For the boundary conditions, we assume that at any time step, the density is exactly zero on all the edges of the computational domain.

Note that the integration of Poisson's equation is the step that is the most time consuming in the numerical procedure. In order to keep the computing time somewhat low, we have decided to assume that the beam is two-dimensional, and infinite in the z-direction. Since for our analysis we have already assumed that $v_z = 0$ at all times, this additional simplification should not significantly change the beam dynamics. And reducing the numerical integration from three dimensions to two dimensions represents a substantial gain in computing time.

Because the bunch is now considered to be infinite in the z-direction, a round bunch will be called *cylindrically symmetric*, as we will see in the next section.

12.10.2 Numerical results: Cylindrical bunch

If we start with a bunch density profile which is cylindrically symmetric, i.e. such that the bunch density is only a function of the distance from the center of the bunch ($\bar{n}_0 = \bar{n}_0(r)$), then the initial electrostatic potential due to the charges in the bunch will also be cylindrically symmetric: $\bar{\phi}_0 = \bar{\phi}_0(r)$. This implies that the initial electric field will be purely in the radial direction: $\vec{E} = E_r \vec{e}_r$. And the convective velocity $\nabla \bar{\phi}_0 \times \vec{e}_z$ will be purely in the azimuthal direction, i.e. in the \vec{e}_θ direction. We thus expect the density profile to rotate around the center of the bunch. Since this density profile is cylindrically symmetric, a rotation of the profile around the center will leave the profile invariant.

In other words, the space charge forces on a cylindrically symmetric bunch in a purely drifting region are such that the bunch properties are kept constant.

These predictions are confirmed by the numerical simulations. In Fig. 12.1, we see the initial profile of the normalized bunch density; in Fig. 12.2 it is the density profile after 100 revolutions; Figure 12.3 shows the profile after 500 revolutions, and Fig. 12.4 the profile after 1000 revolutions. It is clear that apart from the very small differences which are associated with the error due to the numerical leap-frog scheme, the bunch profiles are exactly identical in all four cases.

12.10.3 Numerical results: Elliptic bunch

The situation is different for an elliptic bunch, since the cylindrical symmetry is then broken. Nevertheless, the electric field far away from the bunch still has cylindrical symmetry (far away, the bunch is seen as a point charge). We thus expect the $\vec{E} \times \vec{B}$ convection to act in such a way as to make the bunch conform with this cylindrical symmetry. This is precisely what happens in the numerical simulation.

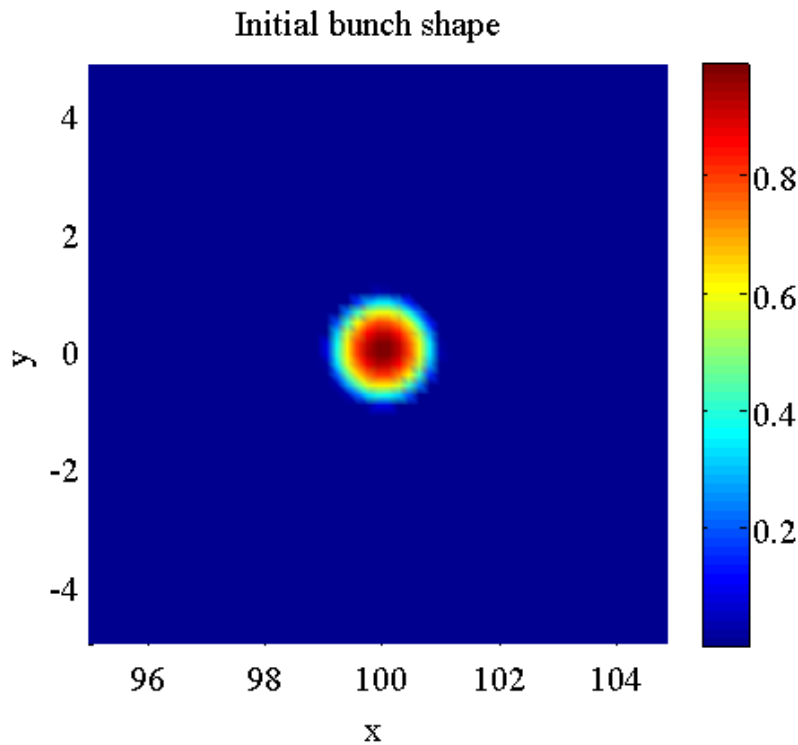


Fig. 12.1 Initial bunch density profile - cylindrically symmetric case

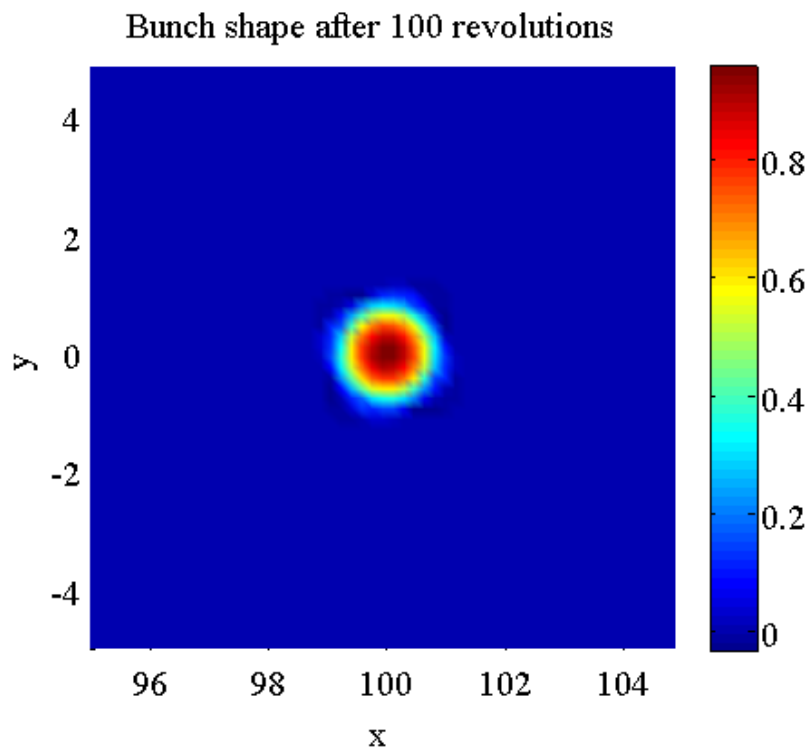


Fig. 12.2 Bunch density profile after 100 revolutions - cylindrically symmetric case

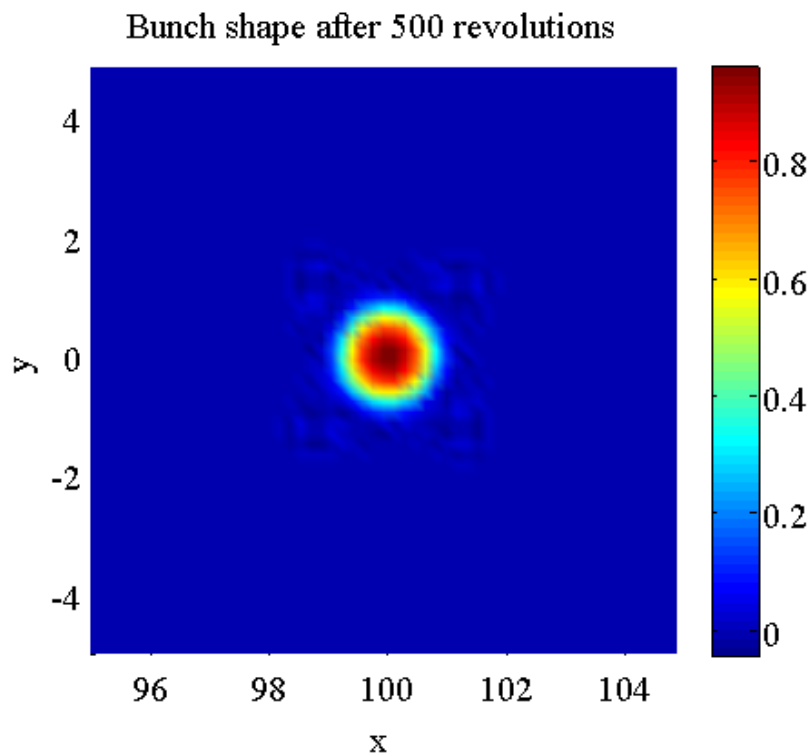


Fig. 12.3 Bunch density profile after 500 revolutions - cylindrically symmetric case

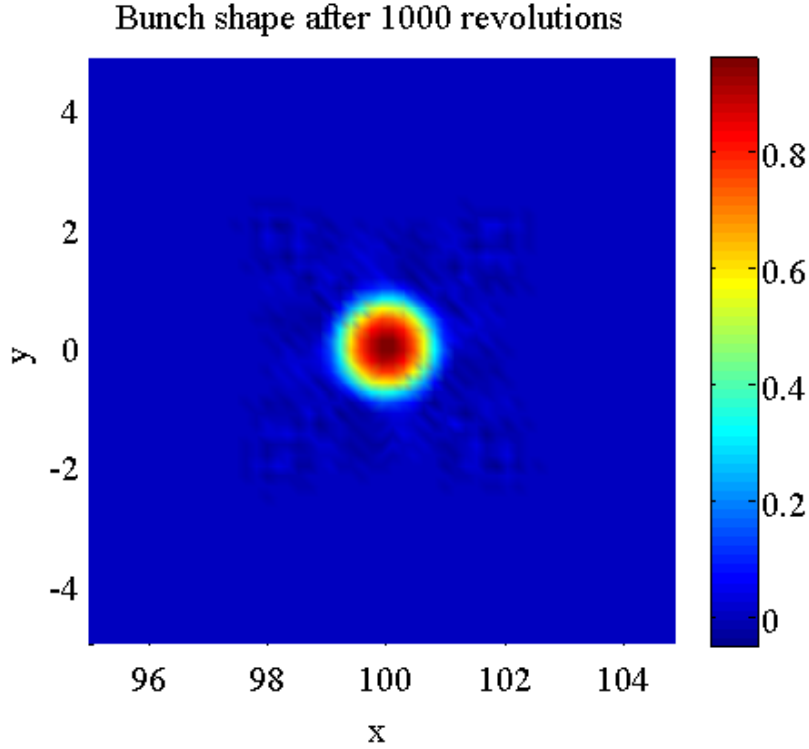


Fig. 12.4 Bunch density profile after 1000 revolutions - cylindrically symmetric case

We start with an elliptically shaped density profile, as shown in Fig. 12.5. The $\vec{E} \times \vec{B}$ convection then distorts and rotates the bunch, as we can see in Fig. 12.6 (snapshot taken after 100 cyclotron revolutions) and Fig. 7 (500 revolutions). After about 1000 revolutions, the bulk of the bunch has already reached a shape that is nearly cylindrically symmetric, and a small part of the bunch fills “galactic arms” (Fig. 12.8). These qualitative features are kept until the end of the simulations, so that after 2000 revolutions, the bulk of the bunch density profile is almost perfectly cylindrically symmetric, and the rest of the bunch is in the galactic arms which have extended further, and are closing on themselves (Fig. 12.9 and Fig. 12.10).

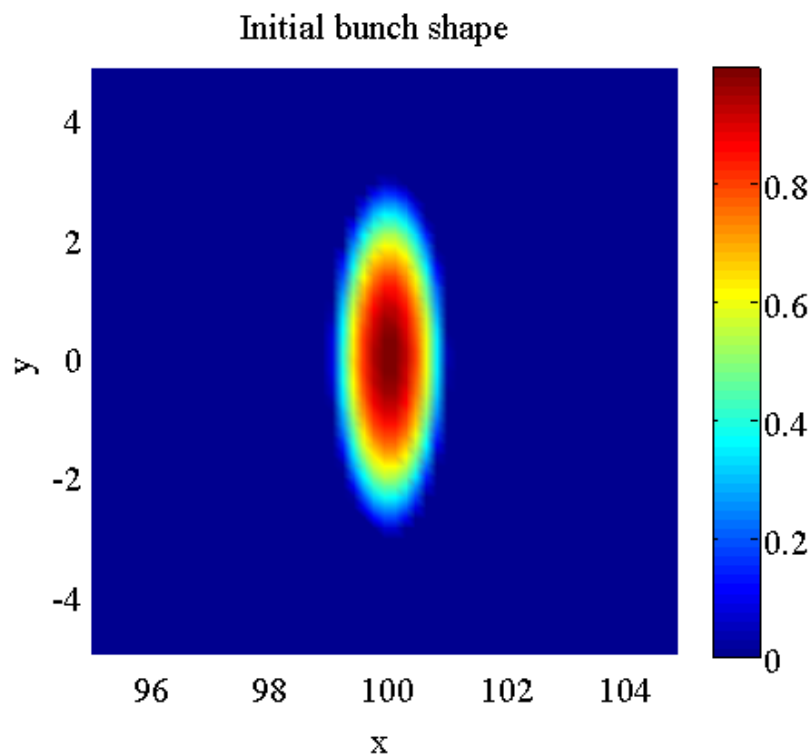


Fig. 12.5 Initial bunch density profile - Elliptic initial density profile

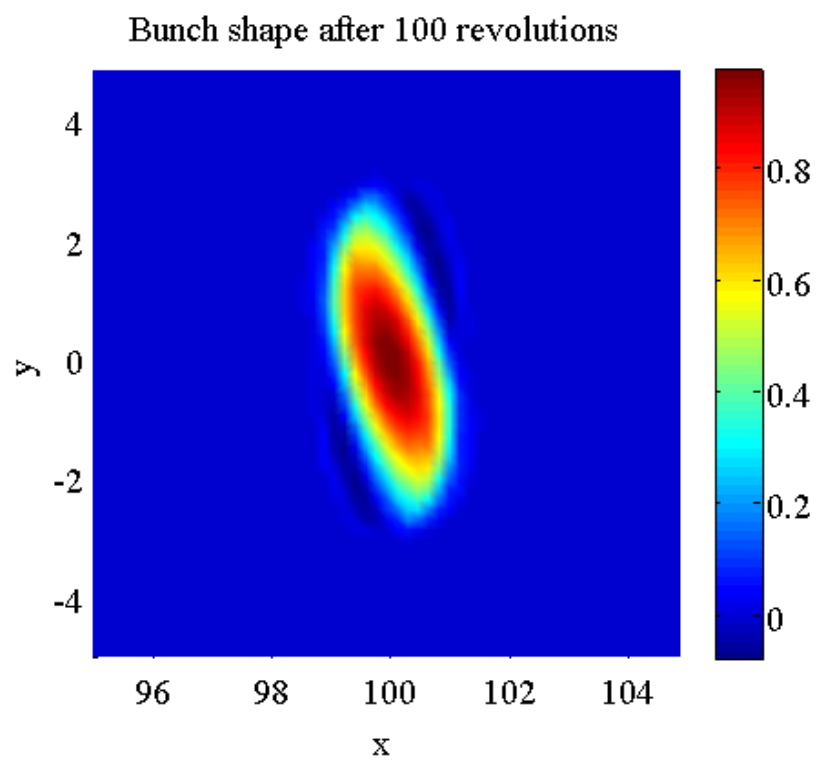


Fig. 12.6 Bunch density profile after 100 revolutions - Elliptic initial density profile

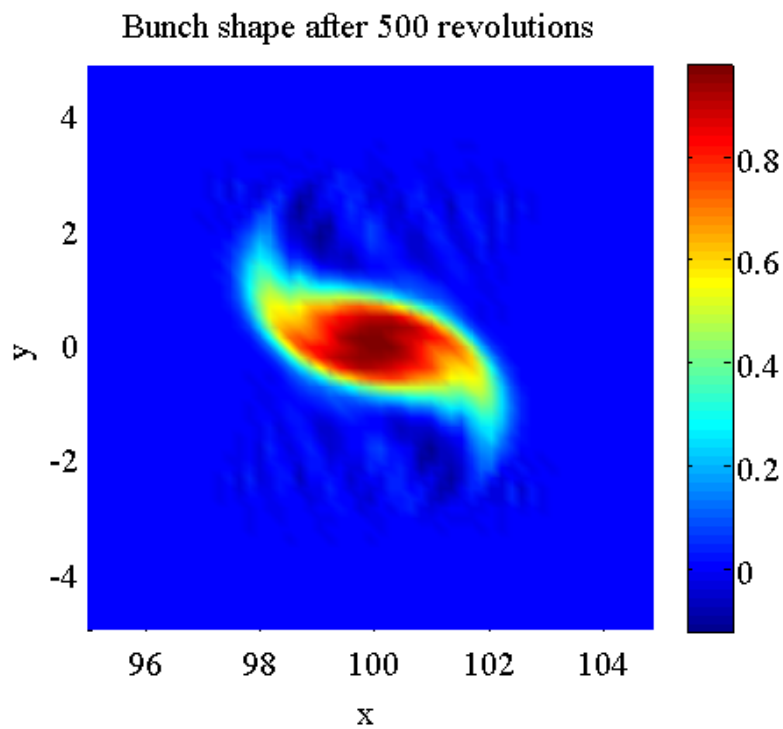


Fig. 12.7 Bunch density profile after 500 revolutions - Elliptic initial density profile

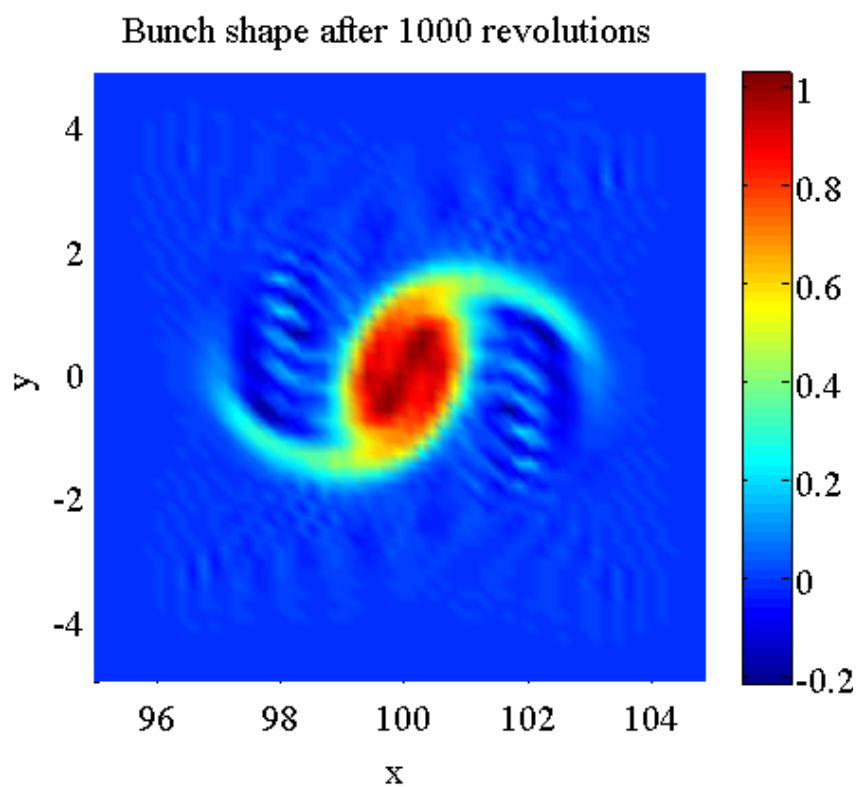


Fig. 12.8 Bunch density profile after 1000 revolutions - Elliptic initial density profile

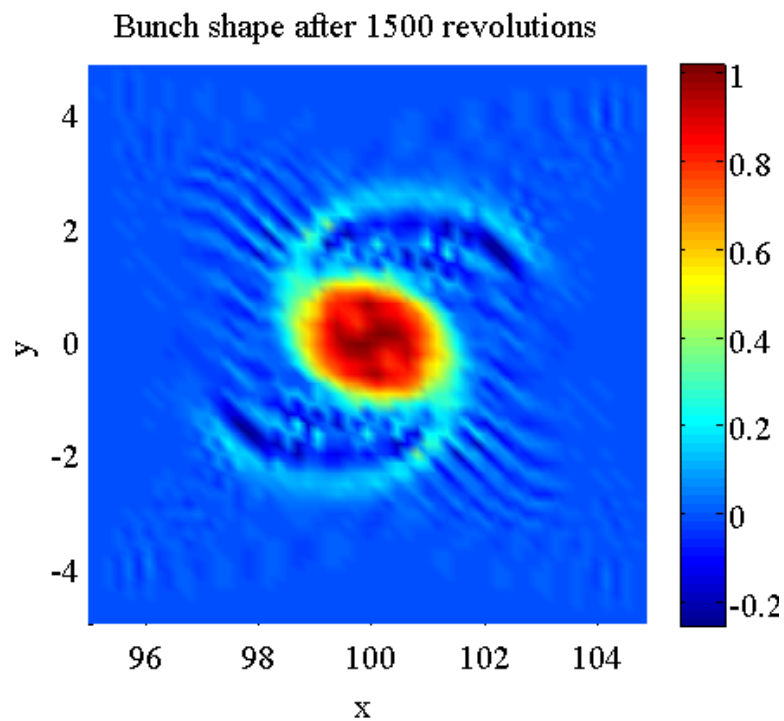


Fig. 12.9 Bunch density profile after 1500 revolutions - Elliptic initial density profile

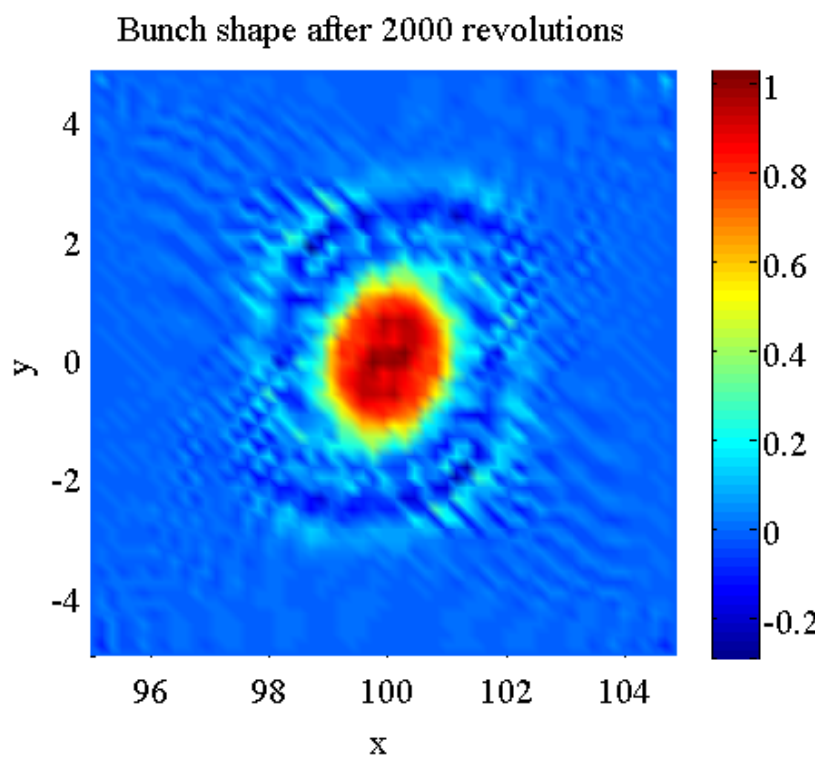


Fig. 12.10 Bunch density profile after 2000 revolutions - Elliptic initial density profile

12.11 Future plans

The simple 2D warm fluid model of a drifting bunch we considered here gave us some important insights on the role of space-charge forces in the drift sections of high beam intensity cyclotrons. Specifically, we have been able to highlight the fundamental role of the $\vec{E} \times \vec{B}$ convection in the deformation of the bunch.

Our goal is to extend this analysis to describe situations in better match with the MEGATRON experiment. Below, we describe the steps we will take towards that goal:

- Inclusion of the accelerating gaps
- Kinetic description of the bunch, in order to identify possible effects due to temperature anisotropies and phase-space instabilities
- Inclusion of the dynamics in the direction along the magnetic field
- Inclusion of the spatial dependence of the external magnetic field
- Inclusion of relativistic effects.

13.0 High Power Beam Dump System Final Design

13.1 Overview

The role of Raytheon IDS was to complete the design of a high-power beam dump target capable of safely stopping the proton beam produced by the Megatron system at full beam power of 250 kilowatts comprising 1 milliamperere of 250 MeV protons.

To support this effort, Raytheon provided neutronics and radiation analysis of the final beam dump design to support cooling requirement and materials selections. Additionally, mechanical design and analysis was to be performed culminating in a beam dump system description, model and manufacturing and test plan. Raytheon's scope also included support to the development of beam diagnostics and calorimetry for beam monitoring at full power when low-current intercepting diagnostics are impractical.

In the following sections, a technical report of the proposed target design and summary of progress through 10/31/2011 is included.

13.2 Beam dump design

The beam dump target design (illustrated in Fig. 31.1) comprises an evacuated beam pipe through which up to full energy 250 MeV protons travel from their extraction point at the cyclotron towards the target. Before reaching the target, an AC raster magnet with a field no larger than 1.5 T deflects the beam up to a maximum angle of 8.3 degrees to spread the incident full 1 mA current over the inner surface. As described later in the report, copper was chosen for the primary beam dump inner cone material through a trade off on thermal conductivity, activation, and cost. The target is cooled by water flowing through 30 coolant channels and outputs arranged symmetrically along the outer surface but

inside a thin exterior copper shell; this configuration allows for calorimetry that can evaluate any asymmetries in the distribution of energy deposition from the primary proton beam throughout the beam dump. This will be useful both in accelerator commissioning to full power and potentially as a diagnostic for measuring energy or current at high power. A thermal and mechanical analysis will also be presented in Section 13.5.

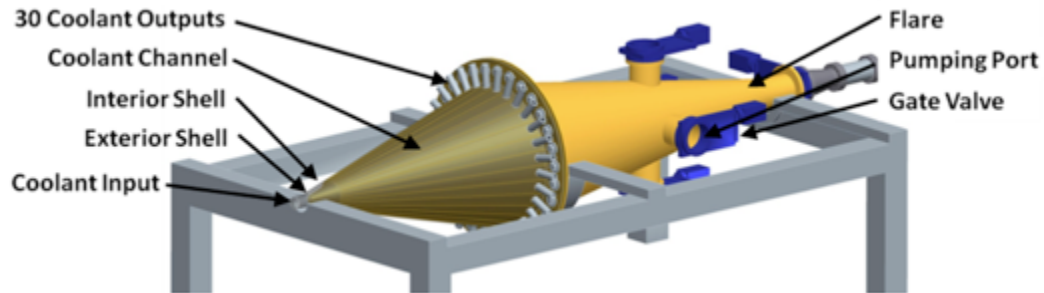


Fig. 13.1 Beam Dump Target Design Schematic

The final beam dump design obtained in this phase achieves significant reduction in overall dimensions and savings in material requirements relative to the preliminary design presented in the first phase of this program. An illustration of the current design baseline relative to its original dimensions appears in Fig. 13.2 below.

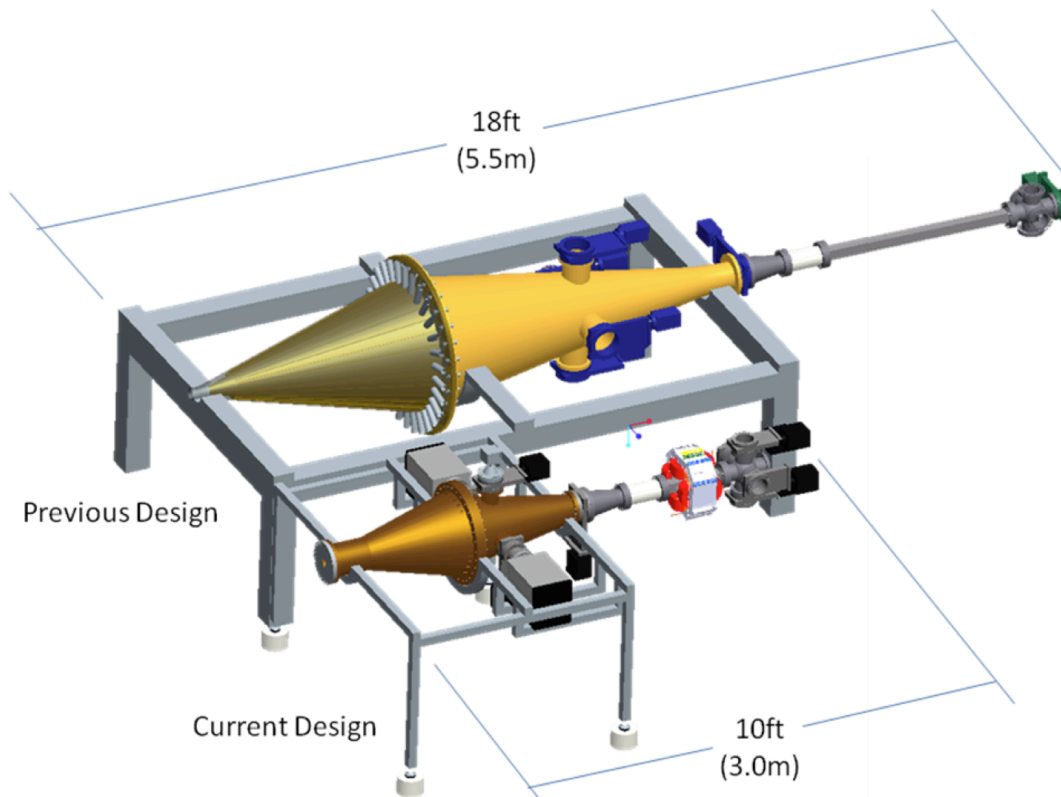


Fig. 13.2 Beam dump target sizing

All the main components (beam flare, main dump, pipes, etc.) remain but are scaled down relative to the original design. This reduction was obtained after more detailed simulations of the stopping of full-energy protons through the material making up the beam dump. In the original configuration, a thickness of 6.5 cm was chosen for the copper beam stop as this is the range of 250 MeV protons in copper. However, because the protons will be arriving at a shallow angle, they will traverse a 6.5 cm range but only occupy a fraction of that thickness in the beam dump. With the new sizing, nearly the entire beam dump volume is utilized for stopping protons posing a more optimal use of material requirements and minimizing radioisotope activation. The results of proton transport and secondary radiation production will be outlined in section 13.3 on radiation transport modeling.

13.3 Radiation Transport Modeling

In order to determine appropriate beam dump size, simulations were performed using the radiation transport code MCNPX⁶ to evaluate configuration trade-offs in arriving at a final beam dump design. These simulations start with the full energy 250 MeV protons and track most secondary particles, primarily photons and neutrons. Photonuclear interactions and proton interactions were sampled using CEM model physics rather than tabular data.

13.3.1 Energy deposition and heating

In order to evaluate cooling requirements, energy deposition was calculated for the original geometry presented at the Preliminary Design Review and the following interactions. For these simulations, energy deposition and heating are calculated as the total collisional heating due to all particle interactions within the tallied volume. Fig. 13.3 contains a representation of the target geometry as implemented in MCNPX.

⁶ Unless otherwise indicated, these simulations were performed using MCNPX version 2.7.E, a beta version of the MCNPX code that contains numerous enhancements for model physics and active interrogation applications. These features were later publically released as MCNPX 2.7.0

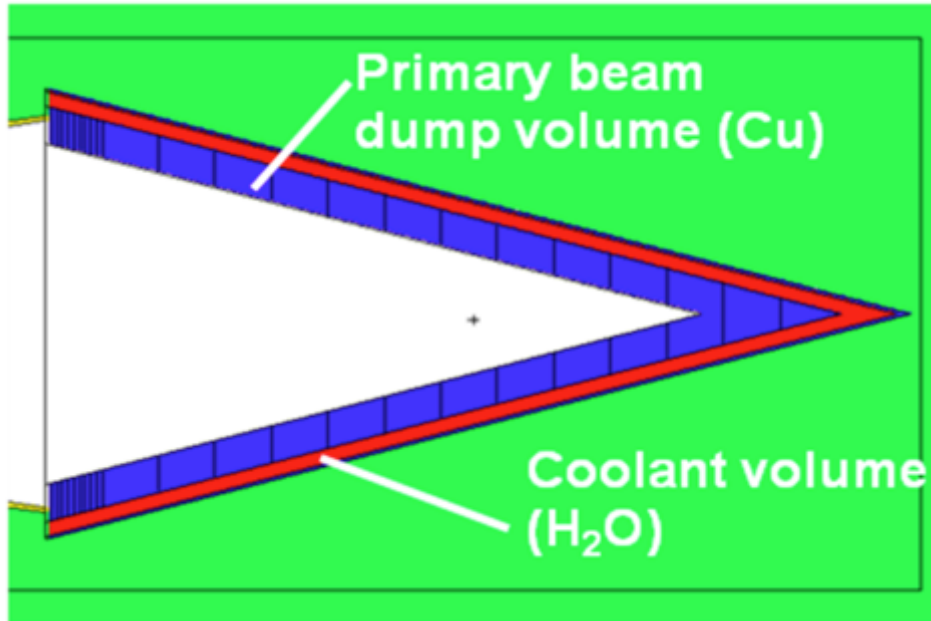


Fig. 13.3 MCNPX Geometry Implementation

A simplified model was implemented in MCNPX and the volume was segmented to examine heating throughout the volume. Initial examination showed that for a conical target with an inner half-angle below 10 degrees, essentially all the incident proton energy stopped within less than 3cm. A plot of the heating throughout the target is given in **Error! Reference source not found.** Here, energy deposition is dominated by protons interacting and stopping within a few cm of the inner surface of the beam dump. The outer half of the target volume does not contribute to stopping of primary protons though it may provide some shielding of secondary radiation. This configuration is further stymied by the interactions of secondary radiation, which can be expected to produce activation in material that does not serve the purpose of the beam dump target. Otherwise, heating is uniform along the inner surface of the target, consistent with the angular spread of the incident proton beam by the raster magnet. Also, due to the buildup of secondary radiation near the apex of the inner surface there is some peaking of heat generation at that location.

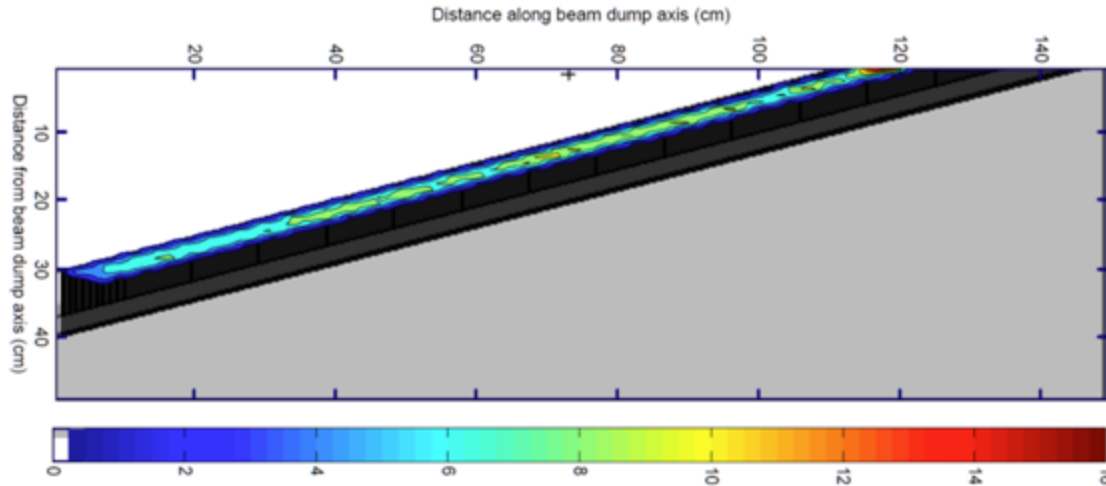


Fig. 13.4 Energy deposition values in $\text{W}/\text{cm}^3/\text{mA}$ and throughout the original beam dump

Additionally the variation along the length of the beam dump was also calculated both as a function of distance and throughout the target thickness. The results from one segmentation scheme for the initial geometry are given in **Error! Reference source not found.**

After reducing the beam dump size for the final beam dump design, these analyses were repeated to confirm that the heating profile is as expected and fully captures the incident proton beam less the production of secondary radiation. The results of this energy deposition calculation served as input to thermal analysis described in Section 13.5.1.

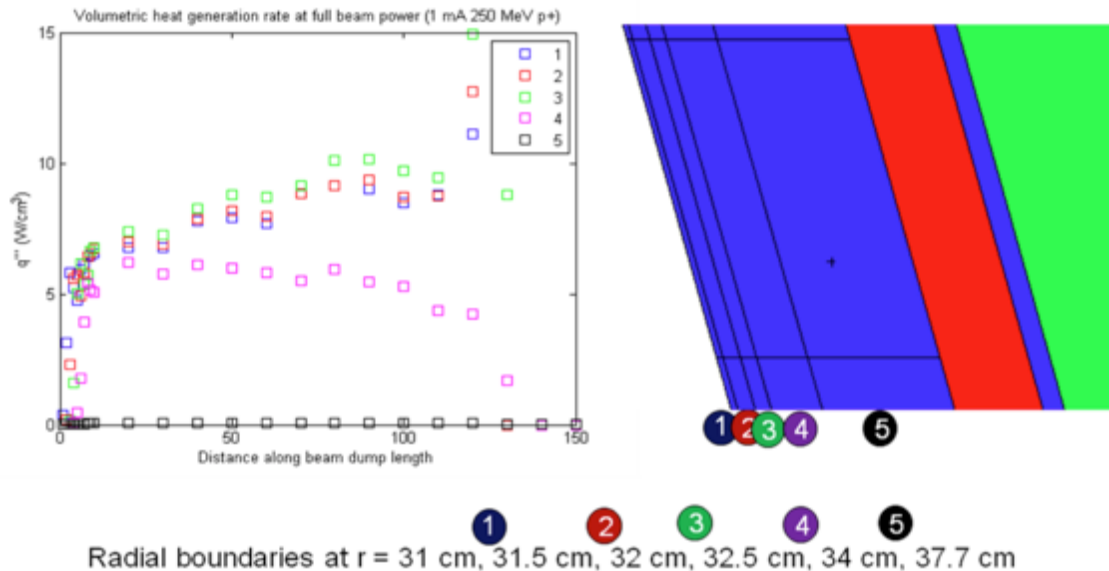


Fig. 13.5 Volumetric heating rates as a function of distance along the beam dump for several layers. The boundaries for each layer are given at the bottom of the figure.

13.4 Activation

Several beam dump materials were considered for the beam target and a trade study was performed for manufacturability and cost, among other factors. One of the more significant characteristics to be considered was residual activation. Unstable isotopes can be produced not only through the reactions of secondary particles (particularly photons and neutrons) but also by spallation initiated by the primary proton beam.

Because the incident protons will have an energy of 250 MeV, all materials will undergo activation to some extent, and the challenge is to choose a material that minimizes the long-term handling requirements while meeting the other mechanical, thermal, and cost considerations.

Copper was selected for this beam dump. Although a number of isotopes will be produced, they are generally shorter lived with half-lives on the order of several hours or shorter than those that might appear with other materials. The longest-lived copper isotope anticipated is ^{64}Cu with a half-life of 12.7 hours. The use of aluminum may result in isotopes with a similar distribution of half-lives, but the emissions from the decay of these isotopes, such as ^{28}Al and ^{24}Na exhibit higher energies and would produce larger dose handling requirements for the same amount of shielding.

The steady-state activity of several isotopes for the full power 250 MeV and 1 mA beam is given for the revised design in Table 13.1. These estimates were obtained through a combination of residual nuclide tallies in MCNPX where model physics is available as well as estimates based on measured cross section data and calculated photon or neutron fluxes in the simulated beam dump target.

Table 13.1 Steady-state activity for the full power 250 MeV 1 mA proton beam

Isotope	Reaction	Half-Life	Steady-State Activation (Ci)
^{62}Cu	$^{63}\text{Cu}(\text{g},\text{n}) + \text{spallation}$	9.74 minutes	2800
^{64}Cu	$^{63}\text{Cu}(\text{n},\text{g}) + ^{65}\text{Cu}(\text{g},\text{n}) + ^{65}\text{Cu}(\text{n},2\text{n}) + \text{spallation}$	12.7 hours	5700
^{66}Cu	$^{65}\text{Cu}(\text{n},\text{g})$	5.12 minutes	1100

It should be emphasized the above values are steady-state activities which is different from the activity that would be expected to be produced during operation of the accelerator. The true expected activities will depend on the duration of the time the accelerator is active. While beam power is on, these isotopes will accumulate with a characteristic time that depends on the corresponding half-life.

Simulations of the beam dump with shielding configurations were also evaluated within an MCNPX representation of one experimental hall. Figure 13.6 shows the dose fields with the beam dump at full power with no shielding and a maximum shielding of three feet of concrete.

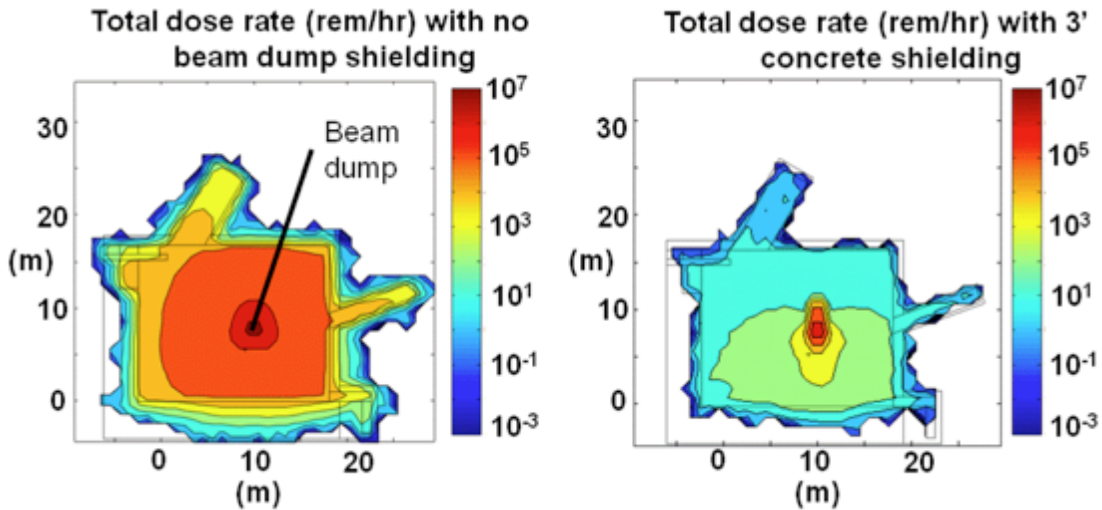


Fig. 13.6 Effects of shielding on dose fields surrounding beam dump with cyclotron at full power (1 mA of 250 MeV protons)

13.5 Mechanical Design and Analysis

For final design, analysis was performed using the results of radiation transport simulations for heating as a function of position throughout the beam target. This source term was modeled in the final beam dump design to determine cooling requirements. Other mechanical design issues for cooling, vacuum, pumping etc. were evaluated as articulated in the following sections.

13.5.1 Thermal Analysis

Total power dissipation into the proton beam dump is assumed to be 250kW. Water acts as the coolant with an inlet temperature of 20°C. Using these assumptions, thermal analysis was performed using a simplified representation of the cooling cone, which consisted of 54 volumetric power dissipation values previously calculated in MCNPX. These sections were divided into 18 sections along the beam axis and sections into the cones depth. The analysis results given in Fig. 13.7 show that system is sufficiently cooled at a rate of 18 GPM. However, for conservative measures a flow rate of 50 GPM will keep the water temperatures at 52°C and still keep water velocities from reaching degradation speeds on the surface. Coolant flow rates obtained through the analysis described in Section 13.5.2 show velocities throughout the system according to Table 13.2.

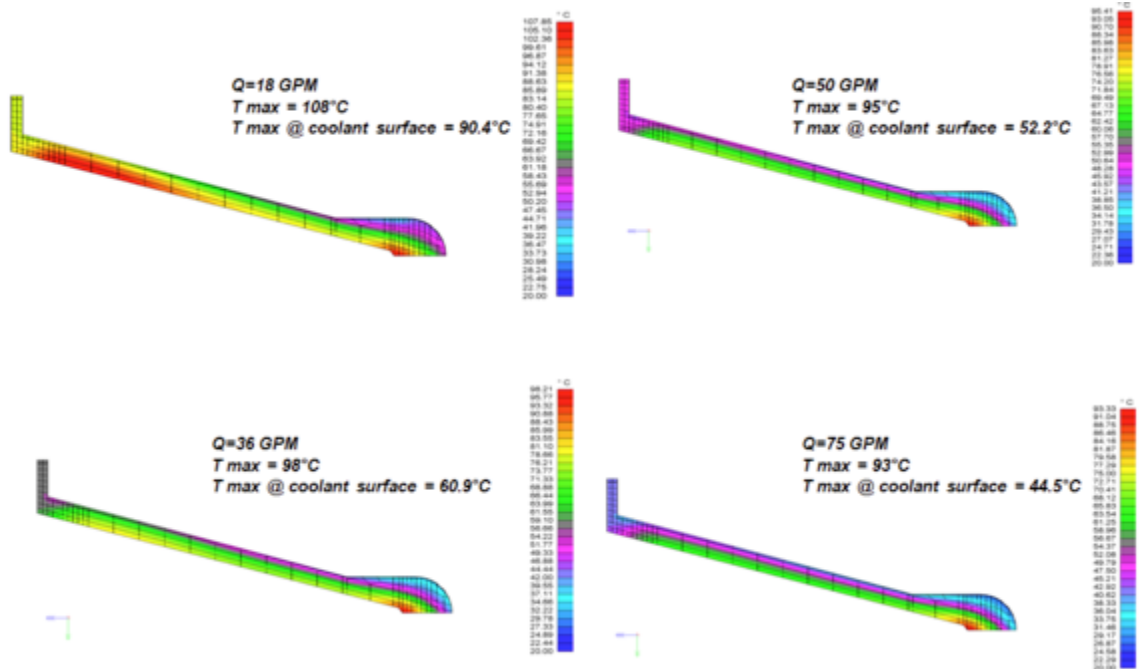


Fig. 13.7 Temperature profiles in beam dump for varying water coolant flow rates.

Table 13.2 Coolant flow rates throughout system

Sec.	X-Sec	Flow Rate	Temp.
AB	1-1/2" Dia	50 GPM @ 9.07 ft/s	20°C
BC	6" Dia	50 GPM @ 0.57 ft/s	20°C
CD	~ 1-3/4 x 1/4"	1.67 GPM @ 1.22 ft/s	39°C
DE	3/4" Dia	1.67 GPM @ 1.21 ft/s	39°C
EF	1-1/2" x 1-1/2"	25 GPM @ 3.56 ft/s	39°C
FG	1-1/2" Dia	50 GPM @ 9.07 ft/s	39°C
GH	2" Dia	50 GPM @ 5.11 ft/s	39°C
HA	2" Dia	50 GPM @ 5.11 ft/s	20°C
XY	2" Dia	100 GPM @ 10.21 ft/s	15°C
YZ	2" Dia	100 GPM @ 10.21 ft/s	25°C

13.5.2 Cooling System and Analysis

The cooling system is a closed-loop system, cooled by facility water as diagrammed in Fig. 13.8. The system's flow rate can be adjusted between 20-84 GPM. This range was governed by the thermal analysis to keep the temperatures well below boiling point; 50 GPM is the targeted optimal rate.

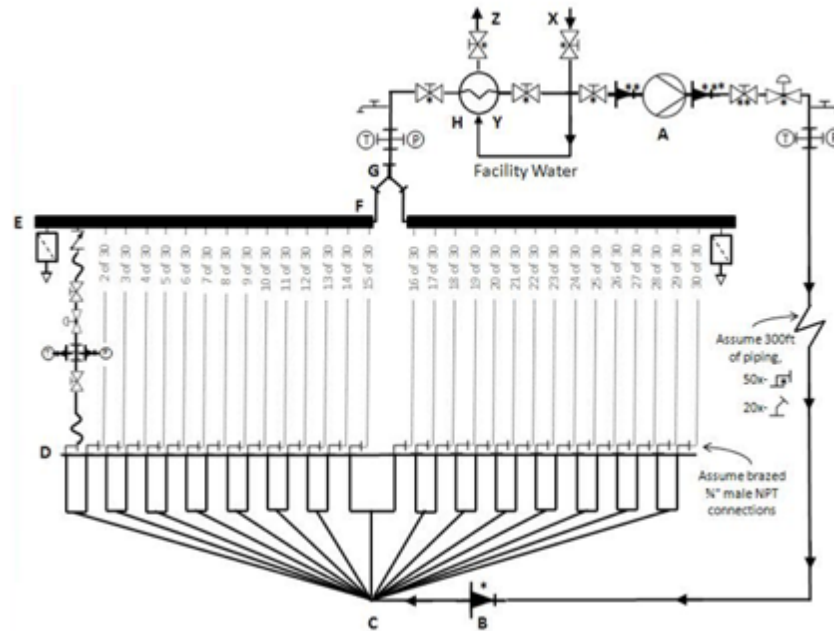


Fig. 13.8 Cooling schematic layout

The cooling chamber is divided into 30 sections for increased heat transfer area and for accurate system monitoring. In the event the proton beam or coolant water disperses unevenly across the beam dump temperature and pressure sensors will help detect this undesired affect. Electronic proportional valves will help regulate the flow through each channel keeping temperatures consistent across the cooling chamber as needed. A scheme for channel measurements is illustrated in **Error! Reference source not found.**

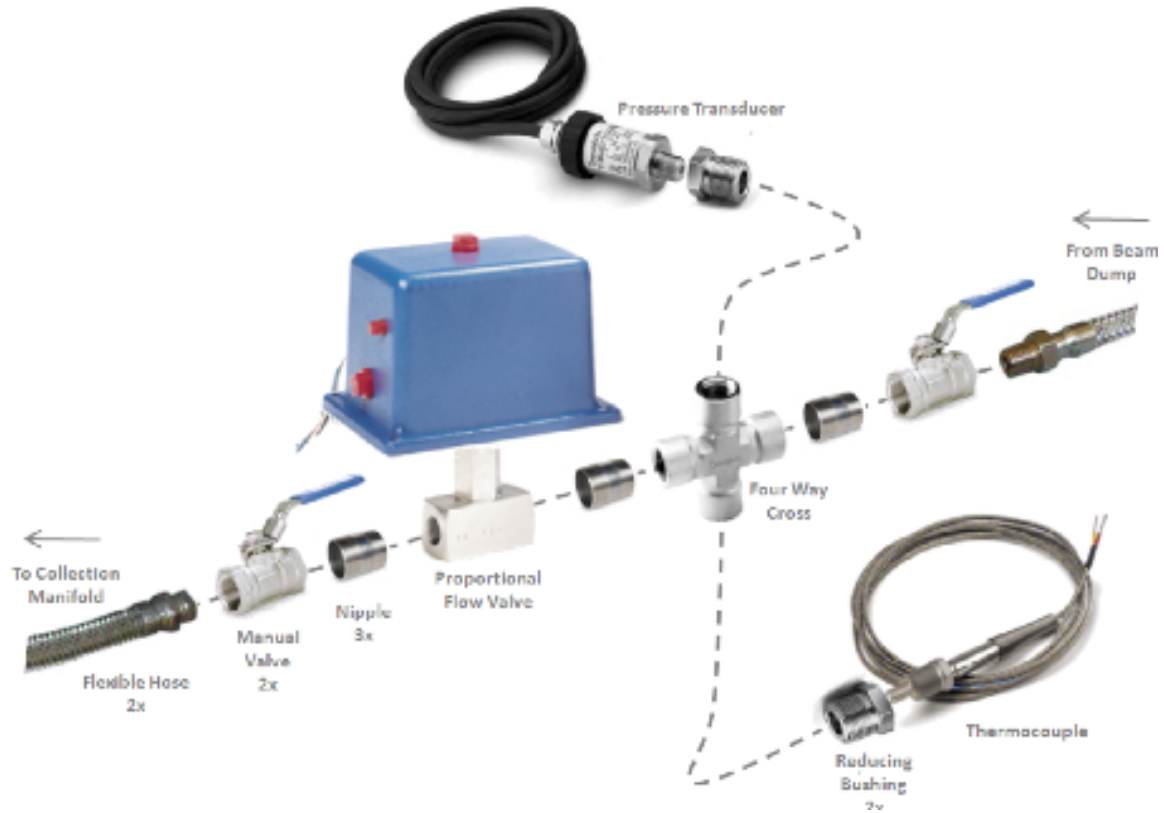


Fig. 13.9 Channel measurements

The water coolant then filters into a collection manifold (shown in Fig. 13.10), which leads to a heat exchanger and circulating pump. The facility water is assumed to flow at 100 GPM for proper cooling of the water back to 20°C.

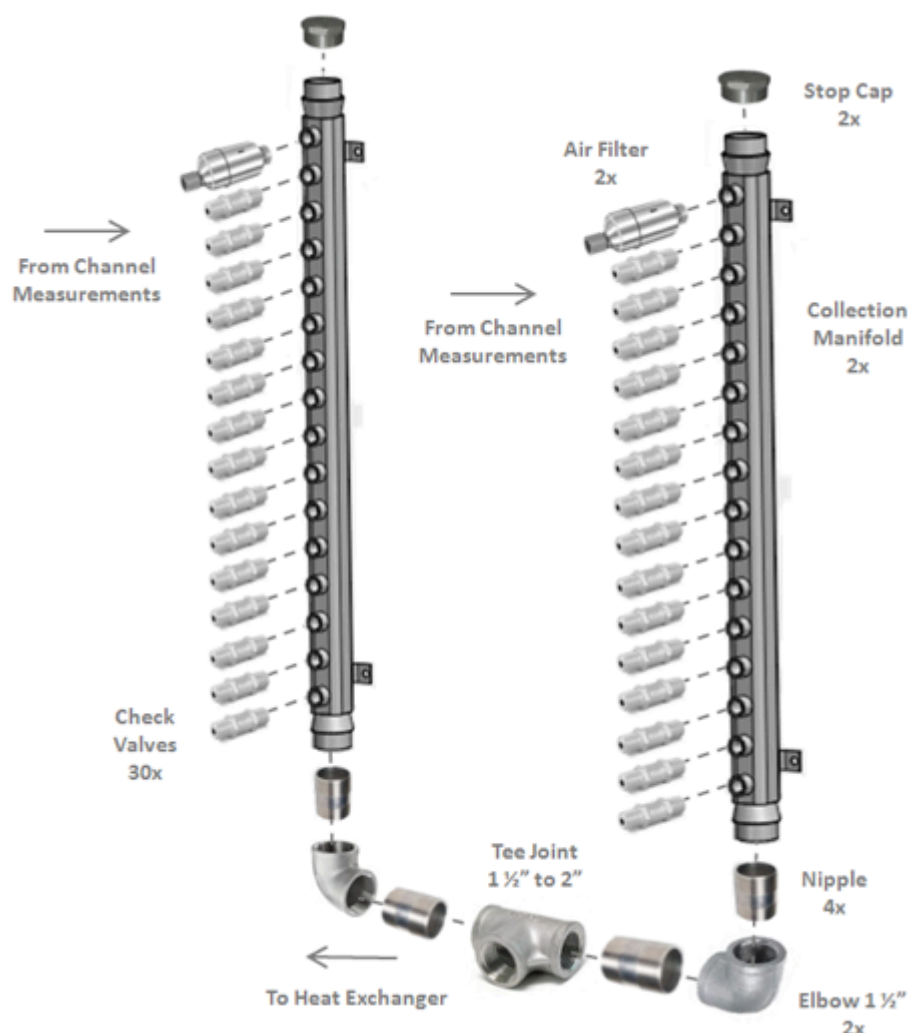


Fig. 13.10 Collection manifold

13.5.3 Vacuum system

The working pressure inside the beam dump is assumed to be 10^{-8} torr. Based on one DS 202 roughing pump and two VacIon 150 vacuum pumps the time required will be 10 days to get the system to 10^{-8} torr. Calculated pumping rates are given in **Error! Reference source not found.**

Figures 13.11, 13.12, and 13.13 show details of the vacuum system configuration.

Table 13.3 Pumping rates

Pump	Volume/Surface Area	Pressure	Run Time
Roughing	115,660 cm ³	7.5 x 10 ⁻⁴ Torr	50 Seconds
Ion (2x)	26,120 cm ²	10 ⁻⁶ Torr	2.4 Hours
Ion (2x)	26,120 cm ²	10 ⁻⁷ Torr	24 Hours
Ion (2x)	26,120 cm ²	10 ⁻⁸ Torr	241 Hours

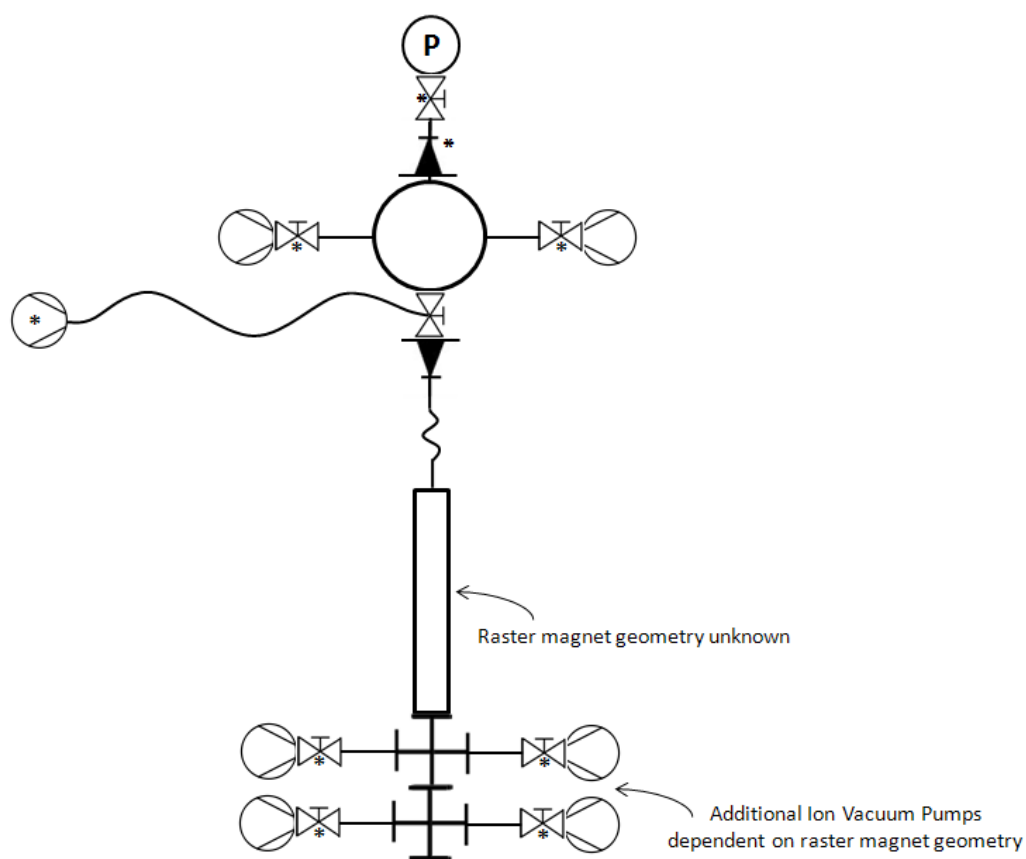


Fig. 13.11 Vacuum schematic layout

Gate valves are used on all ports to allow for repairs without bringing down the system completely. The top port was designed to mount a secondary pressure monitoring gauge or for other optional component diagnostics. Although not depicted in the figures, the pumps will be plumbed outside the radiation shielding to reduce noise and radiation dose fields.

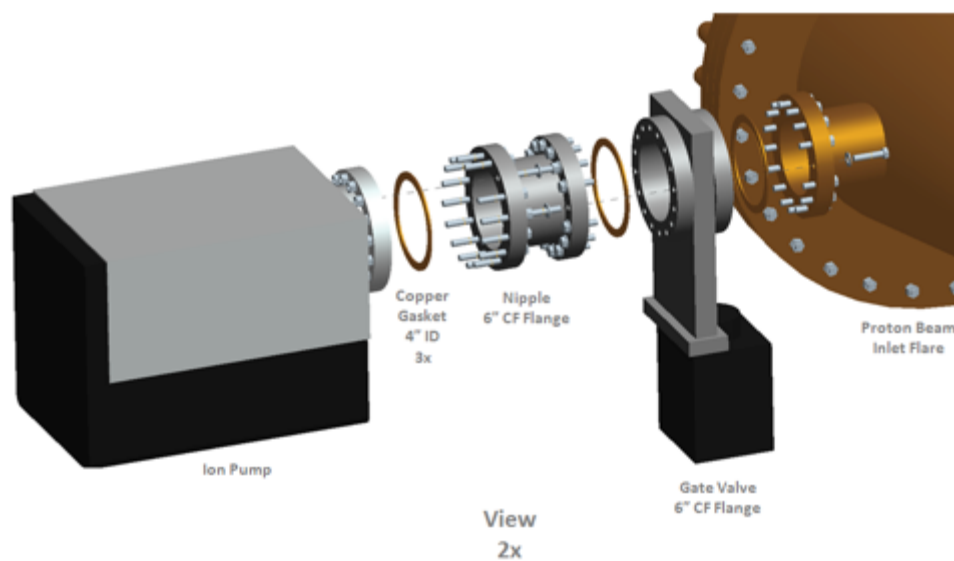


Fig. 13.12 Vaclon pump

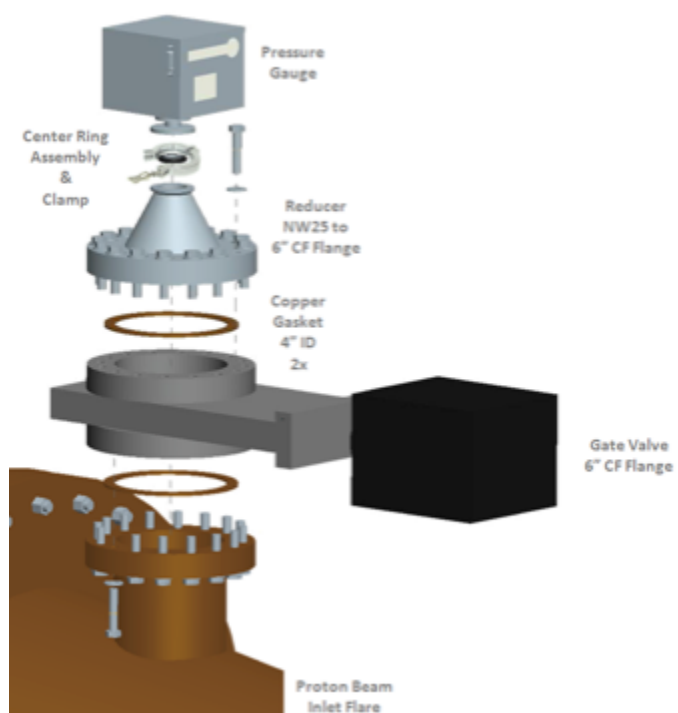


Fig. 13.13 Pressure gauge

13.6 Manufacturing plan

The majority of the cooling and vacuum system shown in the above section will be purchased parts from various supply vendors such as Grainger, McMaster Carr, MDC and Varian. However, the cooling chamber and inlet flare will both require custom manufacturing to create. The brazed assembly of the cooling chamber is shown in Fig. 13.14.

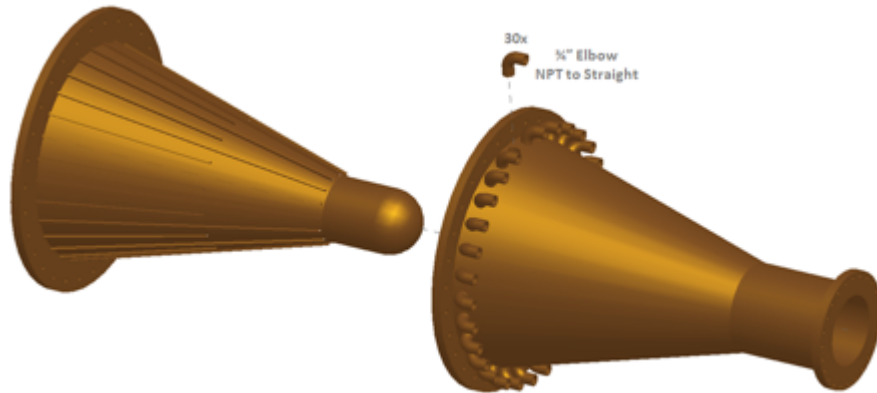


Fig. 13.14 Brazed assembly of cooling chamber

Copper was selected for the cooling chamber because of its density, heat transfer, and relatively low radiation half-life properties. Alternatively, the inlet flare (**Error! Reference source not found.**) can be aluminum for cost effectiveness but these properties are not as strongly desired for the inlet proportion of the proton beam dump, because aluminum won't stop the primary protons.

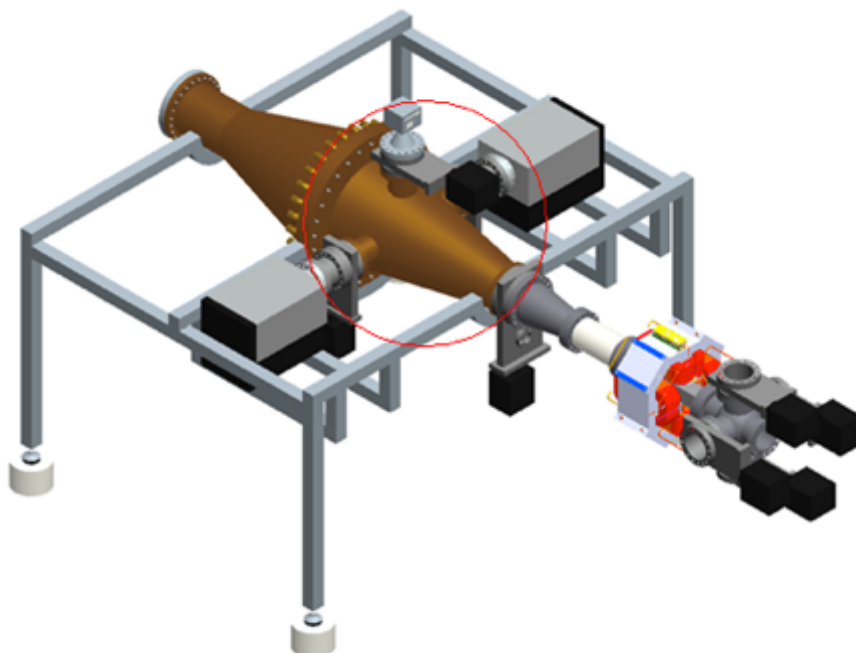


Fig. 13.15 Inlet flare

A three step process of casting, post-machining and brazing will be required. Not only will the two halves be brazed together (Fig. 13.14) but also the channel fins and lanced and offset fins (Fig. 13.16) will be brazed into place. Scott Craft Co. (Cudahy, CA), Major Tool (Indianapolis, IN) and (Tampa Brass Tampa, FL) all have the ability to manufacture these parts.




Fig. 13.16 Lanced and offset fins

Bills of materials for the vacuum and cooling systems are given in Table 13.4 and Table 13.5, respectively.

HISCC (Megatron) Final Report

Table 13.4 Vacuum system bill of materials

#	Symbol	Name	Qty	Part Number	Material
1		Ion Vacuum Pump	2	Varian- P/N: Vacclon Plus 150	
2		Roughing Vacuum Pump	1	Varian- P/N: DS 202	
3		Pressure Gauge	1	Varian- P/N: Eversys Mini-BA Gauge	
4		6" OD Gate Valve	3	MDC- P/N: GV-4000M-P-05	
5		8" OD Gate Valve w/ Roughing Port	1	MDC- P/N: GV-4000M-P	
6	N/A	Hinged Clamp, NW25	2	MDC- P/N: K100-C	
7		Reinforced Vacuum Tubing	10 ft	Generic Part	
8		Beam Dump Inlet Flare	1	Custom Part	
9	N/A	Center Ring Assembly, NW25	2	MDC- P/N: K100-CR	
10		Nipple	2	MDC- Custom Part Available upon request	
11		Reducer	1	MDC- Custom Part Available upon request	
12	N/A	Copper Gasket, 4-inch	8	MDC- P/N: GK-400	
13	N/A	Copper Gasket, 6-inch	2	MDC- P/N: GK-600	
14		4" Six-Way Cross	1	Geometryunknown	
15		Raster magnet	1	Geometryunknown	
16		Reducer	1	Geometryunknown	
17		Nipple, Electrical Isolator	1	Geometryunknown	

HISCC (Megatron) Final Report

Table 13.5 Cooling system bill of materials

#	Symbol	Name	Qty	Part Number (suggested)	Material
1		Pump	1	Goulds- P/N: 2BF15012 Grainger- P/N: 1NS16	303 Stainless Steel
2		Heat Exchanger	1	Bell & Gossett- P/N: 8PN422-40 LCA Grainger- P/N: 6RGF2	316 Stainless Steel
3		Pressure Sensor	32	Swagelok- P/N: PTI-S-NGXXX-27AD	316 Stainless Steel
4		Thermal Sensor	32	Omega Engineering- P/N: TC-E-NPT-G-80	304 Stainless Steel
5		Collection Manifold	2	Burger Engineering (Smartflow)- P/N: 8-S5-16-6-A	304 Stainless Steel
6		Air Vent/Bleeder	2	Spence Engineering- P/N: NAV-213 Grainger- P/N: 3EJ44	Stainless Steel
7		Check Valve	30	Swagelok- P/N: S5-12C2-25	316 Stainless Steel
8		Control Valve	30	Omega Engineering- P/N: PV12-S5 Parker Engineering- MODEL EPC Valve	316 Stainless Steel
9		Control Valve	1		
10		Manual Valve, 3/4"	60	Milwaukee Valve- P/N: 10SSOD-02-LL N Grainger- P/N: 1JBW4	316 Stainless Steel
11		Manual Valve, 2"	5	Grainger- P/N: 1WMI7	316 Stainless Steel
12		Manual Valve, 1-1/2"	1	Grainger- P/N: 1WMI27	316 Stainless Steel
13		Flexible Hose	60	Hose Master P/N: G075SHKJ360 Grainger- P/N: 1LN86	304 Stainless Steel
14		Reducer (6" to 1-1/2")	1		
15		Reducing Bushings	64	Swagelok- P/N: S5-12-RB-4	316 Stainless Steel
16		Drain Valve	2	General Part	
17		Y-Joint	1	General Part	
18		Crosses	30	Swagelok- P/N: S5-12-C5	316 Stainless Steel
19		90° Elbow	30	General Part	
20		90° Elbow	50	General Part	
21		45° Bend	20	General Part	
22		Nipple, 1/4"	90	Grainger- P/N: 1XAW9	316 Stainless Steel
23		1 1/2" Dia. Pipe	10ft	General Part	
24		2" Dia. Pipe	300ft	General Part	
25		6" Dia. Pipe	1ft	General Part	
26		Cap, 1 1/2"	2	Grainger- P/N: 6JK27	316 Stainless Steel
27		Reducer (2" to 1-1/2")	1	General Part	
28		Reducer (1-1/2" to 1-1/4")	1	General Part	

13.7 Long-lead items

Long lead items according to the above manufacturing plan will include:

- Custom cooling chamber (6 months)
- Custom flare (2-4 months)

13.8 Beam Monitoring and Diagnostics

As traditional interception beam diagnostics will not be possible for use with the full power beam, several alternatives (both intercepting and non-intercepting) were considered to be associated with the beam target. A summary of potential diagnostic concepts considered is given in **Error! Reference source not found.**13.6

Table 13.6 Beam diagnostic measurement concepts

INTERCEPTING		
TYPE	MEASURED VALUE	OPERATION
Segmented target	Energy	Measure current in electrically isolated thicknesses of target material
Electron beam profiler	High current proton beam profiles	Deflection of 1-2 keV electrons from high intensity proton beam indicates beam profile [<i>Wendt, et al., FERMILAB-CONF-08-663-AD</i>]
Thin graphite target	Beam profile	Image the induced activity in thin graphite target as indicator of 2D beam profile
NON-INTERCEPTING		
TYPE	MEASURED VALUE	OPERATION
¹⁰ B-lined proportional tube	Energy and Current	Benchmark neutron yield for current and energy
BLM	Beam loss	Bare PMT or PMT with scintillator for machine protection
BPM	Beam position	Measures x,y position of beam
Torroid	Current	Measures current via induced magnetic field

14.0 Acknowledgements

Many people contributed to the work in this report. Listed here are the people who contributed either technically or programmatically to this project.

MIT-PSFC: Timothy Antaya (now with Ionetix, Inc.), Philip Michael, Bradford Smith, Alex Zhukovsky, Alexey Radovinsky, Valery Fishman, Leslie Bromberg, Zach Hartwig, Darlene Marble.

Also Jeffrey Freidberg, Antoine Cerfon, Buddy Gardiner, and Felix Parra for the evolution of proton bunches study.

Legacy Recruiting: Kyra Oles, Richard Torti, Anthony Bistany, Richard Gazaille.

Michigan State University: John Vincent for the RF system design.

Raytheon – Integrated Defense Systems: Brandon Blackburn, Erik Johnson for the High Power Beam Dump design.

DISTRIBUTION LIST
DTRA-TR-12-40

DEPARTMENT OF DEFENSE

DEFENSE TECHNICAL INFORMATION
CENTER
8725 JOHN J. KINGMAN ROAD, SUITE 0944
FT. BELVOIR, VA 22060-6218
ATTN: DTIC

MASSACHUSETTS INSTITUTE OF
TECHNOLOGY
PLASMA SCIENCE AND FUSION CENTER
77 MASSACHUSETTS AVENUE, NW16,
CAMBRIDGE, MA 02139
ATTN: DR. J. MINERVINI

DEPARTMENT OF THE NAVY

NAVAL SEA SYSTEMS COMMAND
1333 ISAAC HULL AVENUE SE
WASHINGTON NAVY YARD, D.C. 20376-
1220
ATTN: MS. WANDA BROWN

EXELIS, INC.
1680 TEXAS STREET, SE
KIRTLAND AFB, NM 87117-5669
ATTN: DTRIAC

DEPARTMENT OF ENERGY

NATIONAL NUCLEAR SECURITY
ADMINISTRATION
1000 INDEPENDENCE AVE SW
WASHINGTON, DC 20585 0420
ATTN: DR. D. BEACH

OTHER GOVERNMENT

**DEPARTMENT OF HOMELAND
SECURITY**

WASHINGTON, DC 20528
ATTN: DR. J. RYNES
ATTN: DR. N. MOON

**DEPARTMENT OF DEFENSE
CONTRACTORS**

INSTITUTE FOR DEFENSE ANALYSES
4850 MARK CENTER DRIVE
ALEXANDRIA, VIRGINIA 22311-1882
ATTN: DR. J.SILK

PENNSYLVANIA STATE UNIVERSITY
APPLIED RESEARCH LABORATORY
P.O. BOX 30
STATE COLLEGE, PA 16804
ATTN: DR. D. MERDES